©Copyright 2017
Aaron T. Fricke

Sediment dynamics and deposits along the fluvial–marine transition: Tidal river to mangrove coast

Aaron T. Fricke

A dissertation
submitted in partial fulfillment of the
requirements for the degree of

Doctor of Philosophy

University of Washington

2017

Reading Committee:

Charles A. Nittrouer, Chair

Andrea S. Ogston, Chair

J. Wesley Lauer

Program Authorized to Offer Degree:
Oceanography

University of Washington

Abstract

Sediment dynamics and deposits along the fluvial–marine transition: Tidal river to mangrove coast

Aaron T. Fricke

Co-Chairs of the Supervisory Committee:
Professor Charles A. Nittrouer
Oceanography

Professor Andrea S. Ogston
Oceanography

Rivers supply the vast majority of sediment that reaches the global ocean. As many rivers approach the sea, they experience tidal influence in the absence of salinity, along a reach known as the tidal river. As a result, a significant fraction of the sediment discharged by rivers around the world passes through a tidal river before entering the ocean. Within the tropics, these tidal rivers also supply sediment to coastal mangrove forests near the river mouths. Although common, the deposits and dynamics associated with tidal rivers and the coastal mangrove forests they nourish remain poorly understood. Processes acting within tidal-river environments, as well as between tidal rivers and adjacent mangrove forests, are governed by a combination of fluvial and tidal processes, which are a focus of this work.

The Amazon River is the largest fluvial source of freshwater and sediment to the global ocean and has the longest tidally-influenced reach in the world. Two major rivers, the Tapajós and Xingu, enter the Amazon along its tidal reach. However, unlike most fluvial confluences, these are not one-way conduits through which water and sediment flow downstream toward the sea. The drowned river valleys (rias) at the confluences of the Tapajós and Xingu with the Amazon River experience water-level fluctuations associated not only with the seasonal rise and fall of the river network, but also with semidiurnal tides that propagate as far as 800 km up the Amazon River. Superimposed seasonal and tidal forcing, distinct sediment

and temperature signatures of Amazon and tributary waters, and antecedent geomorphology combine to create mainstem–tributary confluences that act as sediment traps rather than sources of sediment. Hydrodynamic measurements are combined with data from sediment cores to determine the distribution of tributary- and Amazon-derived sediment within the ria basins, characterize the sediment-transport mechanisms within the confluence areas, and estimate rates of sediment accumulation within both rias. The Tapajós and Xingu ria basins trap the majority of the sediment carried by the tributaries themselves in addition to $\sim$20 Mt y^{-1} of sediment sourced from the Amazon River. These findings have implications for the interpretation of stratigraphy associated with incised-valley systems, such as those that dominated the transfer of sediment to the oceans during low-stands in sea level.

The estimates of water and sediment discharged by the Amazon River are based on data from the lowermost non-tidal gauging station at Óbidos, $\sim$800 km upstream of the Atlantic Ocean. Depositional environments along the lengthy tidal river downstream of Óbidos have been proposed as important sinks for up to a third of the reported sediment discharge from the Amazon River. However, the morphology and dynamics of the intertidal floodplain have yet to be described. River-bank surveys in five areas along the Amazon tidal river reveal a distinct evolution in bank morphology between the upper, central, and lower reaches of the tidal river. The upper tidal-river floodplain is defined by prominent natural levees that strongly control the transfer of water and sediment between the mainstem Amazon River and its floodplain. Increased tidal influence in the central tidal river suppresses levee development, and tidal currents increase sediment transport into the distal parts of the floodplain. The floodplain morphology in the lower tidal river closely resembles marine intertidal environments (e.g., mud flats, salt marshes), with dendritic tidal channels incising elevated vegetated flats. Theory, morphology, and geochronology suggest that the dynamics of sediment delivery to the intertidal floodplain of the Amazon tidal river vary along its length due to the relative dominance of fluvial and tidal influence.

The interplay between fluvial and marine influence is similarly felt in coastal mangrove forests that are nourished by tidal rivers. Mangrove forests are an important means of coastal

protection along many shorelines in the tropics, and are often associated with large rivers there. The mangrove forest at the seaward end of Cù Lao Dung, an island in the Mekong Delta, includes areas with progradation rates of 10s of meters per year, and areas that have experienced little to no progradation in recent decades. The physical proximity (<12 km) of these two environments allows detailed hydro- and sediment-dynamic measurements to be related directly to morphologic change and century-scale stratigraphy. Contrary to conventional understanding, the region of mangrove forest prograding most rapidly is subject to the greatest wave attack, while progradation is slowest in the most quiescent area. Limited progradation here is the product of a reduction in the supply of sediment to certain parts of the mangrove forest due to estuarine dynamics operating on spring–neap timescales. Measurements of sediment flux show transport into the rapidly prograding part of the forest, and transport out of the area with minimal progradation. Century-scale rates of sediment accumulation determined using ^{210}Pb geochronology are consistent with in-situ dynamical measurements and geomorphic evolution of the mangrove forest. Where progradation is most rapid, sediment accumulation rates (3–5.1 cm y^{-1}) exceed the rate of local sea-level rise ($\sim$1.5 cm y^{-1}). In contrast, sediment-accumulation rates in the area of minimal progradation (0.8–2.8 cm y^{-1}) barely keep pace with local sea-level rise, if at all. Physical stratification is well preserved in cores from areas of rapid progradation, consistent with energetic transport processes and an ample sediment supply. Greater impact from bioturbation and episodic sediment delivery produce more chaotic bedding where progradation is less rapid. The presence of a supply-limited mangrove forest adjacent to a major sediment source highlights the complexity of sediment-supply pathways in coastal mangrove environments.

TABLE OF CONTENTS

Page

List of Figures iii

List of Tables vii

Chapter 1: Introduction 1
1.1 The Tidal River 2
1.2 River-Mouth Mangrove Forests 3
1.3 Organization of the text 4

Chapter 2: River tributaries as sediment sinks: Processes operating where the Tapajós and Xingu Rivers meet the Amazon tidal river 5
2.1 Introduction 5
2.2 Background 6
2.3 Methods 9
2.4 Results 11
2.5 Discussion 24
2.6 Conclusions 38

Chapter 3: Morphology and dynamics of the intertidal floodplain along the Amazon tidal river 40
3.1 Introduction 40
3.2 Background 43
3.3 Methods 45
3.4 Results 50
3.5 Discussion 55
3.6 Conclusions 63

Chapter 4: Asymmetric progradation of a coastal mangrove forest controlled by combined fluvial and marine influence, Cù Lao Dung, Vietnam 67
4.1 Introduction 67

4.2 Setting 68
4.3 Background 70
4.4 Methods 72
4.5 Results 74
4.6 Discussion 87
4.7 Conclusions 96

Chapter 5: Summary 98

Bibliography 101

LIST OF FIGURES

Figure Number — Page

2.1 Maps of the Tapajós and Xingu Rias and the Amazon tidal river 8
2.2 Hydrographs of the Amazon, Tapajós, and Xingu Rivers 12
2.3 Cross sections of residual velocity in the Tapajós Ria during low- and high-discharge conditions 14
2.4 Cross sections of residual velocity in the Xingu Ria during low- and high-discharge conditions 15
2.5 Cross sections of water temperature along a ∼60-km transect from the XinguÐAmazon confluence into the Xingu Ria. 18
2.6 Sediment grain-size distributions over the lengths of ten kasten-type cores from the Tapajós Ría. 19
2.7 Sediment grain-size distributions over the lengths of seven kasten-type cores from the Xingu Ría. 20
2.8 Profiles of excess ^{210}Pb from 9 kasten-type cores from the Tapajós Ría. 21
2.9 Profiles of excess ^{210}Pb from 7 kasten-type cores from the Xingu Ría. 22
2.10 Clay-mineral composition from the <2-μm fraction of 20 surface sediment samples from the Tapajós and Xingu Rías 23
2.11 Sediment grain size from the Tapajós and Xingu Rías. 25
2.12 Satellite image of the birdsfoot delta that has built upstream into the Tapajós Ría near the Tapajós-Amazon confluence. 27
2.13 Water level over one tidal cycle as measured on 2 December 2012 at the town of Almeirim 28
2.14 Wind-driven circulation in the Tapajós Ría is associated with persistent northeasterly winds. 32
2.15 Sediment budgets for the Tapajós and Xingu Rías based on ^{210}Pb geochronology. 34
2.16 Cartoon representation of the possible sediment-transport processes that deliver Amazon-derived sediment to the confluence regions of the ría basins. . . 37

3.1 Annotated map of the Amazon tidal river between Óbidos and the Atlantic Ocean. 42
3.2 Gauge height of the Amazon River at Óbidos between 1975 and 2015. 46
3.3 Satellite images (Landsat 8) of the river bank survey areas. 47

3.4 Fractional response to water-level changes at Óbidos and tidal oscillations at Macapá along the length of the Amazon tidal river 48

3.5 Summary of water-level records used to define reference datum. 49

3.6 Representative river-bank profiles from each of the five survey areas. 51

3.7 Elevation of the banks of the Amazon tidal river between Lago Grande de Monte Alegre and Macapá relative to the water-level datum. 52

3.8 Surface-sediment grain size along the banks of the Amazon tidal river between Lago Grande de Monte Alegre and Macapá. 53

3.9 Profiles of excess ^{210}Pb from cores collected along the banks of the Amazon tidal river between Lago Grande de Monte Alegre and Macapá. 54

4.1 Location map of study area. Panel a shows the entire Mekong River delta including the southern Sông Hậo channels and the northern Sông Tiền channels. The enlargement at right (b) shows the seaward limit of the island of Cù Lao Dung with approximate locations of the SW and NE sites. A yellow star marks the approximate location of the study site described in Vo-Luong et al. (2017). 69

4.2 Four infrared Landsat images show seaward progradation of Cù Lao Dung between 1975 and 2010. The shoreline from each previous panel is marked on subsequent satellite images from 1990, 2000, and 2010. Maximum progradation between 1975 and 2010 is ∼2.8 km at the southernmost extent of the island. 70

4.3 Comparison between surface-sediment grain-size distributions for the SW and NE sites during September 2014 and March 2015. Individual curves show the cumulative mass percent of each sample that is finer than the corresponding particle diameter in ϕ units (lower scale), and microns (upper scale). Bold black curves are the mean of the individual sample distributions shown. Sediment samples from the SW site (September: $n = 44$, March: $n = 23$) are generally coarser than samples from the NE site (September: $n = 20$, March: $n = 9$) and show a greater range in grain size. Mean grain size at the SW site is coarser in March than in September, while the mean grain size of samples from the NE site is very similar between the two seasons. 76

4.4 Repeat surface-sediment grain-size transect at the SW site during September 2014 and March 2015. Samples were collected along a transect extending from 30 inside the mangrove forest to a distance of 150 m from the seaward limit of the mangroves. Pie charts show the fraction of sand (yellow), silt (brown), and clay (gray) in each sample. Samples from both seasons show a fining trend into the mangrove forest, and samples collected in March are consistently coarser than samples collected at the same locations in September. 77

4.5 Repeat X-ray negatives (September and March) of the upper ∼28 cm of the seabed at the seaward edge of the mangrove forest at the SW site. Darker colors correspond to lower bulk density (more mud) and light colors indicate higher bulk density (more sand). X-radiographs were collected within 5 m of each other and show an increase in the proportion of sand in the upper 10 cm of the seabed between September and March. 78

4.6 X-ray negatives of the upper 250 cm of two vibracores from the seaward edge of the Cù Lao Dung mangrove forest. Core MM-44 (a) was collected at the SW site, and core MM-94 (b) was collected at the NE site. Darker colors correspond to lower bulk density (more mud) and light colors indicate higher bulk density (more sand). Simplified core descriptions are shown to the right of each core section. 79

4.7 Profiles of excess ^{210}Pb from cores collected in or near the Cù Lao Dung mangrove forest. Panels a and b show data from cores at the SW site; MM-44 (a) was collected at the seaward edge of the mangrove forest, and MM-208 (b) was collected ∼500 m farther landward. Panel c shows data from a core (MM-249) collected in the interior of the mangrove forest at the middle site (see Vo-Luong et al., 2017). Panels d and e show data from cores collected at the NE site. MM-95 (d) was collected ∼300 m seaward of the mangrove forest on the unvegetated intertidal flat, and MM-94 (e) was collected at the boundary between the mangrove forest and flat. Log-linear regressions and correlation coefficients (R^2) are determined for the profile regions of log-linear decay, and the sediment accumulation rate (S) is shown. 80

4.8 Plots of water depth, significant wave height (H_{sig}), suspended-sediment concentration (SSC), and salinity. Panels a and b show data from the SW site during September 2014 and March 2015, respectively. Depth, H_{sig}, and SSC were measured by an RBR-duo, and salinity was measured by a Hobo conductivity sensor. All sensors were located at the seaward edge of the mangrove forest (see Table 4.1). Panels c and d show data from the NE site during September 2014 and March 2015, respectively. Panel d also includes salinity data from the Định An channel (dashed red line) collected ∼20 km upstream from the NE site using a YSI CTD. River salinity was 0 PSU during September 2014, and is not shown in panel c. All other parameters in panels c and d were measured by an RBR-concerto located at the seaward edge of the mangrove forest (see Table 4.1). The period of spring tidal conditions is marked for September and March deployments in panels a and b, respectively. 82

4.9 Four panels showing histograms of wave-orbital and depth-averaged current velocity for the SW and NE sites during September and March deployments. Blue-shaded bars represent wave-orbital velocities computed from 6-Hz pressure data collected at the mangrove–flat boundary, and semi-transparent light brown-shaded bars represent depth-averaged current velocities measured by Aquadopps locted 150 m inside the mangrove forest (see Table 4.1). Regions of overlap between the two distributions appear as dark brown. Plots a and b show data from the SW site, and plots b and d show data from the NE site. 83

4.10 Eight plots showing the relationship between SSC and either wave-orbital velocity or salinity. Gray-shaded plots (b, d, f, h) represent data from the NE site, while unshaded plots (a, c, e, g) show data from the SW site. The four plots on the left show data from September (high-flow and calm), while the four plots on the right show data from the March (low flow and energetic). Data are colored such that red dots represent data collected during spring tides and blue dots represent data collected during neap tides. Trendlines are fit to both spring (red) and neap (blue) data in each panel, and correlation coefficients (R^2) are reported for each line. 84

4.11 Map of the Cù Lao Dung mangrove forest showing the orientation of sediment flux at the SW and NE sites in September 2014 and March 2015. Colored lines are progressive vectors of sediment flux as measured by an Aquadopp current profiler and calibrated OBSs at the origin of each line ($\sim$ 150 m inside mangrove forest, see Table 4.1). These lines are constructed by joining sediment-flux vectors measured every 10 minutes in a tip-to-tail fashion. Line shading transitions from blue at the beginning of the deployment to yellow at the end of the deployment. Spring tidal conditions spanned roughly days 3-9 in September, and days 2-8 in March. Scaling of the vectors is arbitrary but all vectors are shown at the same scale. 86

4.12 Distributions of wave-orbital velocities from the period 3–8 March 2015 at the NE (solid blue), middle (dotted red), and SW (dash-dot yellow) sites. Wave orbital velocities increase from NE to SW. Data from the middle site are from Vo-Luong et al. (2017). 89

LIST OF TABLES

Table Number Page

2.1 Summary of hydrodynamic conditions in the Tapajós and Xingu Rias during periods of low and high discharge of each tributary 16

2.2 Summary of water temperatures in the Tapajós and Xingu Rías and the Amazon River during the four study periods 17

3.1 Summary of some of the key attributes of the upper, central, and lower reaches of the tidal river. 64

4.1 Summary of instruments deployed in the Cù Lao Dung mangrove forest during field campaigns in Septemer 2014 and March 2015. 74

4.2 Seasonal summary of wave, suspended-sediment concentration, salinity, and temperature data from instruments deployed on the mangrove/flat boundary (Table 4.1) at the SW and NE sites in the Cù Lao Dung mangrove forest. Mean significant wave heights (H_{sig}) and mean suspended-sediment concentrations (SSC) are statistically different between both seasons and sites at a 95% confidence level. 81

ACKNOWLEDGMENTS

The completion of this research has required the the help and support of countless individuals and organizations over the past 6 years. I thank my advisers, Chuck Nittrouer and Andrea Ogston, for their guidance, support, and camaraderie, both in the field and on campus. I also owe a great deal to the rest of my committee: Wes Lauer, Miles Logsdon, Jeff Richey, Dave Montgomery, and Erkan Istanbulluoglu. I also thank my first adviser, Ben Sheets, for bringing me to U.W., and advice over the course of my graduate career.

I am thankful for the friendship of the graduate students, past and present, of the Sediment Dynamics Group. In particular, my former office mate, Dan Nowacki, and office neighbors Rip Hale and Emily Eidam have been tremendous resources.

I am also fortunate to have participated in a number of collaborative research projects around the world. In Brazil, I tremendously appreciate the camaraderie and collaboration with the students, staff, and faculty Universidade Federal do Pará. In Vietnam, I am sincerely grateful to Dan Culling and Rich Nguyen for their tenacity and friendship. I also give thanks to the students, staff, and faculty of Vietnam National University.

I owe many thanks to outstanding staff of the School of Oceanography administration office, and to the UW Oceanography Engineering Services, especially Dave Thoreson, Randy Fabro, and Tor Bjorklund.

The Amazon research was supported by the Office of Naval Research (award numbers N00014-13-1-0075 and N00014-13-1-0127), and the National Science Foundation (award number OISE-1157410). Work on the Mekong was funded by the Office of Naval Research (award numbers: N00014-12-1-0181, N00014-13-1-0075, N00014-13-1-0781, N00014-15-1-2014, N0014-15-1-2011, N0014-13-1-0127)

Finally, and most importantly, I thank my friends and family, and in particular, my wonderful wife Beth.

Chapter 1

INTRODUCTION

The field of sedimentology has increasingly embraced a source-to-sink framework in the study of sedimentary systems (e.g., Driscoll and Nittrouer, 2000; Goodbred, 2003; Carter et al., 2010; Kuehl and Nittrouer, 2011). Such a framework encourages investigating individual sedimentary environments in the context the larger transport system of which they are a part. The historical boundaries of sedimentary research; hillslope, fluvial, littoral, shelf, and deep marine have blurred as cross-environment collaboration has moved toward a seamless understanding of sedimentary systems from mountains to the deep ocean. However, the source-to-sink framework has also identified environments that are weak or missing links in our knowledge of this sedimentary chain, chief among them the tidal river and river-dominated coastal environments, including mangrove forests.

The tidal river is defined as the reach of river where tides propagate, but salinity does not penetrate. While many rivers have some degree of tidal influence in their lowest freshwater reaches, it is large, low-gradient rivers where the tidally influenced reaches are especially significant. Of the worlds' twelve largest rivers measured by freshwater discharge, seven lie within the tropics, and six have tidally influenced reaches longer than 200 km (Milliman and Farnsworth, 2011; Barua, 1990; Wolanski et al., 1996; Kravtsova et al., 2009; Andel, 1967). These six rivers (Amazon, Orinoco, Bramaputra, Mekong, Ganges, Ayeyarwaddy) are responsible for ∼25% of the freshwater and ∼15% of the sediment discharged to the global ocean (values from Milliman and Farnsworth, 2011). The tidal reaches of these rivers are characterized by low gradients and vast floodplains. Where they meet the ocean, sediments from these rivers nourish some of the largest mangrove ecosystems on earth. While the scale of tropical tidal-river systems is immense, our understanding of the sediment dynamics within them is limited. This dissertation describes research in the Amazon and Mekong tidal rivers that elucidates important interactions between the tidal river and floodplain

environments, and between the tidal river and linked coastal mangrove forests.

The chapters that follow will focus on sedimentary deposits and processes. Sediment, however, does not move from source to sink alone. Rather, sediment carries with it important nutrients and potentially harmful pollutants (e.g., heavy metals, pesticides). Moreover, ~90% of the organic carbon that is preserved in marine deposits was transported there sorbed to surfaces of sediment particles (Keil et al., 1994). Understanding the mechanisms by which these sediment-associated constituents move through, are potentially trapped in, and interact with depositional environments along their path to the sea is an added benefit of source-to-sink studies.

1.1 The Tidal River

The Amazon River is the largest single source of freshwater and sediment to the ocean, and its ~800-km tidal river is also the longest in the world (Milliman and Farnsworth, 2011; Nittrouer et al., 1995b). Our knowledge of the Amazon tidal river is informed by substantial bodies of research at its upstream and downstream limits. Numerous studies have focused on hydro- and sediment dynamics of the non-tidal Amazon system upstream of the village of Óbidos, located at the head of tides (Gibbs, 1967; Mead et al., 1979; Milliman and Meade, 1983; Meade et al., 1985; Mertes, 1994; Dunne et al., 1998). A similarly impressive body of work describes the dynamics and accumulation of Amazon-derived sediment in the litoral zone and continental shelf (Nittrouer et al., 1995b; Allison et al., 1995b; Nittrouer and DeMaster, 1996; Kuehl et al., 1996).

Less well studied is the Amazon tidal river from the upstream limit of tides at Óbidos to the Atlantic Ocean. The Amazon tidal river is an ideal location to study the interactions between a tidal river and its floodplain and tributaries. The gentle gradient of the lower Amazon River, and macrotidal conditions at the river mouth ensure that the tidal signal is able to influence a large reach of river and floodplain. The great length of the Amazon tidal river allows for the study of a variety of sedimentary environments with distinct proportions of fluvial and tidal influence. Because the Amazon River is in a nearly natural condition, without dams, dredging, or artificial levees, we are able to study the natural behavior of the system, and gain insights into the effects of future and past alteration of other large rivers.

1.2 River-Mouth Mangrove Forests

Along tropical coastlines, mangroves are the dominant form of intertidal vegetation. Tropical rivers collectively export more than 60% of the particulate matter to the global ocean (Nittrouer et al., 1995a). Coastal mangrove forests are often found near these river mouths, where they are nourished by sediment discharged from adjacent rivers. The combination of sediment supply and natural armoring by mangroves help to limit erosion associated with storm surge and wave attack (e.g. Alongi, 2008; Granek and Ruttenberg, 2007). As mentioned above, many of the largest tropical rivers that nourish such coastal mangrove forests (Amazon, Orinoco, Ganges-Bramaputra, Mekong, Ayeyarwaddy) have tidal reaches greater than 200 km in length (Milliman and Farnsworth, 2011; Barua, 1990; Wolanski et al., 1996; Kravtsova et al., 2009; Andel, 1967). Given the association between large tropical tidal rivers and mangrove forests, an understanding of the linkages between the two environments is needed to resolve more fully sediment dynamics acting to supply sediment to and create the morphology of these linked mangrove forests.

Much of the coastline of the Mekong Delta in southern Vietnam is fringed by mangrove forests, especially near mouths of major distributary channels of the large tropical Mekong River. The combination of dramatic coastal subsidence (Erban et al., 2014) and loss of mangroves forests due to coastal erosion and development pressure (Thu and Populus, 2007) makes these mangrove forests important targets for research. Cù Lao Dung is a mid-channel island located in the Sông Hậo distributary of the Mekong tidal river. The seaward shoreline of Cù Lao Dung, which is colonized by mangroves, is prograding in an asymmetric manner. This asymmetric progradation of the coastline provides an opportunity to examine the suite of processes that either encourage or inhibit progradation of a coastal mangrove forest at the mouth of a tidal river. The dominant signals impacting sediment dynamics in the Mekong Delta (river discharge and marine energetics) occur at different times of the year. This lack of coherence between river discharge and ocean energy (e.g. waves, currents) allows dynamics within the coastal mangrove forest to be more easily attributed to influence from either the marine realm or tidal river.

1.3 Organization of the text

The objective of the proposed research is to improve our understanding of the mechanisms of sediment exchange between tropical tidal rivers and depositional environments along the tidal reach, and adjacent marine shorelines. These environments include drowned-confluence lakes (rias) and intertidal floodplains, as well as mangrove forests near tidal-river mouths. To that end, Chapter 2 focuses on sediment dynamics and deposits within the Tapajós and Xingu Rias, lake-like bodies of water formed at the confluences of these major tributaries with the Amazon tidal river. Chapter 3 explores the morphologic evolution of the floodplain of the Amazon tidal river along its transition from strongly fluvial (upstream) to strongly tidal (downstream). Chapter 4 examines the relative influence of fluvial and marine forcing on the asymmetric progradation of the coastal mangrove forest on Cù Lao Dung at one of the mouths of the Mekong tidal river. Taken together these three chapters (2–4) address a gap in our understanding of the role tidal-river processes play in influencing sedimentation in adjacent sedimentary environments. Chapter 5 provides a summary of this work and discusses it in the context of source-to-sink sedimentological research.

Chapter 2

RIVER TRIBUTARIES AS SEDIMENT SINKS: PROCESSES OPERATING WHERE THE TAPAJÓS AND XINGU RIVERS MEET THE AMAZON TIDAL RIVER[1]

2.1 Introduction

If not for the fact that the Tapajós and Xingu Rivers flow into the Amazon River rather than the sea, they would be ranked among the largest rivers on Earth. Ignoring the other large tributaries of the Amazon (Madeira, Negro, Japura), the Tapajós, with a mean annual discharge of 13,500 $m^3 s^{-1}$, would rank as the 15th largest river in the world based on discharge and the Xingu as the 18th (Latrubesse et al., 2005; Milliman and Farnsworth, 2011). Combined, these two tributaries contribute ∼10% of the freshwater carried by the Amazon River (Latrubesse et al., 2005; Milliman and Farnsworth, 2011). The Tapajós and Xingu join with the Amazon mainstem along the freshwater tidally influenced reach of the Amazon River, and consequently sedimentary processes near both confluences are influenced by factors acting on both seasonal and tidal timescales.

During the last glacial period, falling sea level led to incision of the Amazon River and its tributaries (Sioli, 1984; Irion, 1984; Vital and Stattegger, 2000a). Post-glacial sea-level rise caused the bed of the sediment-laden Amazon River to aggrade. This aggradation effectively dammed the confluences of a number of tributaries in the lower reach of the Amazon (Sioli, 1984; Irion, 1984). Many of these tributaries, including the Tapajós and Xingu, drain low-elevation, highly weathered and vegetated areas, and carry insufficient sediment to have yet filled their incised valleys to the level of the Amazon River bed. The discrepancy between the ability of these rivers to erode and aggrade has produced drowned-river-valley lakes (rias) at their confluences with the Amazon River (Figure 4.1).

---

[1]This chapter was accepted by *Sedimentology* as: Fricke, A.T., Nittrouer, C.A., Ogston, A.S., Nowacki, D.J., Asp, N.E., Souza Filho, P.W.M, and da Silva, M.S., River tributaries as sediment sinks: Processes operating where the Tapajós and Xingu Rivers meet the Amazon tidal river, and is in revision.

The ria basins make the connection between the tributaries and the mainstem of the Amazon less straightforward than a typical fluvial confluence. Because of their low sediment loads, both the Tapajós and Xingu Rivers have been unable to reach an equilibrium cross-section (see Wilson, 1973) within the ria basins. The difference between the observed cross section (lake-like) and an equilibrium cross section (river-like) can be considered the accommodation space available in the systems. Substantial accommodation space is not typically found at river confluences because both river and tributary usually develop equilibrium cross-sections at a more similar pace to each other. Consequently, in most confluences, water and the sediment it carries, will move downstream over all but the shortest timescales (e.g., a seasonal flood pulse, or rising tide). This is not the case in the Tapajós or Xingu Rias, where ample accommodation space remains to be filled, and sediment from both tributary and mainstem contributes to that infilling (Sioli, 1984; Irion, 1984). These rias offer a rare opportunity to observe the sedimentary processes acting to fill a pair of late-Pleistocene incised valleys that experience both tidal and fluvial influence.

The processes acting in these important gateways through which 2% of global fluvial freshwater flows are poorly understood, and results discussed in existing literature are inconsistent. This research aims to clarify the role the Tapajós and Xingu Rias play in the Amazon system by: (1) determining the distribution of tributary- and Amazon-derived sediment within the ria basins, (2) identifying the sediment-transport mechanisms that deliver tributary- and Amazon-derived sediment to the ria basins, and (3) estimating rates of sediment accumulation within both rias.

2.2 Background

2.2.1 Physical Setting

The Amazon River is the largest single fluvial source of freshwater and sediment to the ocean (Milliman and Farnsworth, 2011; Nittrouer et al., 1995b). The lowest gauging station on the Amazon River is in the town of Óbidos at the farthest upstream extent of tidal propagation, roughly 800 km from the Atlantic Ocean (Figure 4.1). Estimates of water, sediment, and dissolved loads are based primarily on measurements from this gauging station. Very little is

known about the transformation of the loads measured at Óbidos along this 800-km path to the sea. In addition to exchange between the Amazon River and its vast floodplain along this tidal reach, the Amazon River receives inputs from the Tapajós, Xingu, and other smaller rivers, which contribute ∼10% to its water discharge.

Following the classification scheme outlined in Sioli (1984), both the Tapajós and Xingu Rivers are clearwater rivers, containing little in the way of the tannins characteristic of blackwater rivers (e.g, Rio Negro), or the suspended sediment characteristic of whitewater rivers (e.g., Amazon River). Because of their low sediment loads, the Tapajós and Xingu Rivers have not filled their incised valleys produced during the last glacial period Sioli (1984). The Tapajós Ria is ∼150 km in length with an average width of ∼15 km, and the Xingu Ria is smaller with a length of ∼100 km and an average width of ∼10 km (Figure 4.1).

2.2.2 Previous Work

Previous work has introduced the concept that the large Tapajós and Xingu Rias act to modify the sedimentary signal from each tributary that ultimately reaches the Amazon River, but the interpretations are in many cases inconsistent. Sioli (1984) describes a 'Sedimentation Zone' at the upstream end of the rias, downstream of which the water is free of sediment. Even so, it is reported that the Tapajós and Xingu Rivers individually contribute ∼1% (∼5–10Mt) to the sediment load of the Amazon River (Filizola and Guyot, 2009; Wittmann et al., 2011). Additionally, a core collected ∼100 km downstream of the head of the Tapajós Ria contains ∼40 m of Holocene sediment, which the authors attribute to input from the Tapajós River (Irion, 1984; Irion et al., 2006, 2010). These findings are contradictory, as the Tapajós River cannot deposit nearly all of its sediment upon entering the lake-like ria, produce a 40-m thick deposit 100 km farther downstream, and contribute millions of tons of sediment to the Amazon River each year. Relatively little has been written about the sedimentary history of the Xingu Ria, although it is thought to function in a similar manner to the Tapajós, perhaps with subtle differences due to an increased tidal range (Archer, 2005).

In addition to describing how sediments from the Tapajós and Xingu tributaries reach

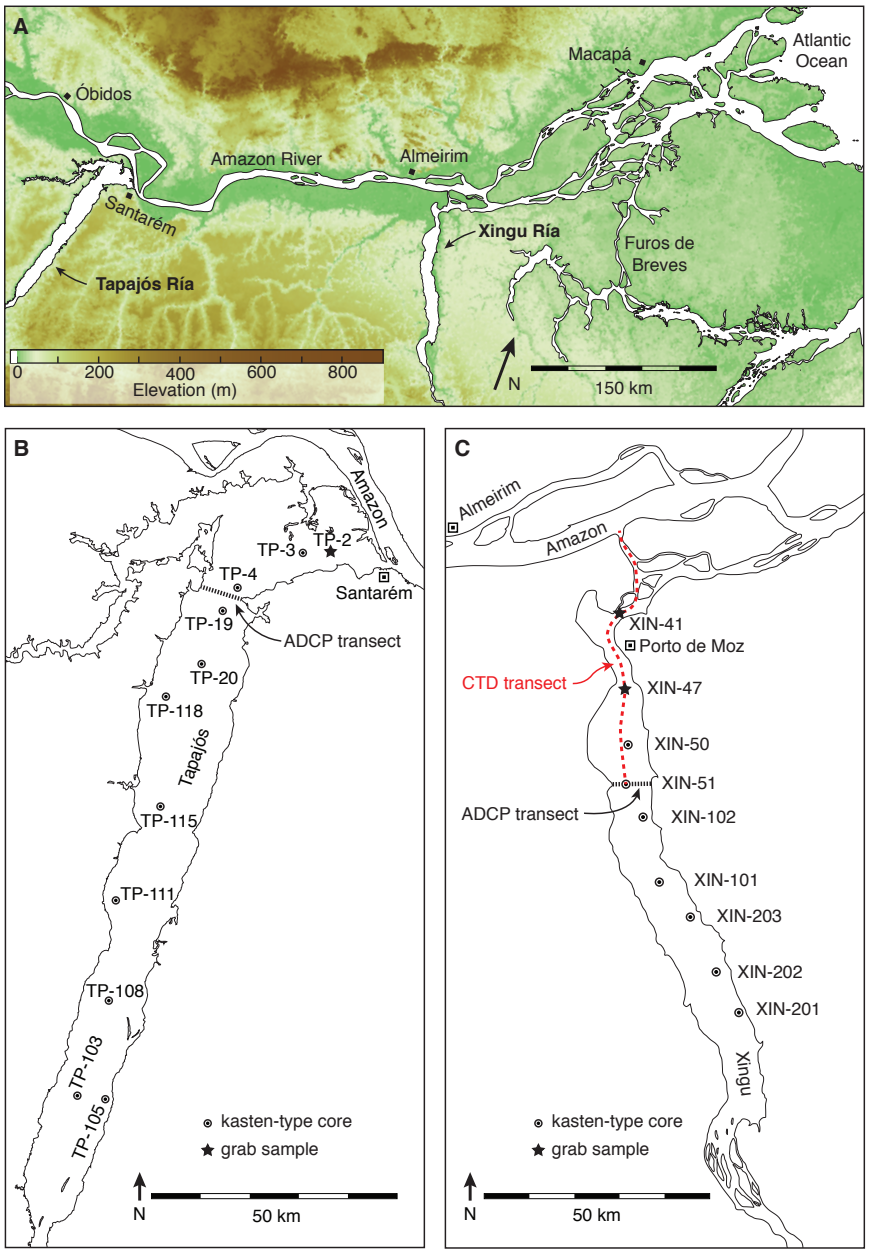

Figure 2.1: Maps of the Tapajós and Xingu Rias and their location within the lower Amazon River. (A) The lower Amazon River showing the location of the Tapajós and Xingu Rias. Note the low-relief floodplain along the Amazon River, and highlands bordering the Tapajós and Xingu Rias. Land-surface elevation from the Shuttle Radar Topography Missions, with major water bodies shown in white. (B) The Tapajós Ria showing the locations of 10 kasten-type sediment cores, and 1 surface grab sample. Also shown is the location of the ADCP transect used to calculate discharge. (C) The Xingu Ria showing the locations of 7 kasten-type sediment cores and two surface grab samples. Also shown is the location of the ADCP transect used to calculate discharge, and the CTD transect used to examine thermal structure of the water column.

the Amazon, authors have documented ways in which waters from the Amazon River move upstream into the rias, and deposit material there. Archer (2005) mentions the bird-foot delta building from the Amazon River into the Tapajós Ria, which Wallace (1853) attributes to a difference in water-surface elevation between the Amazon River and the Tapajós Ria. Schematic geologic cross sections through the Tapajós Ria from Irion (1984) and Irion et al. (2010) suggest Amazon-derived sediment extends ∼30 km into the Tapajós Ria in the vicinity of the bird-foot delta. These limited investigations of the Tapajós and Xingu Rias yield questions regarding the origin, transport, and fate of sediment in the rias, which are the focus of this paper.

2.3 Methods

Measurement and sampling of the Tapajós and Xingu Rias occured over four cruises on the *N/M Rey Benedito* timed to coincide with low water (November 2012), rising water (March 2014), high water (June 2013), and falling water (August 2011) conditions of the Amazon mainstem.

2.3.1 Ship-Based Measurements and Sampling

Water-velocity measurements throughout the water column were collected along ∼8-km wide transects in both the Tapajós and Xingu Rias using a ship-mounted 600-kHz RD Instruments acoustic Doppler current profiler (ADCP) [Teledyne RD Instruments, Poway, CA, USA] (Fig. 1). These ADCP measurements involved continuous repeated crossings over a ∼13-hr period in order to capture one complete semidiurnal tidal cycle. Instantaneous discharge was determined for each transect crossing by summing the ADCP velocity measurements and multiplying by the cross-sectional area of the channel as measured by the ADCP. Residual (tidally averaged) discharge was calculated by integrating the instantaneous discharge over a complete 12.4-hr semidiurnal tidal cycle.

Measurements of conductivity, temperature, depth, and turbidity were made using a RBR conductivity, temperature, and depth sensor (CTD) [RBR Ltd., Ottawa, ON, Canada] with calibrated OBS 3+ optical backscatter sensor [Campbell Scientific Inc., Logan, UT, USA]. The OBS response voltage was converted to suspended-sediment concentration (SSC) by

applying a calibration based on in-situ water samples that were filtered on the ship, and dried and weighed in the lab. Water depth was recorded using a Lowrance echosounder [Lowrance Electronics, Tulsa, OK, USA]. In the Tapajós Ria, ten sediment cores were collected every ∼15 km along a ∼120-km transect between the upstream limit of the ria and the confluence with the Amazon River (Figure 2.1) using a 1.5-m kasten-type sediment corer. Seven cores were collected in the Xingu Ria along a 65-km transect originating ∼20 km south of the village of Porto de Moz (Figure 2.1). Surface sediment samples were collected using van Veen and Shipek grab samplers.

2.3.2 Core Processing

Cores were opened and processed on the ship. A 2.5-cm-thick slab was removed along the full length of each core, and X-rayed in the field using a portable x-ray system. The sediment in each core was cut into 2-cm intervals and bagged for radiochemical, mineralogical, and grain-size analyses. Wet samples were disaggregated using a 0.05% sodium hexametaphosphate ($[NaPo_3]_6$) dispersant solution and sonicating bath. Disaggregated samples were wet sieved through a 64-um (4-ϕ) sieve. Grain-size distributions of the mud fraction from each sample (<64 μm) were determined using Micromeritics Sedigraph 5100, 5120, and 5125 particle sizers [Micromeritics Instrument Corporation, Norcross, GA, USA] in the laboratory.

Sediment accumulation rates were determined using the naturally occurring radioisotope ^{210}Pb, a geochronological method that has seen considerable use elsewhere in the Amazon system (e.g. Kuehl et al., 1986; Allison et al., 1995b; Kuehl et al., 1996; Aalto and Nittrouer, 2012). Following the technique described by Nittrouer et al. (1979), the activity of ^{210}Pb is determined by measuring the activity of its granddaughter, ^{210}Po, relative to a calibrated spike of ^{209}Po, via alpha spectrometry. Because of its 22.3-year half-life, ^{210}Pb can be used to constrain the century-scale sediment-accumulation rate (S):

$$S = \frac{\lambda z}{\ln(\frac{A_0}{A_z})}$$

where, λ is the decay constant for ^{210}Pb, A_0 and A_z are excess ^{210}Pb activities at two points within the region of log-linear decay, and z is the difference in depth between A_0 and A_z.

To minimize variation in ^{210}Pb activity due to down-core changes in grain size, activities were normalized to percent mud (<64 μm) in each sample. Excess ^{210}Pb activity is that above the supported level of ^{210}Pb produced from in-situ decay of ^{226}Ra in the sediment. The supported level of ^{210}Pb in each core was determined by comparing the total ^{210}Pb activities in the deepest interval of each core with the ^{214}Bi activity (A. Jalowska, pers. comm., 2015), which is in secular equilibrium with ^{226}Ra measured by gamma spectrometry (Benninger and Wells, 1993). Measurements of ^{214}Bi were made in the upper 1 cm of each core, and a uniform activity is assumed over the length of each core. In cases where the activity of ^{214}Bi, and therefore supported ^{210}Pb, is less than the lowest ^{210}Pb activity measured via alpha spectrometry, the supported level of ^{210}Pb determined from ^{214}Bi gamma decay is used. If the lowest ^{210}Pb activity measured via alpha spectrometry is less than the ^{214}Bi-derived supported level, but within the 1σ confidence limits of the 1σ-derived activity (A. Jalowska, pers. comm., 2015), the lowest alpha-derived activity is used as the supported level.

Clay mineralogy for the <2-μm fraction was determined by semi-quantitative X-ray diffraction. Bulk sediment samples were dispersed and the <2-μm fraction isolated via settling. Oriented aggregate slides were prepared using the Millipore Filter Transfer Method (Moore and Reynolds, 1997) and analyzed in a Rigaku Ultima IV X-ray Diffraction System [Rigaku Corporation, Tokyo, Japan].

2.4 Results

2.4.1 Hydrodynamics

The hydrodynamics in the Tapajós and Xingu Rias are governed by forcing that varies on seasonal and tidal timescales. Peak discharge of the Tapajós and Xingu Rivers occurs in April, roughly two months before the peak water discharge of the Amazon River, which occurs in May through June (Figure 2.2) (Meade et al., 1985). Superimposed on this seasonal cycle are semidiurnal (twice daily) tidal fluctuations that influence hydrodynamics within the rias. In addition to seasonal and tidal changes in water level, hydrodynamics in the Amazon, Tapajós, and Xingu are affected by the different character of their waters in terms

of suspended-sediment concentration and temperature.

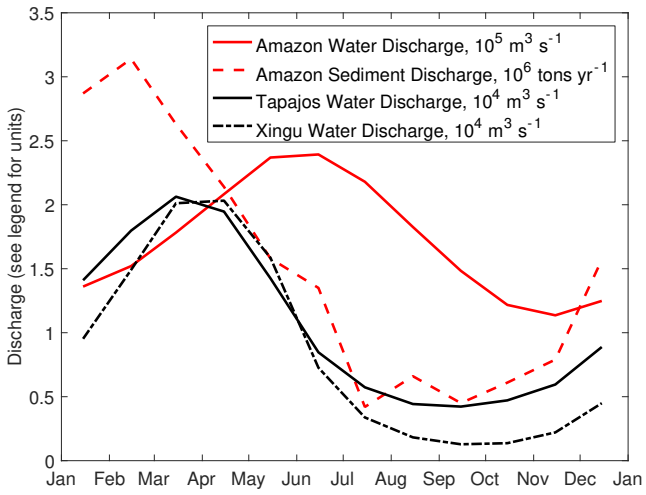

Figure 2.2: Mean annual water discharge for the Amazon, Tapajós, and Xingu Rivers, and mean annual sediment discharge for the Amazon River. Mean annual discharge for the Amazon River is calculated from 34 years of data collected at Óbidos between 1928 and 1983. Mean annual discharge for the Tapajós River is derived from 20 years of data collected at Jatoba between 1973 and 1994. Mean annual discharge for the Xingu River is calculated from 26 years of data collected at Altamira between 1971 and 1997. Water-discharge data from sage.wisc.edu, and Amazon sediment discharge data from Filizola and Guyot (2009).

Velocity and Discharge Measurements

The Tapajós Ria has a greater discharge and experiences weaker tidal forcing than the Xingu Ria. Although peak discharges of the two rivers can be of a similar magnitude, low flow of the Xingu River is typically ∼20% that of the Tapajós (Figure 2.2, Table 2.1). In addition to the difference in typical seasonal discharge, the Xingu experiences greater tidal forcing than the Tapajós, resulting in markedly different discharge conditions over individual tidal cycles. In environments where tidal oscillations are superimposed on river outflow, a distinction must be made between the tidally averaged flow (i.e., residual flow), and instantaneous measurements of discharge at various stages of the tide (see Section 2.3.1). During low flow of the Tapajós and Xingu Rivers, the Tapajós Ria experiences maximum changes in instantaneous discharge due to tidal fluctuations that are approximately equal to

the residual discharge, while in the Xingu Ria instantaneous discharge varies by ±10 times the residual discharge (Table 2.1). During high-flow of the Tapajós and Xingu Rivers, the instantaneous discharge in the Tapajós Ria varies by <4% of the residual discharge, while in the Xingu, tidal fluctuations lead to changes in instantaneous discharge of ∼20% of the residual discharge.

In addition to patterns in residual discharge, instantaneous velocity measurements vary between rías and seasons. Over the course of a tidal cycle during low-flow conditions in the Tapajós, typical downstream flow velocities in the deeper eastern channel are 10–20 cm s^{-1}, while upstream flow over the shallower western part of the ría is 10–15 cm s^{-1}. During high-flow conditions, downstream-directed flow in the deeper channel has a velocity of 20–35 cm s^{-1}, while upstream flow near the extreme western margin has a velocity of 5–10 cm s^{-1} over the course of a tide. The Xingu Ría experiences ría-wide flow reversal during low-discharge conditions (Table 2.1) and flow velocities range between −15 and +15 cm s^{-1} depending on the phase of the tide. During high-discharge periods, flows do not reverse and flow is directed almost entirely downstream, with velocities of 10–30 cm s^{-1} over a tidal cycle.

The Tapajós Ria experiences persistent upstream residual flow over the shallower western part of the basin and along the extreme eastern margin of the ria in the vicinity of the ADCP transect (Figure 2.3). A greater fraction of the cross section experiences upstream flow during low-flow conditions (Figure 2.3, Table 2.1). Residual upstream flow is observed in the Xingu Ria only during low-flow conditions (Figure 2.4A). Unlike the upstream flow in the Tapajós Ria, which is present throughout the tide, upstream flow in the western Xingu Ria occurs only during flood tides, which are preferentially routed along the western side of the ria.

Character of Water Masses

Owing to their different sources, the character (e.g., temperature, suspended-sediment concentration) of waters from the Amazon, Tapajós, and Xingu are distinct from each other, and vary throughout the year. Suspended-sediment concentration is consistently greater in the Amazon River (50–100s mg L^{-1}) than in the Tapajós or Xingu Rias (<10 mg L^{-1}). Although the Amazon River is always observed to be more sediment-laden than either tribu-

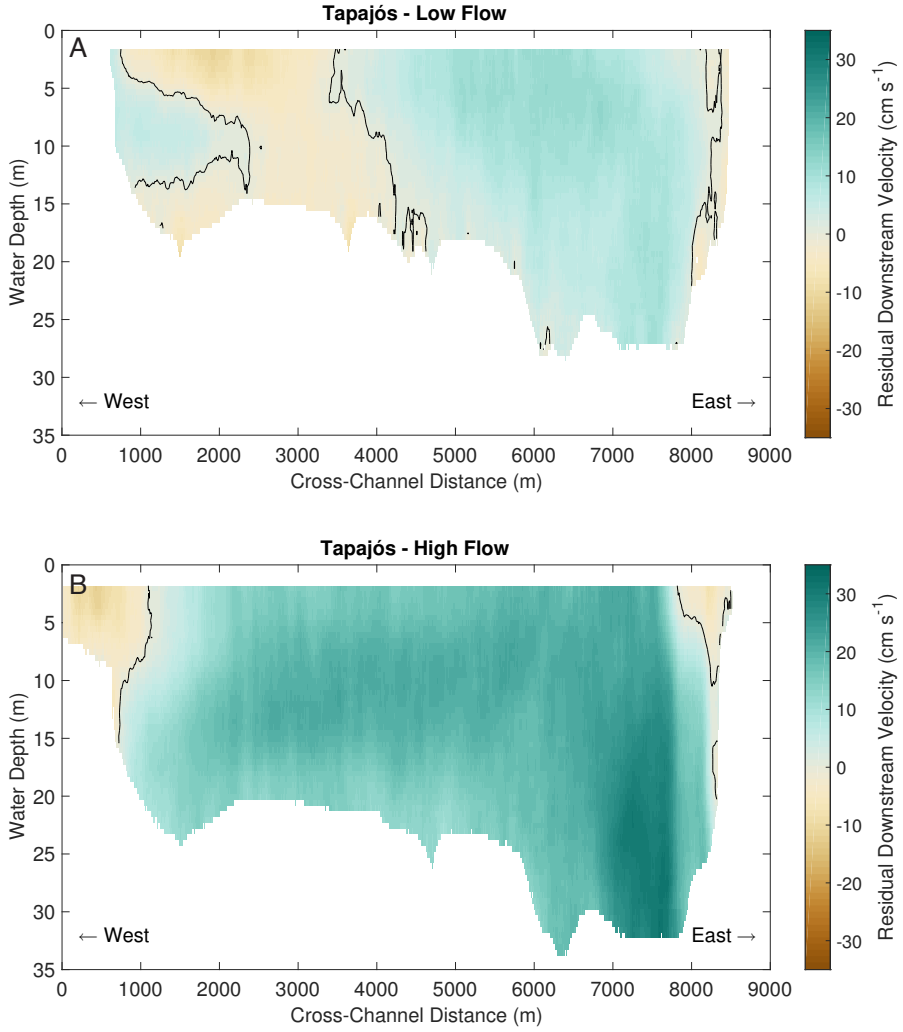

Figure 2.3: Cross sections of residual velocity from the Tapajós Ría during low- and high-discharge conditions. Green colors represent downstream residual velocity and brown colors represent upstream residual velocity. The zero-velocity contour is shown in black. (A) Data from the Tapajós Ría collected over 12.4 hours on 31 October 2012 during low discharge of the Tapajós River (6000 m^3 s^{-1}, Table 2.1) . (B) Data from the Tapajós Ría collected over 12.4 hours on 18 March 2014 during high discharge of the Tapajós River (32000 m^3 s^{-1}, Table 2.1).

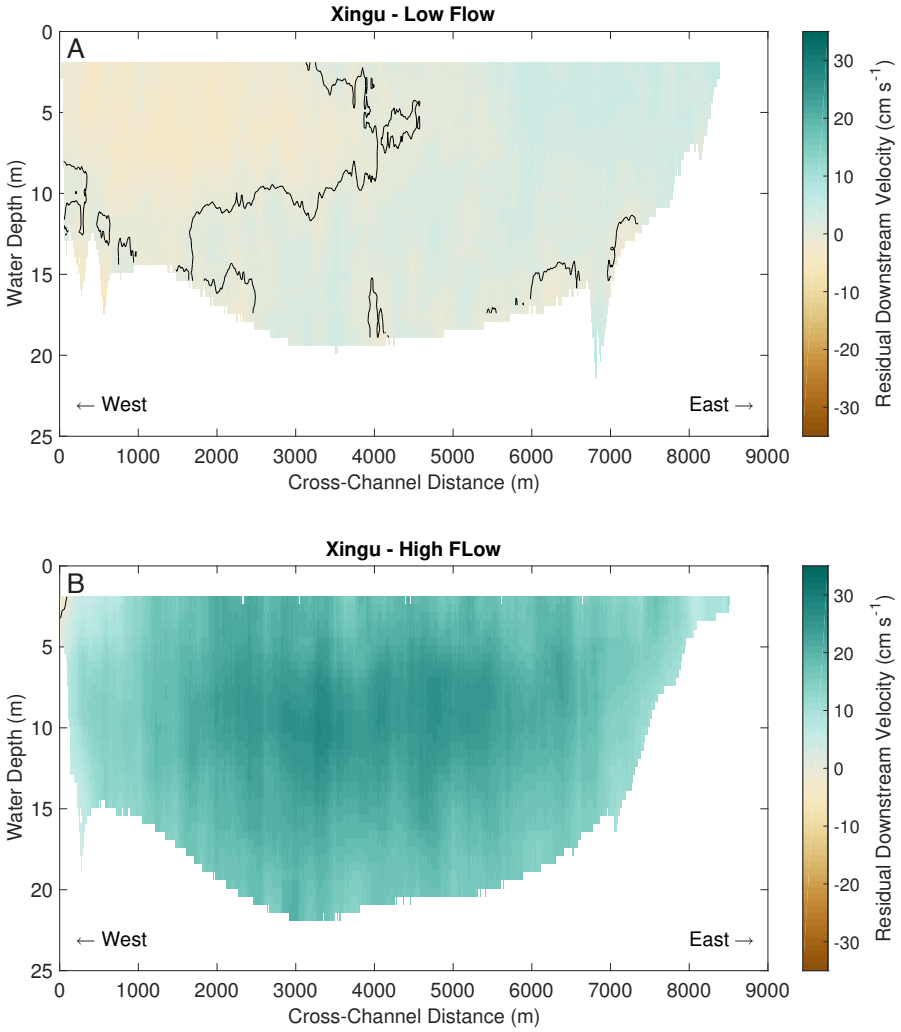

Figure 2.4: Cross sections of residual velocity from the Xingu Ría during low- and high-discharge conditions. Green colors represent downstream residual velocity and brown colors represent upstream residual velocity. The zero-velocity contour is shown in black. (A) Data from the Xingu Ría collected over 12.4 hours on 25 August 2011 during low discharge of the Xingu River (1250 m^3 s^{-1}, Table 2.1). (B) Data from the Xingu Ría collected over 12.4 hours on 22 March 2014 during high discharge of the Xingu River (25000 m^3 s^{-1}, Table 2.1).

		Tapajós Ria	Xingu Ria
Low Flow	Residual Discharge (m^3 s^{-1})	6000	1250
	Maximum Discharge (m^3 s^{-1})	11000	10500
	Minimum Discharge (m^3 s^{-1})	30	-10500
High Flow	Residual Discharge (m^3 s^{-1})	32000	25000
	Maximum Discharge (m^3 s^{-1})	33000	30000
	Minimum Discharge (m^3 s^{-1})	30500	19500

Table 2.1: Summary of the hydrodynamic conditions in the Tapajós and Xingu Rias during periods of low and high discharge of each tributary. Low-discharge measurements were made on 31 October 2012 in the Tapajós Ria and on 25 August 2011 in the Xingu Ria. Both measurement periods capture the extended low-flow period for the Tapajós and Xingu between late August and late October (Figure 2.2). High-discharge measurements were made on 18 March 2014 in the Tapajós Ria and on 22 March 2014 in the Xingu Ria. Residual discharge is the tidally averaged discharge over a 12.4 hour period, while maximum and minimum discharge values are instantaneous discharges associated with tides.

tary, the relative temperature signatures of the Amazon, Tapajós, and Xingu vary seasonally (Table 2.2). During falling stage of the Amazon mainstem (low stage of the tributaries), the Amazon is cooler than either the Tapajós or Xingu Ria. During the other three stages (low, rising, high) of the Amazon River, the Tapajós and Xingu Rias have either slightly warmer or similar temperatures to the Amazon mainstem (no data is available for the Tapajós confluence during high stage of the Amazon River) (Table 2.2).

Differences in temperature and suspended-sediment concentration affect the way in which Amazon and tributary water masses mix. When the Amazon River is cooler than the Xingu Ria, an underflow of Amazon water is observed to extend 30–40 km from the mainstem of the Amazon River into the Xingu confluence area (Figure 2.5A), reaching ∼10 km upstream of the town Porto de Moz (Figure 2.1). When the Amazon River is warmer than the Xingu Ria, this underflow is not observed, and there is a strong horizontal gradient in temperature between the two water masses (Figure 2.5B). The water masses can also be distinguished based on differences in suspended-sediment concentration, given the roughly order-of-magnitude difference between the white-water Amazon and the clear-water Xingu.

However, unlike temperature, SSC is not a conservative tracer (lacking in situ sources or sinks), as it can be added or removed via settling or resuspension, so temperature is used here to differentiate water masses. Underflows of Amazon water into the Tapajós Ria were not observed in the three seasonal stages where CTD transects in the confluence area were performed (August 2011, November 2012, and March 2014).

		Tapajós-Amazon Confluence		*Xingu-Amazon Confluence*	
River Stage		Temperature (°C)		Temperature (°C)	
Amazon	Tributary	Tapajós Ría	Amazon River	Xingu Ría	Amazon River
Falling	Low	30.3	**29.9**	30.2	**30.0**
Low	Low	**30.3**	30.8	**29.8**	30.7
Rising	High	**27.9**	28.2	**27.8**	28.3
High	Falling	–	–	29.1	29.1

Table 2.2: Summary of water temperatures in the Tapajós and Xingu Rías and the Amazon River near each confluence during the four study periods. Temperature data were not collected in the Tapajós during high-water conditions. Temperatures for each ría are the mean of water temperatures below the thermocline from a CTD cast at ∼40 km from the Amazon River. Temperatures for the Amazon River represent a mean throughout the well mixed water column from a CTD cast at each confluence. The cooler water temperature from each pair is shown in bold.

.

2.4.2 Sedimentology

Grain size

In the central parts of the ria basins sediment is very fine, with clay typically representing >75% of the mass. The coarsest sediment is found in cores collected nearest the Tapajós or Xingu bayhead deltas (e.g. cores TP-105, TP-103, Fig. 6), and in cores collected nearest the confluence of each ria with the Amazon River (e.g., cores TP-3, XIN-50, Figures 2.6 and 2.7). Grain size is relatively consistent over the ∼1-m length of most cores (Figures 2.6 and 2.7). This is especially true for cores collected in the central parts of the ria basins. X-radiographs

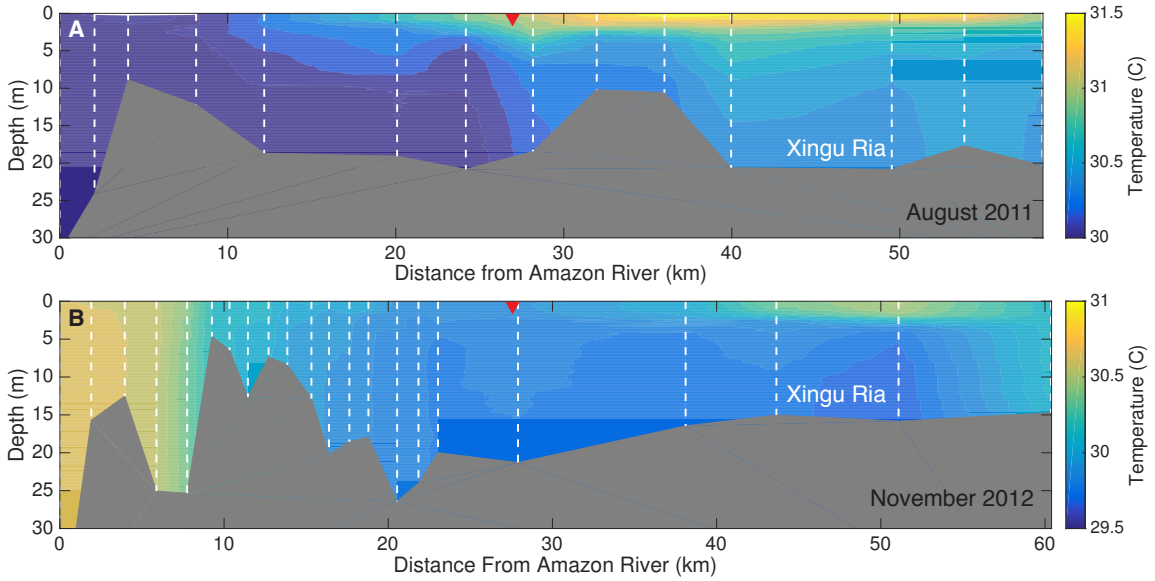

Figure 2.5: Cross sections of water temperature along a ∼60-km transect from the XinguÐAmazon confluence into the Xingu Ria. (A) Temperature cross-section collected during August 2011 (low discharge of the Xingu River, falling discharge of the Amazon River). (B) Temperature cross-section collected during November 2012 (low discharge of the Xingu River, low discharge of the Amazon River). Temperature data from individual CTD casts (white dashed lines) have been interpolated between cast locations. CTD casts reached the bed of the ria and are used to define the bathymetry along each transect. CTD casts did not necessarily capture the maximum thalweg depth at each location, so bathymetric highs should not be considered shoals, and variations in along-transect bathymetry between panels (A) and (B) are due to differences in ship positioning. Red triangles mark the approximate location of the village of Porto de Moz (see Figure 2.1C)

show no evidence of bioturbation (e.g., burrows), but reveal very little physical structure within cores due to the homogeneous nature of the sediment and pervasive biogenic gas in the ria sediment.

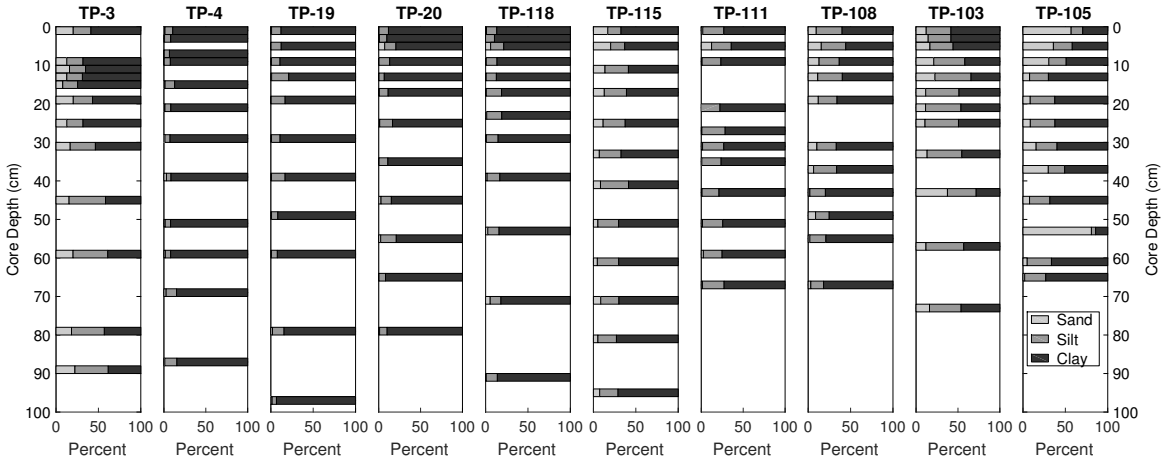

Figure 2.6: Sediment grain-size distributions over the lengths of ten kasten-type cores from the Tapajós Ría. Plots are arranged from nearest the Amazon-Tapajós confluence (left) to most upstream in the Tapajós Ría (right) (see Figure 2.1B). Percent sand (light gray), silt (medium gray), and clay (dark gray) are shown for selected 2-cm intervals. The central part of the Tapajós basin is characterized by the finest sediments, with coarser sediment present nearer the Amazon and Tapajós Rivers.

Sediment Accumulation

Total ^{210}Pb activities in both rias are high compared to most fluvial or coastal-ocean values, and exceed 20 dpm g^{-1} near the sediment-water interface. The supported activity of ^{210}Pb in sediment (from in-situ decay of ^{226}Ra) varies spatially within the rias, so supported levels were determined for each core site (see Section 2.3.2). Sediment-accumulation rates in the Tapajós Ria, as determined by ^{210}Pb geochronology, are between 0.2 cm y^{-1} and 1.9 cm y^{-1} (Figure 2.8). The ^{210}Pb profile in core TP-111 showed no log-linearity between activity and depth, and is therefore not used to calculate an accumulation rate. Accumulation rates in the Xingu Ria are between 0.3 cm y^{-1} and 2.3 cm y^{-1} (Figure 2.9). With the exception of the cores collected nearest the upstream limit of both rias, sediment-accumulation rates

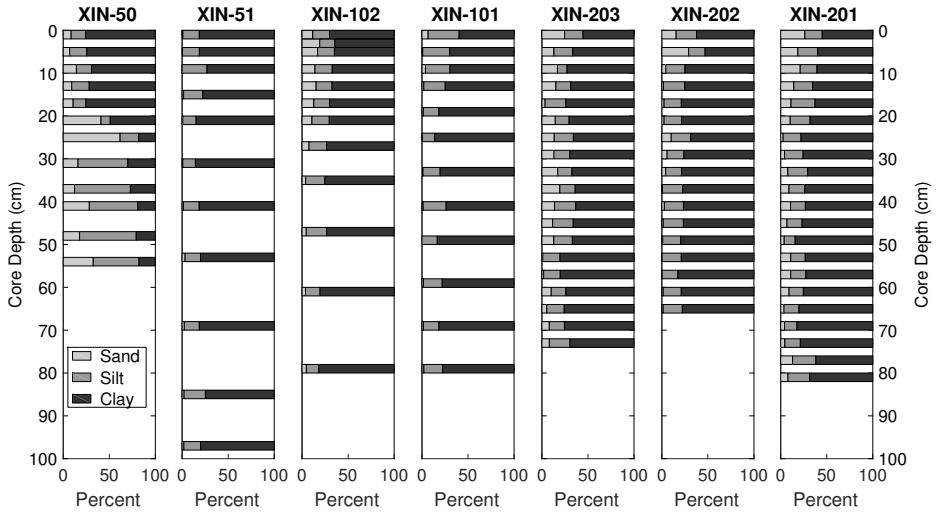

Figure 2.7: Sediment grain-size distributions over the lengths of seven kasten-type cores from the Xingu Ría. Plots are arranged from nearest the Amazon-Xingu confluence (left) to most upstream in the Xingu Ría (right) (see Figure 2.1C). Percent sand (light gray), silt (medium gray), and clay (dark gray) are shown for selected 2-cm intervals. Sediment grain size is very fine throughout the Xingu basin, with some some coarser layers near the Amazon River (XIN-50).

are lowest near the up- or downstream limits of the basins, and increase toward the central part of each ria.

2.4.3 Clay Mineralogy

The mineralogy of the <2-μm fraction of surface sediments from both the Tapajós and Xingu Rias is dominated by kaolinite, with lesser amounts of illite. Smectite is present in only two of 20 samples analyzed (Figure 2.10). Samples with the least kaolinite occur nearest the Amazon River in both the Tapajós and Xingu Rias. With some exceptions, sediment in both rias exhibit a reduction in kaolinite and an increase in either illite or smectite toward the Amazon River.

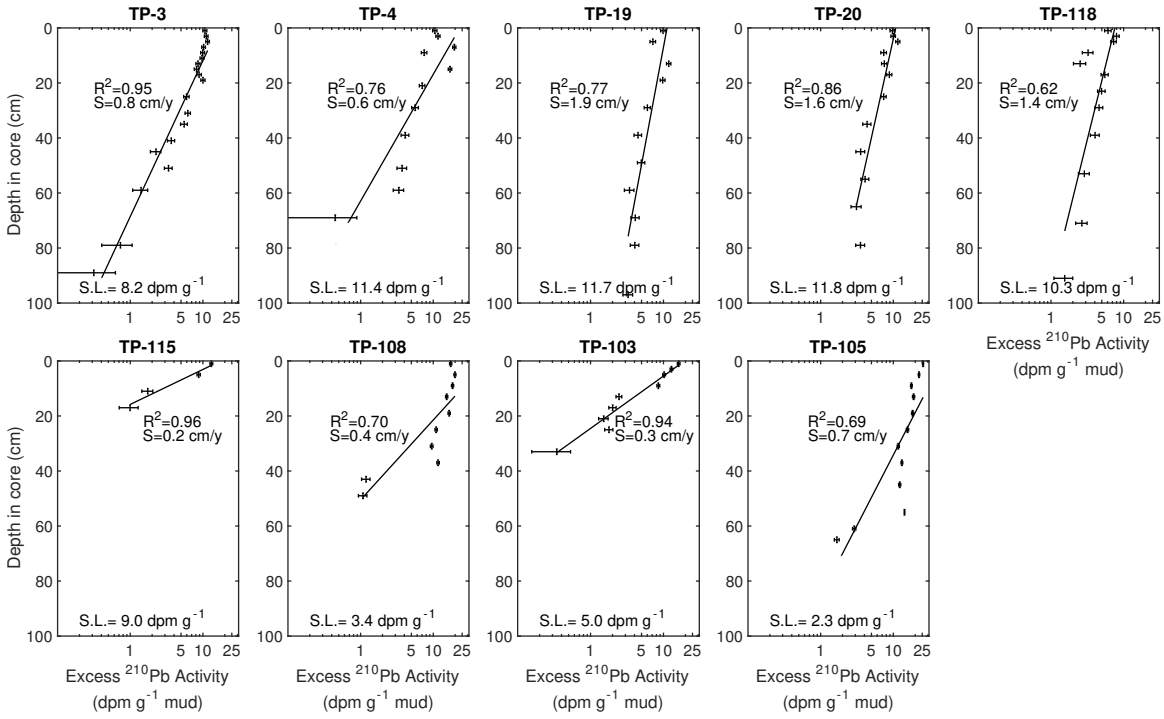

Figure 2.8: Profiles of excess ^{210}Pb from 9 kasten-type cores from the Tapajós Ría. Plots are arranged from nearest to the Amazon-Tapajós confluence (upper left) to most upstream in the Tapajós Ría (lower right) (see Figure 2.1B). Log-linear regressions and correlation coefficients (R^2) are determined for the region of log-linear decay, and the sediment accumulation rate (S) is shown. The supported level (S.L.) of ^{210}Pb is indicated at the bottom of each plot.

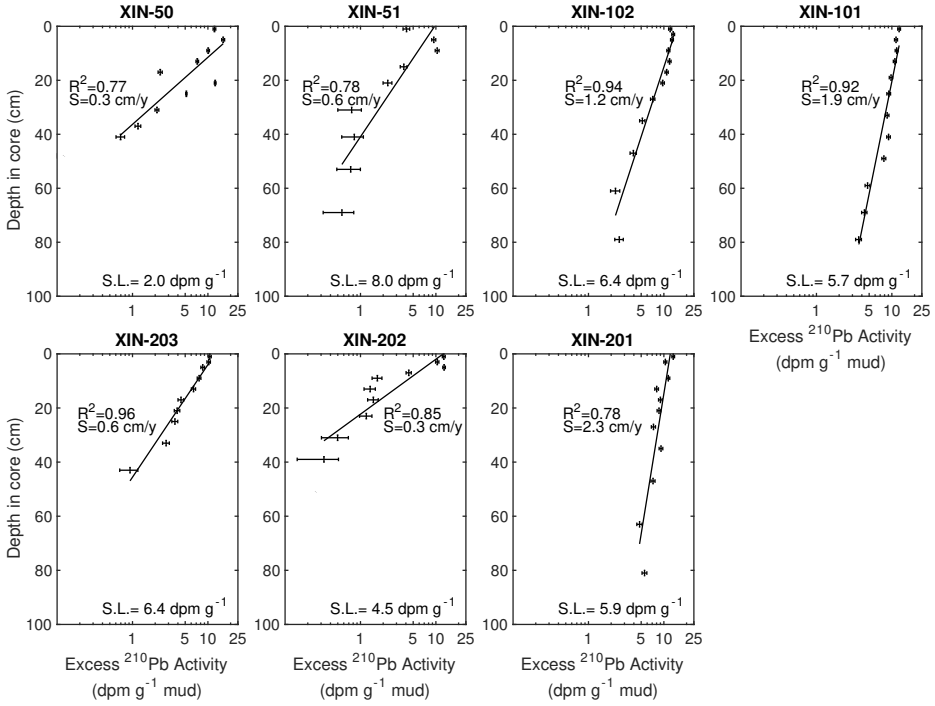

Figure 2.9: Profiles of excess ^{210}Pb from 7 kasten-type cores from the Xingu Ría. Plots are arranged from nearest to the Amazon-Xingu confluence (upper left) to most upstream in the Xingu Ría (lower right) (see Figure 2.1C). Log-linear regressions and correlation coefficients (R^2) are determined for the region of log-linear decay, and the sediment accumulation rate (S) is shown. The supported level (S.L.) of ^{210}Pb is indicated at the bottom of each plot.

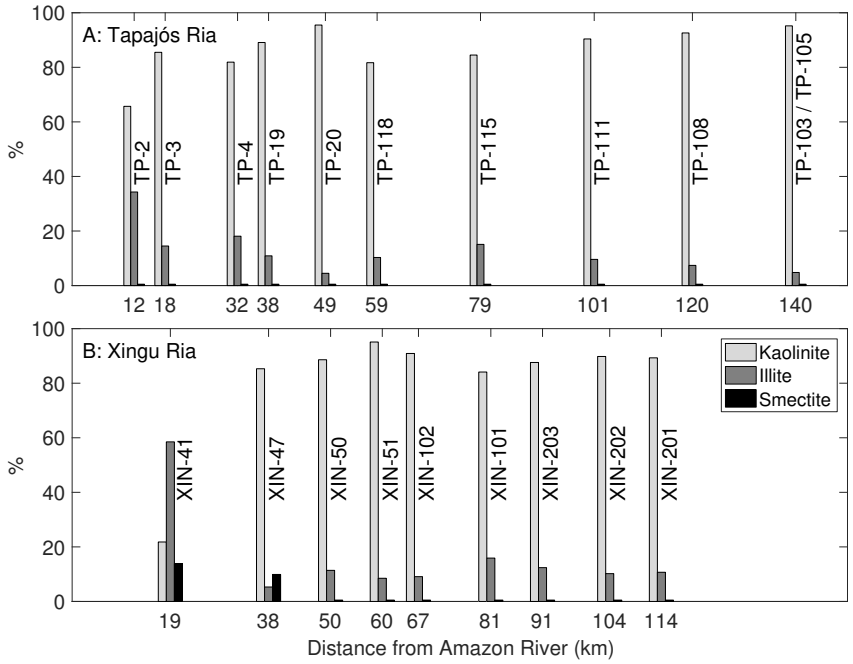

Figure 2.10: Bar graphs of clay-mineral composition from the <2-μm fraction of 20 surface sediment samples from the Tapajós and Xingu Rías shown in terms of percent kaolinite (light gray), percent illite (medium gray), and percent smectite (black). Data are arranged from nearest to the tributary–Amazon confluence (at the left) moving upstream in the ría toward the right. (A) Data from the Tapajós Ría are shown to contain no smectite, with the greatest percent illite and lowest percent kaolinite near the Amazon River. A single set of bars representing the mean composition of TP-103 and TP-105 is shown because both cores were collected at the same distance from the Amazon (see Figure 2.1B), and the difference in clay mineral-composition is <0.1% between the two samples. (B) Data from Xingu Ría showing that samples from upstream part of the basin (XIN-50–XIN201) are kaolinite rich, with lesser amounts of illite, and that the two samples nearest the Amazon River have a distinct signature that includes smectite (see Figure 2.1C).

2.5 Discussion

2.5.1 Sediment Sources

The distribution and character of sediment in the Tapajós and Xingu Rias suggest that sediment is delivered from both the tributary (Tapajós or Xingu River), and from the Amazon River. Sediment fines northward away from the Tapajós bayhead delta (Figures 2.6, 2.11). This can be seen in general decreases in the mean mass percents of silt and sand between the upstream limit of the coring transect to within ∼30 km of the Amazon–Tapajós confluence. This trend reverses in the downstrean ∼30 km of the Tapajós Ria, where coarsening is observed toward the Amazon River (Figure 2.11). The coarsening of sediment toward the Amazon–Tapajós confluence is consistent with an Amazonian sediment source for the lower ∼30 km of the Tapajós Ria, as sediment carried by the Amazon River is coarser than the distal deposits associated with either the Tapajós or Xingu Rivers (see Meade, 1985). Clay mineralogy from these same sample locations (TP-2, TP-3, and TP-4) shows a lesser kaolinite fraction also consistent with influence from an Amazonian source (Figure 2.10A). Clays in the Amazon River are kaolinite-poor, with samples from Óbidos containing 16% kaolinite, 16% illite, and 58% smectite (Guyot et al., 2007), while lowland tributaries draining shield terranes, such as the Tapajós and Xingu Rivers, carry almost exclusively kaolinite (Keim et al., 1999; Guyot et al., 2007).

A fining trend away from the Xingu bayhead delta is not observed, although a lack of bayhead-proximal cores may hinder the identification of such a trend. In the Xingu Ria, the nearest core to the bayhead delta (XIN-201) is ∼20 km from the upstream limit of the ria, while in the Tapajos Ria, cores TP-103 and TP-105 were collected ∼10 km from the upstream limit of the ria and contain significantly coarser sediment. Sediment does coarsen toward the Amazon–Xingu confluence in the lower ∼40 km of the Xingu system, as evidenced by increases in either the silt or sand fractions (Figure 2.11B). Mineralogy of the <2-μm clays from the two lowermost sites in the Xingu Ria (XIN-40, XIN-47) includes smectite, and less kaolinite than samples farther upstream (Figure 2.11B). Both of these signatures are consistent with greater influence from the Amazon River. The combination of coarser grain sizes and distinct clay-mineral composition in the lower 30–40 km of the Tapajós and

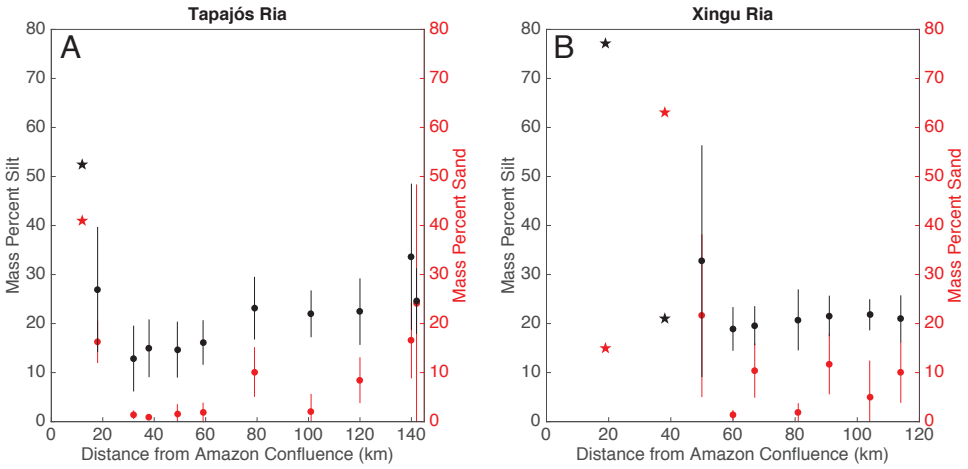

Figure 2.11: Sediment grain size from the Tapajós and Xingu Rías. Black markers indicate the mean mass percent silt (coarser than 8 ϕ, 4 μm) in each core, and the red markers indicate the mean mass percent sand in each core. Black and red dots represent the mean of data from multiple samples from each core (see Figures 2.6, 2.7), and the vertical lines indicate one standard deviation from the mean. Black and red stars represent data from single grab samples (A) Data from the Tapajós Ría. (B) Data from the Xingu Ría.

Xingu Rias indicates a contribution of Amazon-derived sediment to these areas.

2.5.2 Mechanisms of sediment delivery

Barotropic Flows

Barotropic flows are driven by gradients in water-surface elevation, and move water and sediment from the Amazon River into the Tapajós and Xingu Rias on seasonal and tidal timescales. At the Amazon–Tapajós confluence, the seasonal change in water-surface elevation of the Amazon is >5 m, while the tidal range varies from 5 cm during high discharge of the Amazon to 15 cm during low discharge (Freitas et al., 2017). The large seasonal signal, combined with the asynchrony in the hydrographs of the Amazon and the Tapajós Ria (Figure 2.2), favors barotropic flows acting on seasonal timescales. The clearest example of this is the bird-foot delta that originates at a crevasse through the levee separating the Amazon River and Tapajós Ria, and extends ∼40 km into the Tapajós Ria (Figure 2.12).

Field and satellite observations of the birdsfoot delta suggest this feature is active during all seasonal conditions, but is likely most active during the greatest stage difference between the Amazon and Tapajós, which occurs during high discharge of the Amazon River after the Tapajós River has begun to fall.

In the Xingu Ria, seasonal and tidal changes in water-surface elevation are of a similar magnitude, with a seasonal change of ∼2 m, compared to a tidal range of ∼40 cm during high discharge of the Amazon, and ∼1 m during low discharge (Kosuth et al., 2009). While the magnitude of the seasonal and tidal signals may be similar, the semidiurnal tides, because of their higher frequency, represent the majority of the barotropic exchange in the Xingu Ria. The maximum upstream discharge measured in the Xingu Ria was $\sim 1.3 \times 10^8$ m^3 per flood tide (August 2011). To estimate a tidal excursion of Amazon water into the Xingu, this discharge is applied to the most downstream location in the Xingu Ria where a single channel exists, and the channel cross-sectional area is $\sim 3 \times 10^4$ m^2, resulting in an upstream tidal excursion of ∼4 km per flood tide. The tidal excursion is estimated here because the channel is representative of the Xingu–Amazon confluence area, and flow is expected to be unidirectional throughout the cross section. This is unlike flow at the measured ADCP cross section where both up- and downstream flow occurs simultaneously (Figure 2.4A). This upstream extent of barotropic flow roughly matches satellite observations of the position of surface plumes of Amazon-derived sediment in the Xingu Ria, as well as bed sediment with a high smectite content consistent with an Amazon source (Figure 2.10B). While an individual flood tide may not be sufficient to move sediment into the more central parts of the Xingu Ria, the combined effect of settling and scour lag may act to pump sediment farther upstream with each flooding tide. Settling lag refers to time during which sediment continues to be carried upstream (while settling) by a waning flow that is no longer able to keep particles in suspension, an effect compounded by the difference between critical velocities for transport and erosion (scour lag) (van Straaten and Kuenen, 1958).

In addition to the combined effects of settling and scour lag, tidal pumping of sediment into the Xingu Ria is likely to be enhanced by deformation of the tidal wave as it propagates up the Amazon River and its lower tributaries. Tidal asymmetry increases with distance from the river mouth, resulting in periods of rising water with significantly shorter duration

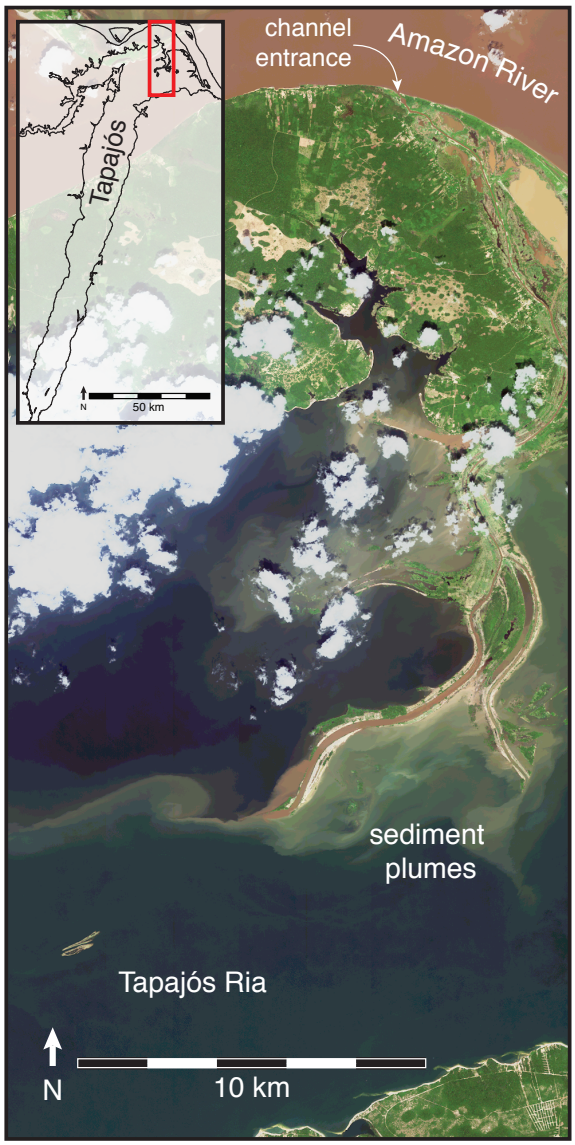

Figure 2.12: Satellite image of the birdsfoot delta that has built upstream into the Tapajós Ría near the Tapajós-Amazon confluence. Image collected on 20 September 2013 by DigitalGlobe WV02 and accessed via Digital Globe ImageFinder. The location of the image is marked by a red box in the inset in the upper left of the figure. Sediment-laden water from the Amazon River can be seen forming sediment plumes in the comparatively clear water of the Tapajós Ría, at the mouths of various distributary channels.

than falling water (Kosuth et al., 2009; Freitas et al., 2017). In the vicinity of the Amazon–Xingu confluence, the duration of falling water is typically twice that of rising water (Figure 2.13). During low flow of the Amazon and Xingu Rivers, discharge of the Xingu River ($\sim$1250 m^3 s^{-1}) is dwarfed by the tidal exchange ($\pm 10,000$ m^3 s^{-1}), and therefore plays a minor role in the observed asymmetry. In order to rapidly fill the Xingu Ria during the steep rising limb of the tide, velocities associated with flood tides must be faster on average than those associated with ebb tides, a phenomenon documented in many other tidal environments (see Friedrichs, 2011, for review).

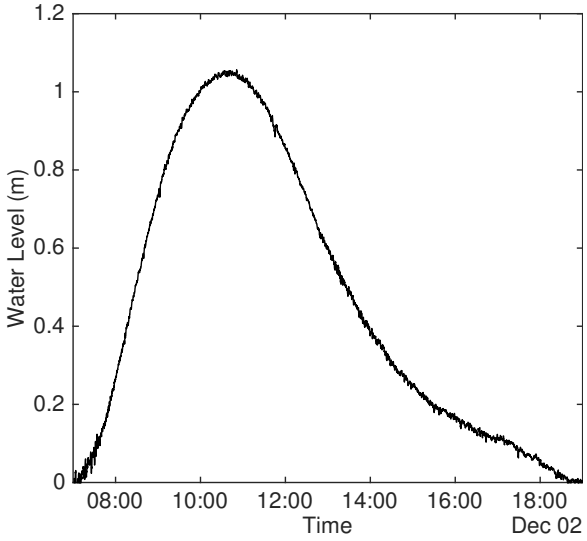

Figure 2.13: Plot of water level over one tidal cycle as measured on 2 December 2012 at the town of Almeirim, near the Amazon–Xingu confluence (see 2.1). Duration of the ebb tide is over twice that of the flood tide due to deformation of the tidal wave as it propagates up the Amazon River.

Higher velocities during flood tides can enhance upstream-directed sediment transport of both sediment reaching the bed and remaining in suspension. If the current-induced bed stress exceeds the critical stress for sediment resuspension, the elevated upstream-directed velocities will promote greater transport of bed sediment during flood tides due to the non-linear relationship between transport and bed stress (e.g., Bagnold, 1966). With the onset of the flood tide, water and sediment from the Amazon mainstem moves into the ria.

Upon entering the comparatively quiescent ria, particles kept in suspension in the energetic Amazon mainstem begin to settle. The greater upstream-directed flood velocities allow the larger of these particles to be transported a farther distance upstream before settling to the bed relative to upstream transport by symmetric tidal currents. Both processes promote upstream transport of Amazon-derived sediment into the Xingu Ria.

Baroclinic Flows

In addition to barotropic flows driven by surface gradients, density-driven (baroclinic) underflows appear to transport Amazon water and sediment into the Xingu Ria. During falling stage of the Amazon River, water temperatures in the mainstem are cooler than in the Xingu Ria (Figure 2.5A, Table 2.2). This appears to drive a tongue of cooler Amazon water upstream beneath a layer of warmer Xingu water near the surface (Figure 2.5A). Although the temperature differential is small (0.2°C), the density difference is equivalent to ∼60 mg L^{-1}. In addition to the temperature-induced excess density, the Amazon water at depth is more sediment laden (70–80 mg L^{-1}) than the Xingu water above it (<10 mg L^{-1}), resulting in an underflow with a combined excess density >100 mg L^{-1}. This type of underflow was observed in the Xingu only during August 2011, which coincides with falling stage in the Amazon mainstem and low flow of the Xingu River. During the other three cruises, water in the Amazon was warmer or nearly the same temperature as the tributaries (Table 2.2), producing a surface plume or no plume instead of an underflow (Figure 2.5B). The Amazon River was also cooler than the Tapajós Ria during August of 2011, but a similar phenomenon was not observed in the Tapajós. An underflow at the confluence of the Amazon and Tapajós may be more difficult to observe given the less-confined nature of the confluence relative to the Amazon–Xingu confluence. The larger discharge of the Tapajós compared to the Xingu during low-flow conditions (Table 2.1) might also inhibit any intrusion of Amazon water at depth, in much the same way that estuarine processes are commonly pushed seaward of river mouths during periods of elevated river discharge (e.g., Gibbs, 1970; Wright and Coleman, 1974; Nowacki et al., 2015).

Other Mechanisms

Circulation within the ria basins also plays an important role in sediment advection. The net downstream flux of water and sediment associated with input from the Tapajós and Xingu Rivers serves both to build proximal deposits (bayhead deltas), and distribute sediment more distally within the rias. In the Tapajós Ria, sediment fines away from the bayhead delta into the central part of the ria basin. Clay particles (finer than 2 μm), which comprise >75% of most samples, are carried beyond the bayhead deltas and into the ria basins by the weak currents, as measured at the ADCP transects. In order to reconcile the water clarity in these clearwater rias, and the substantial accumulation of very fine sediment on the beds of both rias, fine particles likely form aggregates or flocs, thereby hastening their settling to the bed. In the central part of each basin basin (cores TP-4 through TP-111, XIN-50 through XIN-201), particles finer than 1 μm comprise ∼50% of the sediment by mass. The amount of time required for these <1-μm particles to settle individually through a 10-m water column (representative depth of the rias) is ∼3.5 months, compared to the ∼1-month residence time of water in either the Tapajós or Xingu Ria. The possibility of flocculated sediment in freshwater is well documented (e.g. Walling and Moorehead, 1989; Droppo and Ongley, 1994). In the case of the Tapajós and Xingu Rias, flocculation may be encouraged by high phytoplankton production in clearwater environments, where Schmidt (1982) reports higher productivity than in areas of whitewater or blackwater (e.g., Amazon River, Rio Negro, respectively). In estuaries, such organic materials have been shown to play as large a role in flocculation as the salt-related electrochemical processes most commonly associated with sediment flocculation (Eisma, 1986).

In the Tapajós Ria, a persistent upstream flow is observed in the western margin of the ADCP transect (Figure 2.3). This upstream flow occurs throughout the tidal cycle during periods of both low and high discharge from the Tapajós River, with residual current velocities of ∼10–15 cm s^{-1}. Persistent upstream flow along the western margin of the northern Tapajós basin is likely a result of wind-driven circulation associated with northeasterly trade winds that occur throughout the year (Figure 2.14). The long axis of the Tapajós Ria downstream of the ADCP transect is roughly aligned with this dominant wind direction, creating

sufficient fetch to develop a current aligned with the wind. Upon encountering the western margin of the basin, this current is deflected toward the south, producing the upstream current observed at the ADCP transect.

The sediment plumes exiting the bird-foot delta (Figure 2.12) appear to be advected toward the southwest, consistent with such a wind-driven current. This upstream surface flow is likely balanced by a downstream return flow, which is added to the residual downstream discharge of the Tapajós River (see Csanady, 1973). The proximity of this persistent upstream flow to the terminus of the upstream-prograding bird-foot delta provides an additional mechanism for continued transport of Amazon-derived sediment into the Tapajós Ria. The upstream residual flow observed in the Xingu Ria during low-discharge conditions (Figure 2.4A) may similarly move Amazon-derived sediment farther into the Xingu Ria. However, the seasonal dependence of this upstream flow, and its presence during only the flood and early ebb phases of the tide likely results in a less-effective transport pathway in the Xingu Ria compared to the Tapajós Ria.

2.5.3 Sediment-Accumulation Budgets

Using the sediment-accumulation rates determined from ^{210}Pb geochronology, it is possible to estimate the amount of sediment trapped in the Tapajós and Xingu Rias (Figure 2.15). The bed-sediment budget for each ria is constructed by dividing the basin into zones represented by core locations. The boundaries between adjacent zones are defined by the perpendicular bisector of a line between neighboring cores. The sediment-accumulation rate determined from each core is applied to the entire zone. While this oversimplifies sediment accumulation within the basins, it provides a first-order approximation of the amount of sediment being trapped in each basin. Calculations using the areas and accumulation rates of each zone indicate that the Tapajós Ria traps ∼22 Mt of sediment annually (Figure 2.15). This value is ∼4 times the annual Tapajós River sediment discharge of 4.25–5.43 Mt estimated at Jatobá (upstream of the Tapajós Ria) reported in Filizola and Guyot (2009). Similarly, annual sediment accumulation in the Xingu Ria is ∼12 Mt y^{-1}, roughly 2.5 times the 4.46–5.80 Mt y^{-1} sediment discharge reported for the Xingu River at Altamira, upstream of the Xingu

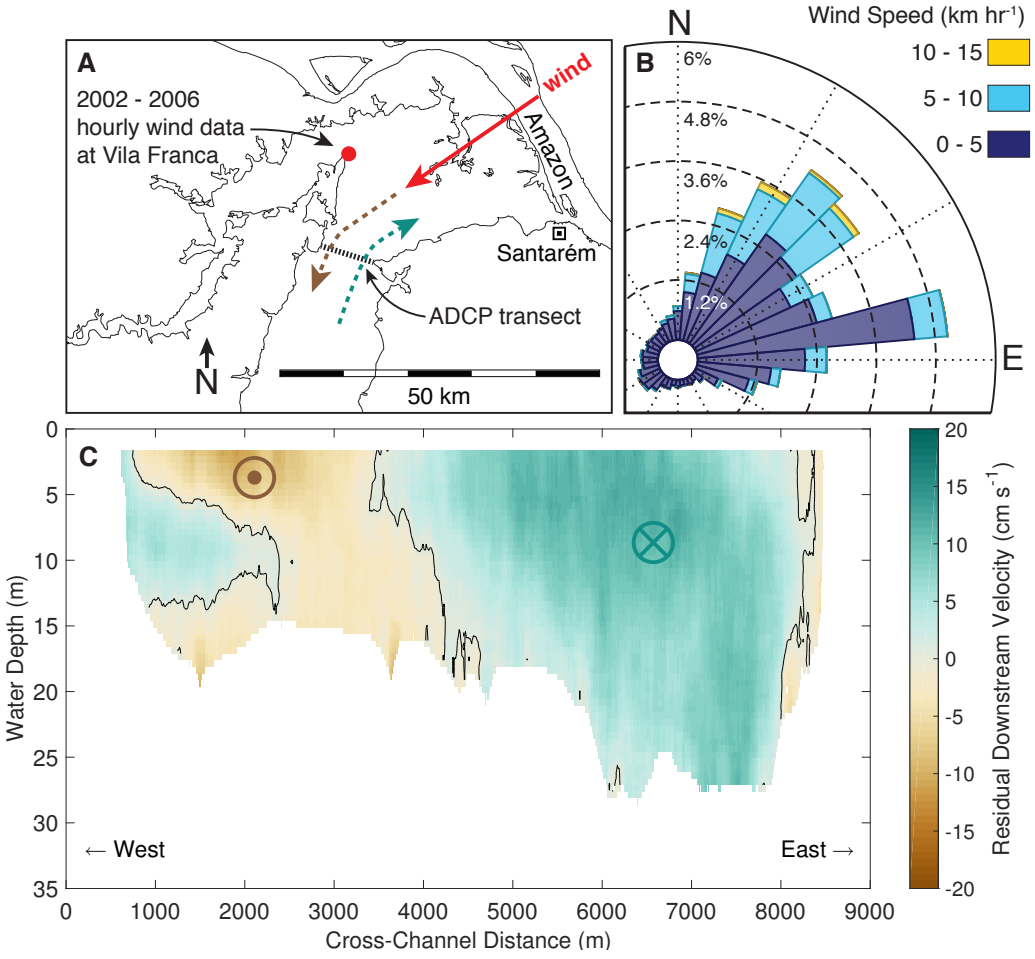

Figure 2.14: Wind-driven circulation in the Tapajós Ría is associated with persistent north-easterly winds. (A) Map of the northern 50 km of the Tapajós Ría showing the location of the ADCP transect (hashed black line) and the metrological station from which the data in panel B are derived (red dot). The red arrow indicates the dominant wind direction, and the brown dashed arrow suggests the direction of wind-driven upstream flow. The green dashed arrow represents the residual downstream flow in the eastern basin. Brown and blue colors correspond to colors of the ⊙ and ⊗ flow-direction indicators in panel c. (B) Wind rose of 35,031 hourly wind velocity measurements from 2002 - 2006 from The Large Scale Biosphere-Atmosphere Experiment in Amazonia (Fitzjarrald et al., 2009). (C) Plot of residual ADCP velocity from a 12.4-h tidal cycle collected on 31 October 2012, showing upstream flow in the western part of the Tapajós basin, and downstream flow in the deeper eastern part of the ría. The zero-velocity contour is shown in black.

Ria Filizola and Guyot (2009).

The sediment-accumulation rates used to calculate these budgets are similar to long-term sediment-accumulation rates determined for the duration of the Holocene (Irion et al., 2010). Geochronology (^{14}C) from two cores (20–40 m long) in the Tapajos Ria suggests sediment-accumulation rates have increased from ∼0.2–0.3 cm y^{-1} to ∼0.5–0.6 cm y^{-1} over the last ∼10,000 years (Irion et al., 2010). These rates are approximately half the mean sediment-accumulation rate of ∼0.9 cm y^{-1} determined from the nine cores collected in the Tapajós Ria (Figure 2.15A). This discrepancy between the century-scale rates determined from ^{210}Pb geochronology and the Holocene rates determined via ^{14}C could be the result of accelerated modern sediment accumulation, spatial variability in accumulation, or consolidation of older sediment. Given that the water depth of a considerable portion of the both rias is <10 m, modern rates of sediment accumulation suggest much of the remaining accommodation space in the rias may be infilled over the next millennium.

Depositional environments along the Amazon tidal river have been proposed as important sinks for sediment between the lowermost gauging station at Óbidos and the Atlantic Ocean. By differencing the sediment discharge at Óbidos (Meade et al., 1985) and measurements of sediment accumulation and fluxes on the adjacent continental shelf, Nittrouer et al. (1995b) estimate that up to one third of the sediment fluxed past Óbidos may be trapped along this reach. A comparison of our estimate of combined annual sediment accumulation in the Tapajós and Xingu Rias (∼34 Mt) and the estimated <12 Mt of sediment carried by the Tapajós and Xingu Rivers (Filizola and Guyot, 2009), suggests a total of ∼20 Mt of Amazon-derived sediment may accumulate in these two rias annually. This accounts for ∼5% of the ∼400 Mt of 'missing' Amazon sediment (see Nittrouer et al., 1995). The Tapajós and Xingu Rias represent ∼5% of the floodplain area of the Amazon tidal River below Óbidos, suggesting these environments do not have disproportionately large effect on trapping of sediment along the Amazon tidal river, and that processes acting in the intertidal floodplain (Mertes et al., 1996; Nowacki et al., 2017; Fricke et al., 2017a, *in revision*) play an important role in sediment trapping along the tidal reach.

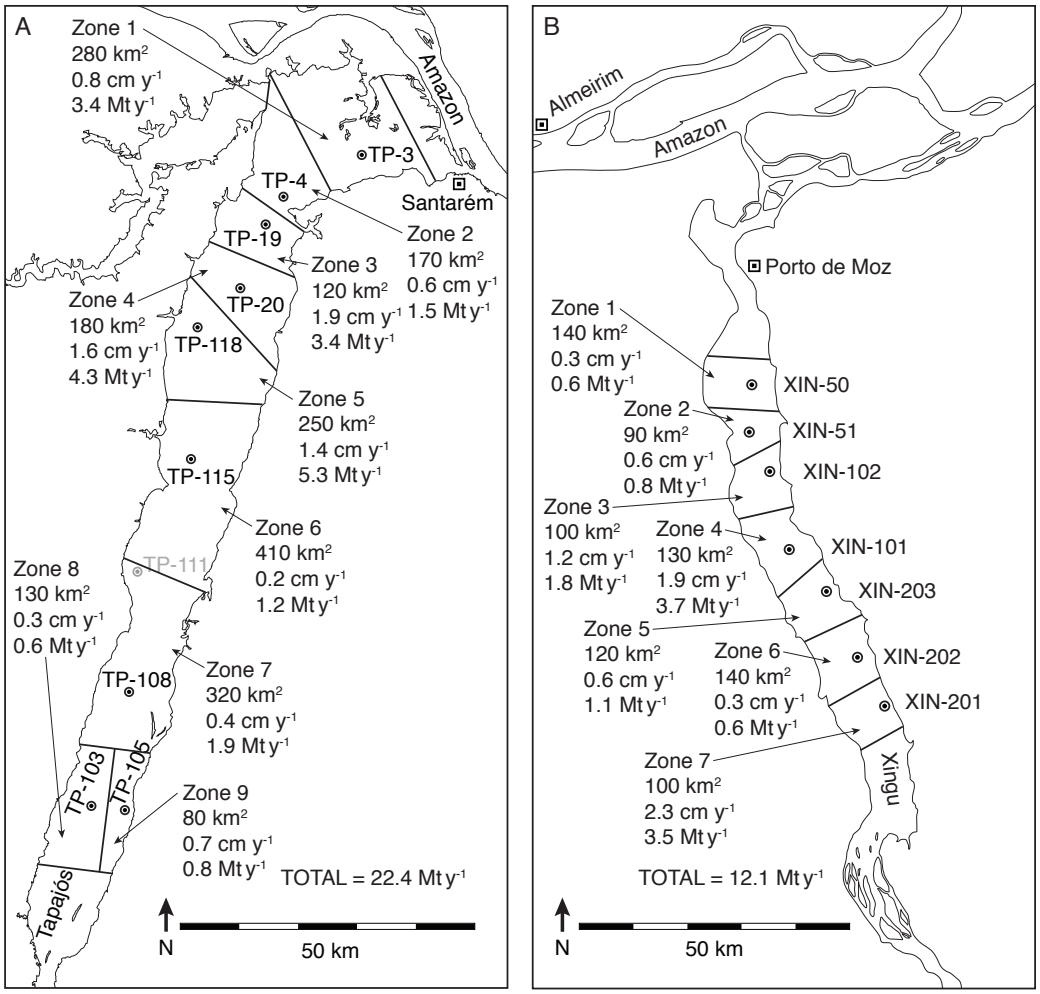

Figure 2.15: Sediment budgets for the Tapajós and Xingu Rías based on ^{210}Pb geochronology. (A) Map of the Tapajós Ría showing the nine zones used to develop the sediment budget. Core TP-111 is shown in light gray and was not used in determining the sediment budget. (B) Map of the Xingu Ría showing the seven zones used to develop the sediment budget. Below each zone number is listed the area of the zone, the sediment-accumulation rate calculated from the core in that zone, and the mass of sediment trapped in each zone annually assuming a uniform sediment-accumulation rate across each zone.

2.5.4 Estuary-like *Character of the Tapajós and Xingu Rías*

The Tapajós and Xingu Rias share many morphologic and hydrodynamic characteristics with estuaries. The plan-view form of the rias is very similar to coastal-plain (drowned-river-valley) estuaries (e.g. Chesapeake Bay, Gironde estuary), and the term ria (or ría) can be used interchangeably to describe such estuaries. All tend to be elongate basins incised during low stands in sea level, and flooded by subsequent sea-level rise. While many high-load rivers (e.g. Amazon, Orinoco, Mississippi) have already filled their incised valleys, rivers with low sediment-loads are still in the process of infilling. If the Amazon River had a lesser sediment discharge, and its incised valley remained unfilled, the Tapajós and Xingu might be more akin to the Rappahannock or York River Estuaries, which enter Chesapeake Bay, the former incised valley of the Susquehanna River (see Hobbs, 2004, for review).

Sediment trapping within coastal-plain estuaries is often dominated by processes that act to keep river-derived sediment in the estuary (e.g., near-bed landward flow creating an estuarine turbidity maximum), but bottom currents can also move offshore sediment into estuaries (e.g., Mead, 1969; Nowacki et al., 2015). The Tapajós and Xingu Rias experience a similar convergent flux of sediment from tributary and downstream sources. Unlike coastal-plain estuaries, however, the Tapajós and Xingu Rias do not debouch into ocean, and therefore do not experience mixing with saline waters, which is generally considered an important criterion for status as an estuary (see Elliott and McLusky, 2002, for review). From a physical perspective, the role of salinity in estuaries is as a driver of baroclinic circulation due to the density difference between fresh and saline waters. In the Tapajós and Xingu Rias, differences in suspended-sediment concentration and temperature provide the density contrast needed to drive baroclinic flows under certain conditions. In estuaries, salt also affects sediment transport and deposition by encouraging flocculation, thereby increasing the settling velocity of particles. In the Tapajós and Xingu Rias, organic material and long residence time may act to encourage flocculation in the absence of salt.

The Tapajós and Xingu, like most estuaries, experience tidal fluctuations that drive barotropic flows within the basins, and exchange across the downstream boundary. Although there is typically some deformation of the tide in estuaries due to a decrease in water

depth and interaction with the bed and with river discharge (see Dalrymple et al., 2011, for review), the deformation of the tide at the mouth of the Tapajós and Xingu Rias is extreme, with the duration of rising water being half that of falling water (see Figure 2.13; Kosuth et al., 2009). Such tidal asymmetry results in flood velocities that are greater than ebb velocities, making landward (upstream) transport in the confluences of the Tapajós and Xingu Rias more efficient than in estuaries with a similar tidal range but less pronounced tidal asymmetry. Such strong tidal asymmetry is likely characteristic of tidal depositional environments (including rias) along most if not all large tidal rivers.

2.5.5 Incised-Confluence Infilling from a Geologic Perspective

The lower reaches of nearly all rivers are subject to incision during falling base level, and subsequent infilling through aggradation and progradation following a rise in base level. In river systems with steep slopes, these processes may be limited to a short reach in the lowermost river, while in large, low-gradient, systems like the Amazon, such fluctuations in base level can propagate thousands of kilometers up the river network. In any river system where the reach that is impacted by base-level fluctuations includes a tributary confluence, then the rate of infilling of the mainstem river and the tributary will be a function primarily of the sediment load of each. The Tapajós and Xingu Rias are rare examples of deeply incised, low-load tributaries to a high-load mainstem, a configuration that may occur primarily in very large drainage basins where significant differences in source area and precipitation are more likely to occur. The Amazon watershed, which is the largest of any river, includes tributaries with high-load Andean source areas (e.g., Madeira), and clearwater tributaries like the Tapajós and Xingu Rivers that drain low-relief, low-yield environments. Because of these factors, the Tapajós and Xingu are two of the few major river confluences that are still in the process of infilling to an equilibrium cross-section following sea-level rise that began in the earliest Holocene. Most other incised tributaries (e.g., Strickand and Fly Rivers, Papua New Guinea; Swanson et al., 2008), have been infilled along with the mainstem.

Although such under-filled confluences may be rare in the present, incised-valley fills are common in the geologic record and of great sequence-stratigraphic interest (e.g. Zaitlin et al.,

1994; Blum et al., 2013). Summarizing incised-valley fills based on the segments first defined by Zaitlin et al. (1994), Nordfjord et al. (2006) describe the three process-based segments as: "(1) a landward zone, dominated by riverine sedimentation (e.g., bayhead deltas or straight tidal and fluvial channels), (2) a seaward zone, dominated by wave and/or tidal processes (e.g., an estuary mouth complex), and (3) an intermediate zone of mixed energy, effectively a sediment sink experiencing competing marine and non-marine influences." The Tapajós and Xingu Rias provide an opportunity to examine, as opposed to infer, the processes acting to fill incised valleys along a gradient in fluvial and marine influence similar to that summarized by Nordfjord et al. (2006). The Tapajós Ria would fall under "landward zone", where riverine processes (e.g., seasonal floods, tributary discharge) tend to dominate, producing the observed bayhead delta and distal fining of sediment down the length of the ria. The Xingu Ria might fall under the "seaward zone", given the importance of tides (e.g., reversing flows). On a smaller scale, each ria is a microcosm of the larger system, as both rias, over their length, experience a gradient in tidal and fluvial influence.

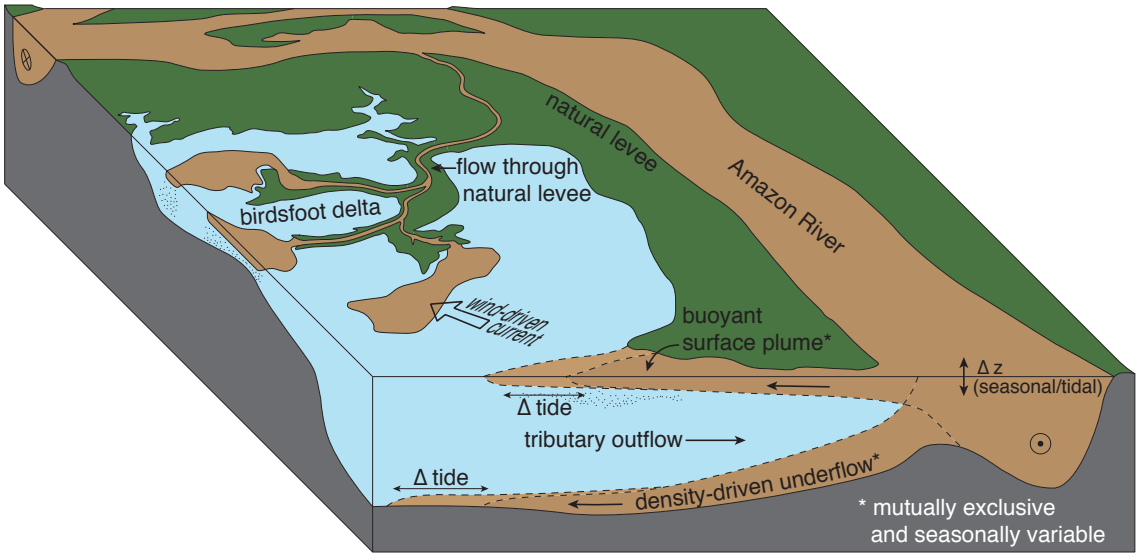

Figure 2.16: Cartoon representation of the possible sediment-transport processes that deliver Amazon-derived sediment to the confluence regions of the ría basins.

Studies of modern systems, such as the one presented here, provide understanding that is

needed to correctly interpret the sedimentary record. For example, both tributaries receive mainstem sediment through various means of upstream transport (Figure 2.16). In the more fluvial-dominated Tapajós Ria, seasonally driven barotropic flows and wind-driven circulation move Amazon sediment upstream into the tributary incised valley. In the Xingu Ria, upstream transport results from fully reversing flows driven by tides, as well as sediment- and temperature-driven baroclinic underflows. These sediment-transport mechanisms, the timescales on which they operate, and the spatial scales over which they move sediment, ultimately define the character of the stratigraphy preserved in the geologic record.

2.6 Conclusions

The distribution of sediment within the Tapajós and Xingu Rias, the mechanisms that deliver that sediment, and the timescales over which those mechanisms operate provide insights into the processes acting to fill incised valleys over geologic timescales. These findings also help to constrain the effect of these major tributary confluences on the fate of sediment carried both by the Amazon River and the tributaries themselves. Unlike most tributary confluences, which are one-way conduits for sediment and water, the rias of the Tapajós and Xingu import sediment from the mainstem of the Amazon River, in addition to trapping sediment carried downstream from the tributary drainages. Based on the above discussion, the following conclusions are reached:

(1) Tributary-derived sediment is accumulating over the majority of the Tapajós and Xingu Rías. There is a contribution of Amazon-derived sediment in the lower 30-40 km of each ría as evidenced by a coarsening of bed sediment, and a decrease in the kaolinite signature of the clay fraction.

(2) In addition to sediment supplied by the tributaries, the Tapajós and Xingu Rias receive sediment from the Amazon mainstem via barotropic and baroclinic processes. In the Tapajós Ria, barotropic processes are strongly influenced by the large seasonal flood of the Amazon River; and in the Xingu Ria, barotropic flows are driven by comparatively stronger tidal forcing. The Xingu Ria also experiences baroclinic exchange in which cooler, sediment-laden Amazon water intrudes beneath warmer, clear Xingu water. Additional local phenomena, including wind-driven circulation, may serve to distribute sediment within the

ria basins.

(3) The Tapajós Ría traps ∼22 Mt of sediment annually. Total sediment accumulation in the Xingu Ría is ∼12 Mt y^{-1}. Both of these values exceed the sediment discharge of the respective tributary. The differences between the published sediment discharge of each tributary and these budgets based on ^{210}Pb sediment-accumulation rates suggest that a combined total of ∼20 Mt of Amazon-derived sediment may be accumulating the two ría basins each year.

Chapter 3

MORPHOLOGY AND DYNAMICS OF THE INTERTIDAL FLOODPLAIN ALONG THE AMAZON TIDAL RIVER

3.1 Introduction

Rivers build floodplains by depositing sediment on the floors of the valleys through which they flow. Vertical accretion of floodplains is largely accomplished by overbank flow during floods (Wolman and Leopold, 1957). The timing, duration, and extent of overbank deposition during floods is impacted by the form of the floodplain and in particular the morphology of the river banks. For example, in the lowland reaches of many large rivers, the river channel is flanked by natural levees. These levees form as alluvial ridges along river banks, built from sediment deposited during repeated floods of the river. They form a topographic high that both confines the river channel, and impacts the transport of sediment and water into the floodplain behind the levee (Wolman and Leopold, 1957; Mertes et al., 1996; Brierley et al., 1997; Smith et al., 2009). The maximum height of natural levees is dictated by the water elevation during floods (Smith et al., 2009). In most rivers, a flood wave will attenuate downstream due to backwater effects, the increasing cross-sectional area of the river channel, and the decreasing fraction of the total flow contributed by the flood. Levee height should therefore decrease downstream as well.

For rivers that debouch into the ocean, water level near the river mouth is a function of both forcing from the upstream hydrograph and downstream tides. If the river gradient is steep, tides will propagate only a short distance up the river, if at all. However, if the channel gradient is low, as it is for many of the world's largest rivers (e.g., Amazon, Mekong, Fly), and the tidal range at the river mouth is large, tides may propagate hundreds of kilometers up the river. This reach of the river, where water level is impacted by tidal oscillations but salinity is absent, is known as the tidal river.

Environments downstream of the head of tides may remove sediment from (e.g., accu-

mulation in floodplains) or contribute sediment to (e.g., discharge from tributaries) the tidal river. Many studies have explored sedimentation in depositional environments at the seaward end of fluvial systems: deltas and estuaries. However, tidal rivers have received comparatively little attention (see Hoitink and Jay, 2016, for review). In the lower, non-tidal reaches of many large rivers, the form of river banks, especially natural levees, is a first-order control on river–floodplain connectivity (e.g., Fisk, 1947; Coleman, 1969). The character of levees and banks is likely as important in tidal-river settings, but their morphology and function in mixed fluvial–tidal environments has yet to be described.

This paper is focused on the river–floodplain interface along the fluvial–tidal continuum in the Amazon tidal river (Figure 3.1A). The Amazon River is the largest river in the world based on discharge of water and sediment, with an estimated 6300 km^3 of water and 1200 Mt of sediment estimated to flux past the lowermost gauging station at Óbidos each year (Milliman and Farnsworth, 2011). This gauging station is ∼800 km upstream of the Amazon River mouth, and relatively little is known about the transformation of these measured fluxes below Óbidos. The floodplain of the Amazon tidal river has been suggested as a possible sink for a significant fraction of the sediment that passes Óbidos, as much as one-third of which remains unaccounted for in Amazon sediment budgets (Nittrouer et al., 1995b; Dunne et al., 1998).

Preliminary observations along the Amazon tidal river suggest that the river banks change form over its length (Figure 3.1B,C). Levees, which play an important role in river–floodplain exchange along non-tidal rivers, seem to be prominent in the upper tidal river and absent from the lower reach. Rather than leveed banks, the floodplain of the lower tidal river appears infilled with sediment and dissected by dendritic channels. Understanding the spatial evolution of bank morphology (including levees) along tidal rivers is an important first step in understanding the exchange of water and sediment between tidal rivers and their intertidal floodplains. The objectives of this work are to: describe the morphologic evolution of the river-floodplain interface along the Amazon tidal river; identify the hydrodynamic and sediment dynamic forcing that creates the observed morphology; and develop a generalized conceptual model of river–floodplain exchange along the fluvial–tidal continuum characteristic of tidal-river environments.

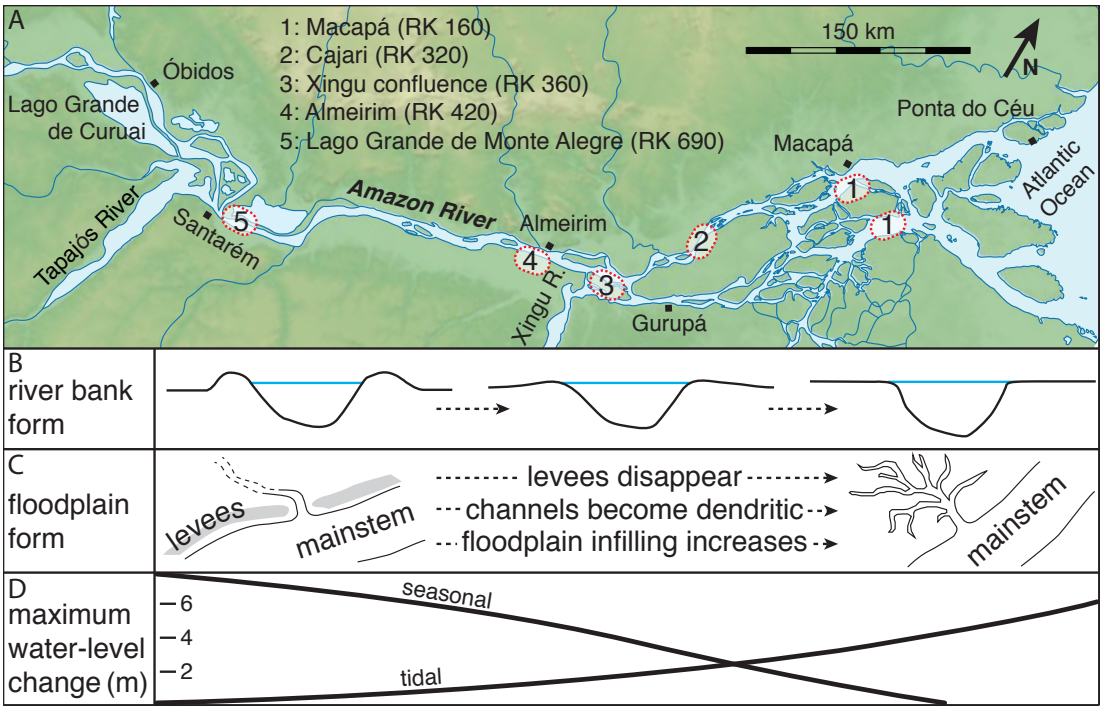

Figure 3.1: Map of the Amazon tidal river between Óbidos and the Atlantic Ocean. The five numbered regions (1–5) outlined in red dashed lines mark the river-bank study areas described herein. Three panels below the base map summarize preliminary observations of the morphology of (B) river banks, (C) floodplains, and (D) the approximate maximum water-level change associated with the seasonal flood and tidal oscillations. Lines in panel D are simplified from Kosuth et al. (2009).

3.2 Background

3.2.1 Site Selection

The lower Amazon River is an ideal location to study natural river-floodplain exchange. Of the world's largest rivers, the Amazon River arguably remains in the most natural condition. In particular, the banks of the Amazon tidal river exhibit very minimal human manipulation, largely limited to small wharfs in villages and cities. Unlike the lower reaches of almost all other large rivers (e.g., Mississippi, Huáng Hé, Yangtze, Mekong, Ganges–Brahmaputra), flood control systems are absent on the lower Amazon River. While these other rivers may have once exhibited trends in the morphology and dynamics associated with their natural banks and levees, those natural trends have been masked by human manipulation through the construction and hardening of levees, closing of crevasses, and creation of other flood-control structures.

Many other tidal rivers with intact natural levees and floodplains are considerably smaller than the Amazon. Variation in natural levees is controlled by more than just the flood levels of a river (Brierley et al., 1997). For example, levees have been shown to form preferentially on outside bends of rivers (Fisk, 1947), or on alternating banks (Iseya and Ikeda, 1989). The ∼800-km Amazon tidal river ensures that the length scale of levee evolution associated with the changing balance between fluvial and tidal influence is considerably longer than the length scale of intrinsic levee variability. In short tidal rivers, for example, it may be difficult to deconvolve the longitudinal trend in levee character from intrinsic levee variability because the overlapping length scale for each type of forcing.

The length of a tidal river is controlled by a number of factors, including the gradient of the river, depth of the river, and tidal range at the river mouth. It should be noted that tidal changes in water level along the river are due to the propagation of the tidal wave, not simply a barotropic effect. This allows tidal oscillations to propagate up rivers to an elevation significantly above that of high tide at the river mouth (see Hoitink and Jay, 2016, for review of tidal-river physics). The exceptional length of the Amazon tidal river is the result of its very low gradient (8–12 meter drop between Óbidos and the river mouth, Kosuth et al., 2009), considerable depth (locally >60 m; Vital and Stattegger, 2000c), and

macro-tidal conditions at the river mouth. The mean tidal range at Ponta do Céu, near the mouth of the Amazon River (Figure 3.1) is 3.3 m, and up to 4.5 meters during spring tides. Tides are semidiurnal, with nearly equivalent elevations between successive high and low tides. The semidiurnal tidal change in water-surface elevation at the river mouth is of a similar magnitude to the seasonal change in water level at Óbidos of ∼6 m (Kosuth et al., 2009). The similar magnitude of seasonal (fluvial) and tidal forcing allows the signature of each regime to be well resolved near the up- and downstream limits of the tidal river, and the the combination of regimes to be distinguished where they overlap in the central tidal river.

3.2.2 Physical Setting – bookends of the Amazon tidal river

It is helpful to put the morphology and dynamics of the tidal river into context by examining the environments that are immediately up- and downstream of this reach. The upstream limit of the Amazon tidal river is also the downstream limit of the purely fluvial Amazon River. Dunne et al. (1998) provide a comprehensive review of the sediment dynamics in the river and floodplain along this reach. Near Manaus, ∼600 km upstream of Óbidos, the heights of natural levees are up to 10 m above the low-water level of the river (Latrubesse and Franzinelli, 2002), which roughly matches the average seasonal water level change at Manaus of 9.8 m (Archer, 2005). Along this leveed reach of the river, levees tend to confine the river to its channel, and limit lateral migration, so that floodplain sedimentation is accomplished primarily through overbank deposition. This is in contrast to non-leveed reaches hundreds of kilometers farther upstream, where floodplain sedimentation is dominated by lateral channel migration, and deposition in myriad floodplain channels, creating scroll-bar topography (Mertes et al., 1996).

Due to the energetic marine environment at the mouth of the Amazon River, sediment discharged by the river has formed a large subaqueous deltaic clinoform, rather than a subaerial delta (see Nittrouer et al., 1995b, for review). Along the coast to the north and south of the Amazon river mouth, sedimentation in the upper littoral zone takes the form of mangrove-colonized tidal flats (e.g., Pará coast: Asp et al., 2016, Amapá coast: Allison

et al., 1995a). These environments are characterized as elevated, vegetated, muddy platforms that are built to the approximate level of high tide. The platforms are dissected by dendritic tidal channels that serve as conduits through which water and sediment are transported. The highest parts of these tidal platforms are only inundated during extreme spring tides (Asp et al., 2016). The morphology of these coastal environments bears a first-order resemblance to the floodplain of the lower Amazon tidal river (Figure 3.1B).

3.3 Methods

3.3.1 Bank Surveys

A survey of the banks along the Amazon tidal river was conducted over the period 20–26 March 2014. This time period is ∼3 months before peak stage of the Amazon River, but discharge in 2014 was especially high, and the water level at the time of the survey was equivalent to mean peak water level of the Amazon River as measured at Óbidos (Figure 3.2). A total of 17 banks were surveyed at five regions spanning ∼690 km of the Amazon tidal river (Figures 3.1, 3.3). River banks were surveyed perpendicular to the water's edge, and were intended to capture the highest part of the bank (e.g., levee crest). Surveyed transects were 30–250 m in length, with a mean length of ∼80 m. Surveys were performed by stretching a long measuring tape along the transect and using a topographic abney level to read a survey staff at ∼1–4-m intervals along the transect.

Where levees were present (between Lago Grande de Monte Alegre and the Amazon–Xingu confluence) bank surveys did not capture the full width of the levee, many of which are 100s–1000s of meters wide. Because levee deposits typically thin away from the river channel (Fisk, 1947; Allen, 1964; Adams et al., 2004), the levee crest is located proximal to the river's edge. In the Amazon system, there is strong zonation of plant and tree species according to inundation duration (i.e., elevation relative to flood level), with the largest trees occupying levee crests (see Junk et al., 1989, for review). Surveys were conducted near the channel, through the most mature vegetation in order to capture the most elevated part of the bank.

In order to relate all of the measured transects, a novel datum was defined. Because of

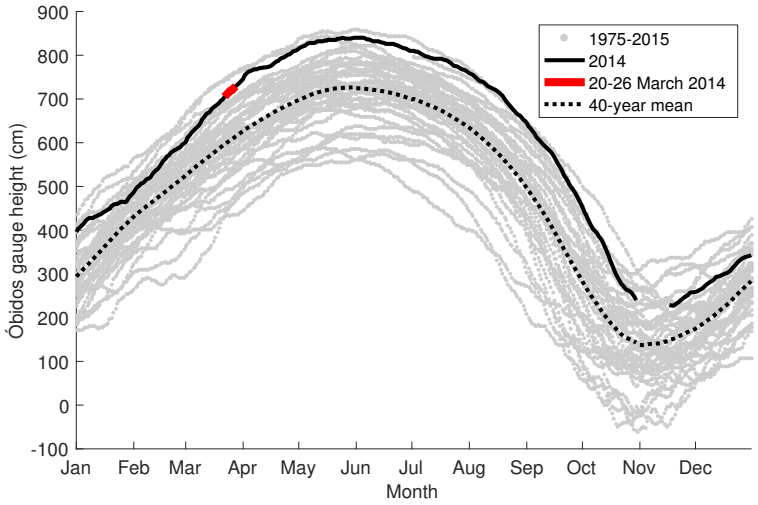

Figure 3.2: Gauge height of the Amazon River at Óbidos between 1975 and 2015 (gray dots), overlain by the 40-year mean annual discharge (dashed black line). The hydrograph for 2014 is shown as a solid black line, and the duration of the study described here is highlighted in red. Data are from the hydrographic station at Óbidos maintained by the Brazilian Agência Nacional de Águas and accessed via the SO HYBAM portal [http://www.ore-hybam.org/].

the important role that the elevation of high water (seasonal or tidal) plays in both river–levee systems and in tidal-flat environments, a high-water or flood datum was defined. A water-level logger with a 10-minute sampling interval was deployed in the vicinity of each of the survey areas for a ∼13-hr period in order to capture a complete tidal cycle. The water's edge was surveyed at each transect, and the time recorded. All of the surveys from each area were subsequently adjusted so that bank elevations were relative to the local high-tide level.

Over the 7 days when levee surveys were undertaken, the water level at Óbidos monotonically rose ∼30 cm. In addition, there was a range in high-tide elevations at Macapá of ∼60 cm. In order to compensate for changes in up- and downstream water level over the survey period, data from each of the survey areas was offset to be equivalent to conditions on 25 March 2014. Because the effect of water-level changes at either end of the tidal river are not felt uniformly over its length, it is necessary to determine the fractional response to up- and downstream perturbations at each of the survey areas.

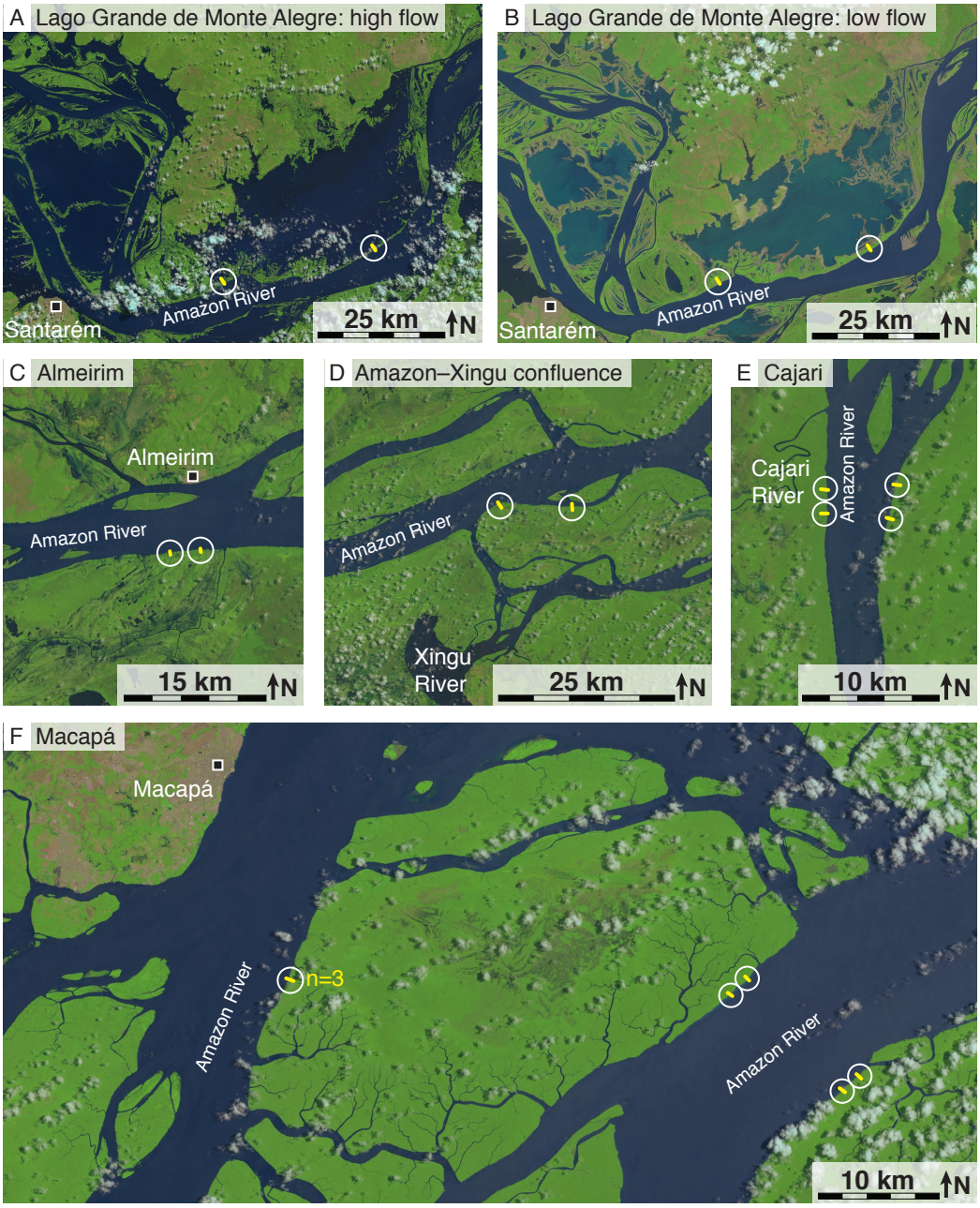

Figure 3.3: Satellite images (Landsat 8) of the river bank survey areas, showing the location of 17 surveyed transects (yellow lines inside white circles). See Figure 3.1 for the location of each survey area along Amazon tidal river. The Lago Grande de Monte Alegre survey area is shown during (A) high discharge and (B) low discharge conditions to illustrate the large seasonal change in water-surface elevation. Only one image is shown for the (C) Almeirim, (D) Amazon–Xingu confluence, (E) Cajari, and (F) Macapá survey areas. A single image of these areas (C–F) is sufficient because seasonal/tidal changes in inundation of these areas are not visible at this scale. Images were collected on the following dates: (A) 5/6/3012, (B) 24/12/2016, (C–E) 23/8/2015, (F) 14/9/2015.

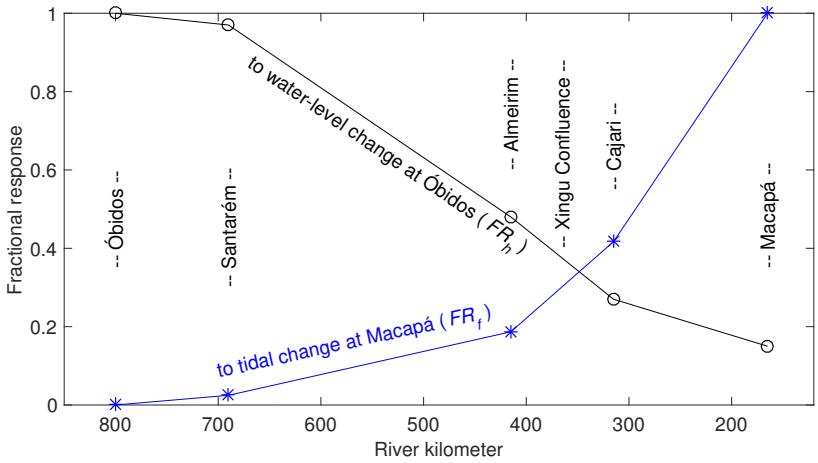

Figure 3.4: Fractional response to water-level changes at Óbidos (black ∘) and tidal oscillations at Macapá (blue ∗) along the length of the Amazon tidal river. The fractional response to a water-level change at Óbidos (FR_h) decreases downstream, while the fractional response to changes in tidal elevation at Macapá (FR_f) decreases upstream. The position of each survey area is marked by its name. Data are derived from Kosuth et al. (2009), see Section 3.3.1 for details.

The fractional response to water-level changes at Óbidos (Figure 3.4) was derived by comparing the water-surface elevation along the tidal river at mean stage (150,000 m^3 s^{-1}) to that during low river stage (100,000 m^3 s^{-1}) (Kosuth et al., 2009). The curve representing the fractional response to tidal change in Macapá was derived from synoptic tidal measurements at 5 locations along the tidal river on 29 June 1999 (Kosuth et al., 2009, Fig. 5). Tidal propagation in the Amazon River is strongly impacted by discharge (Kosuth et al., 2009), so care must be taken when applying estimates of tidal propagation across different flow conditions. In this case, the difference in gauge height at Óbidos between 29 June 1999 and 25 March 2014 (this datum) was 45 cm, or ∼7% of the seasonal change, so the fractional response to tidal forcing along the river determined from the June 1999 data can be reasonably applied to the survey period.

For each survey area, corrected survey elevations (CE) were determined as:

$$CE = WL_s + \Delta H_t + (\Delta H_h \times FR_h) + (\Delta H_f \times FR_f) \tag{3.1}$$

where WL_s is the water level as measured at the time of survey, ΔH_t is the difference in

water level between the time of survey and the high tide measured by the water-level logger at the site (Figure 3.5B), ΔH_h is the difference in Óbidos gauge height during the survey and the gauge height on 25 March 2014 (Figure 3.5A), FR_h is the site-specific fractional response to water-level changes at Óbidos (Figure 3.4), ΔH_f is the difference in water level between the high tide as measured at Macapá on the day of the survey and the elevation of the high tide at Macapá on 25 March 2014 (Figure 3.5C), and FR_f is the site-specific fractional response to water-level changes at Macapá (Figure 3.4). The result is a uniform datum that corresponds to the local high-water level on 25 March 2014, which coincided with neap tidal conditions at the Amazon River mouth. Typical high-tide elevations during spring tidal conditions near Macapá are ∼0.5 m greater than the high tide on 25 March 2014. This datum is not horizontal, but rather tracks the sloped water surface of the river. Because the water level on 25 March 2014 was equal to the mean annual peak water level (Figure 3.2), this datum can be considered a 'flood level' along the Amazon tidal river.

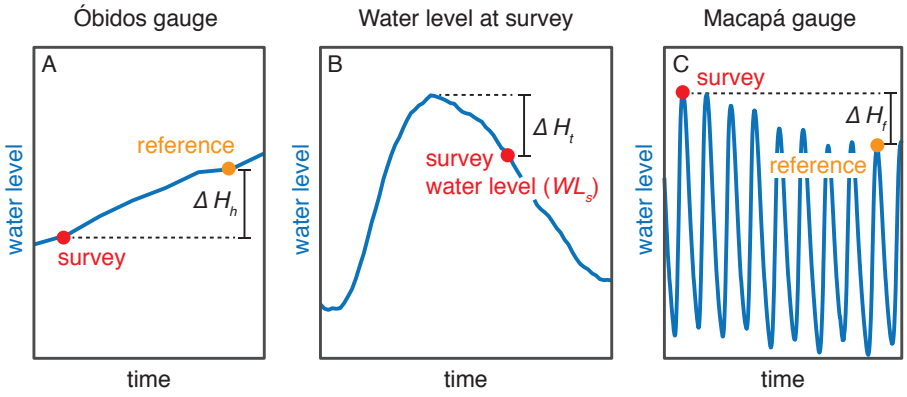

Figure 3.5: Simplified plots of the three types of water-level records used to define the water-level datum used in this study (see Equation 3.1). (A) Water-level record at Óbidos, where ΔH_h is the difference in water level between the time of survey and the 25 March 2014 reference level. (B) Water-level record from near a survey site capturing the high tide, where ΔH_t is the difference between the water level at the time of survey (WL_s) and the nearest high tide. (C) Water-level record from near Macapá, where ΔH_f is the difference in water level between the high tide associated with the survey (shown in panel B) and the reference high tide on 25 March 2014.

3.3.2 Sediment sampling and coring

Sampling and coring were undertaken to examine changes in the sediment character of the banks along the Amazon tidal river, as well as patterns of sediment accumulation over decades to centuries. Grab samples were collected along the measured transects by hand or using a Van Veen grab from a small boat. Short cores, augers(<60 cm length) were pushed directly into the sediment by hand. Cores were cut into 2-cm intervals and bagged for grain-size and radiochemical analyses. Grain-size distributions of the mud fraction (<64 μm) from each sample were determined using Micromeritics Sedigraph 5100, 5120, and 5125 particle sizers in the laboratory.

Sediment-accumulation rates were determined using ^{210}Pb, a naturally occurring radioisotope. ^{210}Pb geochronology can be used to constrain sediment accumulation over the past century, owing to its 22.3-year half-life (Nittrouer et al., 1979). The activity of ^{210}Pb is determined via alpha spectrometry by measuring the activity of its granddaughter, ^{210}Po, relative to a calibrated spike of ^{209}Po. The sediment-accumulation rate (S) is calculated using:

$$S = \frac{\lambda z}{\ln(\frac{A_0}{A_z})} \tag{3.2}$$

where λ is the decay constant for ^{210}Pb, A_0 and A_z are excess ^{210}Pb activities at two points within the region of log-linear decay, and z is the difference in core depth between A_0 and A_z. The activity of ^{210}Pb above that supported by in-situ decay of ^{226}Ra in the sediment column is defined as the excess ^{210}Pb activity. Total ^{210}Pb activity below the region of log-linear decay in the deepest cores is $\sim$1.1 dpm g^{-1}, so this value is used as the supported level for all cores.

3.4 Results

3.4.1 Bank Surveys

Between 2 and 7 bank surveys were conducted at each of the five survey areas and representative profiles are shown in Figure 3.1. River banks were most elevated above the water-level datum in the Lago Grande de Monte Alegre and Macapá survey areas, and were lowest in the Almeirim and Xingu confluence areas (Figures 3.6, 3.7). In general, the elevation of the

river banks in the Lago Grande de Monte Alegre, Cajari, and Macapá areas was found to be roughly coincident with the water-level datum, while the banks near Almeirim and the Xingu confluence were lower (Figure 3.7). The water depth behind the levee in Lago Grande de Monte Alegre is estimated to have been 3–5 m at the time of the bank surveys. This depth range is based on ship-based depth measurements from June 2013, which have been corrected for the difference in Óbidos water level between 14 June 2013 and 25 March 2014 (−80 cm).

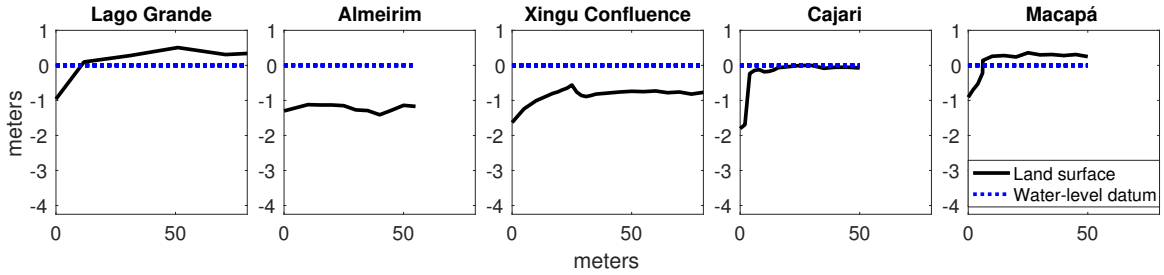

Figure 3.6: Representative river-bank profiles from each of the five survey areas (Figure 3.1). Profiles were measured perpendicular to the Amazon tidal river, which is toward the left in each panel. The measured land surface is marked with a solid black line, and the water-level datum is marked with a blue dashed line (see Section 3.3.1 for datum details). Panels are arranged from upstream at left, to downstream at right.

3.4.2 Sediment Character

Surface-sediment samples were collected at 3–4 locations along each of the surveyed transects. No consistent trend was observed between grain size and distance from the river channel. In general, sediment fines in the downstream direction along the Amazon tidal river (Figure 3.8). Detailed analysis of the mud fraction (<64 μm) of samples shows that mean mud grain size decreases from ∼18 μm (medium silt) at Lago Grande de Monte Alegre to ∼7 μm (very fine silt) at Macapá. Samples collected near the Amazon–Xingu confluence are on average slightly coarser than samples from the Almeirim area. The mud fractions of samples from the two most downstream survey areas (Cajari and Macapá) show little variability, as seen in the short whiskers in Figure 3.8. Areas farther upstream show a greater range of grain

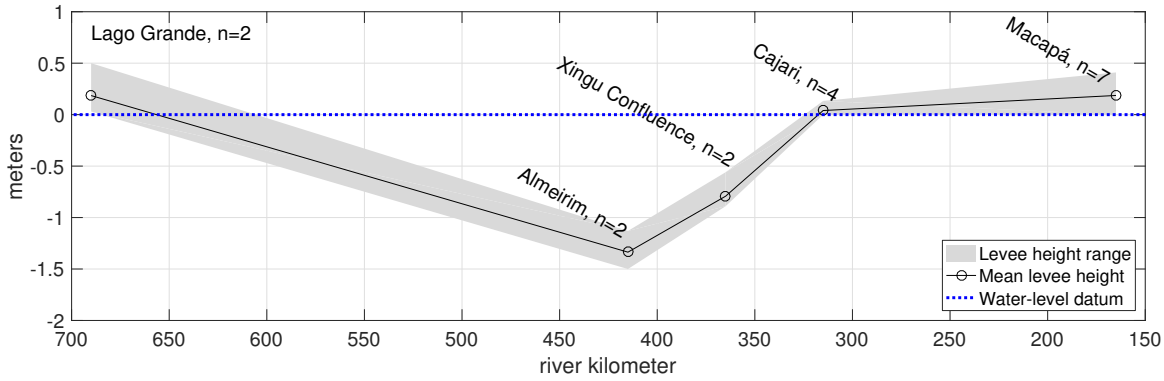

Figure 3.7: Elevation of the banks of the Amazon tidal river between Lago Grande de Monte Alegre and Macapá relative to the water-level datum. The range in measured peak bank elevations from each survey area are shown with gray shading, and the mean peak elevation of the banks from each area are marked with open circles and solid black lines. The water-level datum is marked with a blue dashed line (see Section 3.3.1 for datum details). The river banks along the up- and downstream ends of the tidal river are built roughly to the elevation of the water-level datum, while banks in the central Amazon tidal river are below the datum.

sizes within the mud fraction.

The amount of sand in sediment samples from the river banks broadly tracks with patterns in the mud fraction, and there is a decrease in sand in the downstream direction (Figure 3.8). Samples from the Macapá area show the greatest range in sand content (2–60%), while the range in samples from Cajari and Almeirim, in the central tidal river, is considerably less.

3.4.3 Sediment Accumulation

Sediment-accumulation rates were determined via ^{210}Pb geochronology for a total of 6 cores collected in the survey areas (Figure 3.3) along the Amazon tidal river (Figure 3.9). Of the six cores, four (Figure 3.9A–D) exhibited a log-linear down-core decrease in excess ^{210}Pb activity associated with steady-state sediment delivery (see Nittrouer et al., 1979). Two cores were analyzed from Lago Grande de Monte Alegre. The sediment-accumulation rate determined from a core collected in the central part of the lake (0.8 cm y^{-1}) was less than

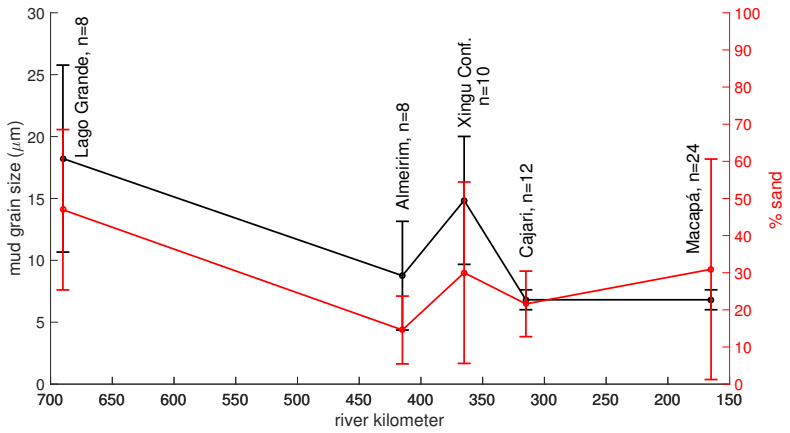

Figure 3.8: Surface-sediment grain size along the banks of the Amazon tidal river between Lago Grande de Monte Alegre and Macapá. Black dots (connected by lines) represent the mean grain size of the mud fraction (<64 μm) of all samples from each site, and the whiskers denote the range in mean grain size of mud at each site. Red dots (connected by lines) represent the mean percent sand (>64 μm) of all samples from each site, and the whiskers denote the range in percent sand at each site. In general sediment fines downstream along the Amazon tidal river.

the rate of 2.2 cm y^{-1} determined from a core collected near the terminus of a crevasse that cuts the levee separating Lago Grande de Monte Alegre from the Amazon mainstem (Figure 3.9A, B).

Analysis of two cores from the Almerim area indicate a sediment-accumulation rate of 1.6 cm y^{-1} at a location ~50 m landward of the levee (Figure 3.9C), decreasing to 1.1 cm y^{-1} at a location ~700 m farther landward (Figure 3.9D). Cores from farther downstream near the Amazon–Xingu confluence and Macapá areas do not yield ^{210}Pb profiles with a region of log-linear decay, and therefore cannot be used to determine a sediment-accumulation rate (Figure 3.9E, F). While the ^{210}Pb profiles are chaotic, excess activity is present in the upper ~30 cm of sediment.

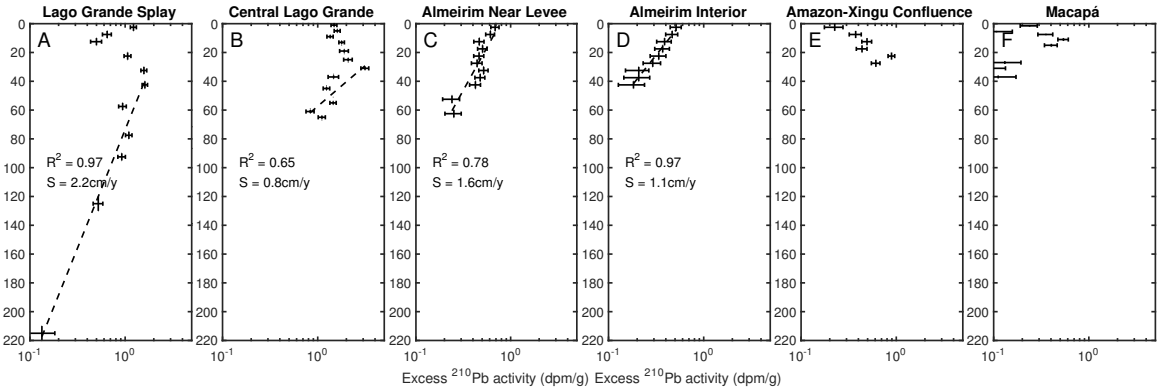

Figure 3.9: Profiles of excess ^{210}Pb from cores collected along the banks of the Amazon tidal river between Lago Grande de Monte Alegre and Macapá. Within Lago Grande de Monte Alegre, a core collected near the terminus of a levee-cutting channel (A) records a sediment-accumulation rate of 2.2 cm y^{-1}, while a core from the central part of the lake (B) records less rapid sediment accumulation (0.8 cm y^{-1}). (C) A core from the Almeirim floodplain collected ∼50 m landward of the levee records a sediment accumulation rate of 1.6 cm y^{-1}. (D) A core collected from the interior of the Almeirim floodplain (∼750 m from the levee) records a sediment-accumulation rate of 1.1 cm y^{-1}. ^{210}Pb profiles from near the Amazon–Xingu confluence (E) and Macapá (F) do not exhibit a decreasing log-linear profile, but excess ^{210}Pb is present in the upper ∼30 cm of sediment. Log-linear regressions and correlation coefficients (R^2) are determined for the profile regions of log-linear decay, and the sediment-accumulation rates (S) are shown.

3.5 Discussion

3.5.1 What controls bank elevation?

The Amazon tidal river is a transitional environment between the non-tidal Amazon River upstream of Óbidos and the Atlantic Ocean. Although the dominant forcing functions in the system (tidal oscillations and seasonal floods) vary continuously along the tidal reach, for the sake of this discussion, the tidal river is subdivided into three reaches: the upper, lower, and central tidal river. The upper and lower reaches of the tidal river are best understood relative to established morphodynamics of the endmember environments that bound them (fluvial and coastal marine). The morphology and processes of the central tidal river are distinct and perhaps unique to tidal-river environments. This central reach, which has yet to be described in the context of the tidal-river system, has been proposed as a location for substantial sediment trapping downstream of Óbidos (Mertes et al., 1996; Mertes and Dunne, 2008), but the processes responsible for such trapping remain poorly constrained.

The upper tidal river

In non-tidal river systems without levees, the elevations of river banks are generally set by bar deposition associated with lateral migration of the river channel (Wolman and Leopold, 1957; Lewin et al., 2016). Where levees are present, their height is limited by the water-surface elevation during floods (Wolman and Leopold, 1957; Smith et al., 2009). The initial elevation of the floodplain behind the levees is likely set by bar deposition associated with lateral migration of the river channel over long timescales, and subsequently modified by overbank deposition (Wolman and Leopold, 1957; Lewin et al., 2016).

The morphology of the upper Amazon tidal river is very similar to the morphology of the non-tidal reach immediately upstream. In particular, Lago Grande de Curuai, located across the river from Óbidos (Figure 3.1A), has a very similar planform morphology and depth range to Lago Grande de Monte Alegre (see Bonnet et al., 2008; Alcântara et al., 2010; Rudorff and Melack, 2014). Although parts of Lago Grande de Curuai are downstream of Óbidos, tidal forcing must be negligible, as tides are not discussed in papers examining the hydrology of the lake (Bonnet et al., 2008; Rudorff and Melack, 2014).

The effect of tides on river–floodplain exchange in the upper tidal river may be limited by the presence of levees. The tidal signal in the upper tidal river is relatively small (<20 cm), and the natural levees are significantly elevated (∼7 m) above the level of low flows of the Amazon River. It is during low discharge of the Amazon River that the tidal range is greatest in the upper tidal river (Kosuth et al., 2009), but the natural levees along this reach largely preclude river–floodplain exchange during this period. River–floodplain connectivity increases as the water-level rises in the Amazon mainstem, but tidal range is diminished due to the greater river velocity and decreased tidal celerity (Kosuth et al., 2009).

During most of the year (or entire years) when levees are not overtopped, they effectively isolate the floodplain from the mainstem except in locations where channels (crevasses) cross-cut the levees and allow water and sediment to move into the floodplain. During high river discharge, the tidal range in the upper tidal river is <10 cm. Given an average slope for the river of ∼1.1 cm km^{-1} (Kosuth et al., 2009), and the large scale of inundated floodplains (>10 km), persistent non-tidal pressure gradients within the floodplain are of a similar magnitude to those caused by tides. These flows through crevasse channels have produced long, leveed channel paths, which Mertes et al. (1996) describe as “lake deltas". Such features are common in the large floodplain lakes of the upper tidal river and are especially visible during low-discharge conditions, when they appear as sinuous, leveed channels building into and across floodplain lakes (Figure 3.3B).

The lower tidal river

This reach of river below the Amazon–Xingu confluence is variously termed the “lowermost” Amazon River (Vital et al., 1998), the “inner Amazon estuary” (Archer, 2005), or the "estuary" (Sioli, 1984). However, the term estuary confuses the understanding of processes in this reach, as salinity is a typical criterion for designation as an estuary (Elliott and McLusky, 2002), and the entirety of the Amazon River (and part of the continental shelf) is fresh at all times (Gibbs, 1970; Geyer et al., 1996). These nomenclatural issues highlight the complex forcing within this reach associated with energetic tidal conditions, and enormous fluxes of water and sediment (10^{12} tons y^{-1} water, 10^{9} tons y^{-1} sediment; Milliman and Farnsworth,

2011).

Literature examining the lower tidal river focuses on the sedimentology and dynamics within the river channels (Sioli, 1984; Torres, 1997; Vital et al., 1998, 1999; Vital and Stattegger, 2000b,a,c), with less attention paid to the floodplains along this reach. Satellite observations reveal a distinct change in floodplain configuration below the Amazon–Xingu confluence, which has been described as the apex of the "mouth funnel" of the Amazon River (Sioli, 1984). Downstream of this point, the planforms of channels that connect the mainstem to the floodplain are dendritic. Floodplain channels with dendritic forms do not exist above the Amazon–Xingu confluence.

Dendritic tidal channels are nearly ubiquitous in mud-flat and salt-marsh environments around the world (e.g., van Straaten, 1961; Bridges and Leeder, 1976; Frey and Basan, 1985; Nittrouer et al., 2013). Such channels in high flats or marshes likely follow the forms of antecedent subtidal channels (Frey and Basan, 1985). These channels experience reversing flows, and serve as conduits for flooding and draining the flat/marsh into which they are incised. Depending on the elevation of the flat/marsh, overbank flow from the channel may occur daily (low flat/marsh), or only during peak tidal conditions (high flat/marsh) (Frey and Basan, 1985).

The morphologies of banks along the lower tidal river more closely resemble flats/marshes than fluvial floodplains. There are no discernible levees along the lower Amazon tidal river, and instead, there are well developed networks of dendritic tidal channels that serve to exchange water and sediment with the floodplain (including distal floodplain) on tidal timescales. The close agreement between the elevation of the land surface and the water-level datum for areas downstream of Cajari highlights the degree of floodplain infilling along this reach (Figures 3.6, 3.7). Any antecedent fluvial morphology (e.g., levee, bar) has been obscured by deposition of sediment that has formed a planar surface incised by dendritic tidal channels.

Like high flats/marshes, which represent the final stage in the transition from intertidal to terrestrial environments, the floodplain in the lower Amazon tidal river has largely filled the accommodation space available. Near Macapá, for example, the floodplain is elevated to the point that a combination of seasonally high water and high tide is necessary to inundate

it (Nowacki et al., 2017). Because the water-level datum defined in this paper represents neap tidal conditions, the banks surveyed near Macapá are up to 50 cm above the datum. Given the ∼60-cm difference between spring and neap high-tide elevations at Macapá, the measured floodplain would experience shallow inundation on spring tides during the high-discharge period. Bank elevation near Cajari is lower than near Macapá (Figures 3.6, 3.7), suggesting the tidal processes that so effectively fill the Macapá floodplain are less efficient farther upstream.

The central tidal river

While the up- and downstream endmembers of the tidal river closely resemble adjacent environments just beyond the bounds of the tidal river, the central tidal river lacks such analogs. This reach begins downstream of Lago Grande de Monte Alegre, and extends to the confluence of the Amazon and Xingu Rivers. The downstream boundary of this reach is defined by a change in floodplain morphology and in the dominant forcing from fluvial to tidal. Below the Amazon–Xingu confluence floodplain channels become dendritic, and water-level changes are more responsive to downstream tidal oscillations than to upstream seasonal changes in river stage (Figure 3.4). Levees are present along the central tidal river, but their relief above the floodplain behind them is considerably less than observed in the upper tidal river. Unlike levees upstream, which appear to be built to the elevation of flood stage, the levees measured near Almeirim and the Amazon–Xingu confluence were overtopped by 0.75–1.25 m of water during the survey period, which was representative of flood conditions (Figure 3.7).

Levees are the product of a marked reduction in flow velocity, and therefore transport capacity, between a river channel and its inundated floodplain. Mertes (1997) describes the complex means by which the floodplains of the non-tidal Amazon river fill with water during floods, including overbank flow, groundwater flow, hyprorheic flow, and direct precipitation. While spatially variable, this diversity of processes promotes an equilibrium between the water-surface elevation in the river and in the floodplain. Of the above mentioned sources of water, only overbank flow carries sediment that can contribute to levee building. Once

the levees are overtopped, there is a free shear boundary that develops between the fast-moving water in the river, and the slow-moving water on the floodplain (Adams et al., 2004). Turbulent eddies form at this shear boundary, and propagate into the floodplain (Rajaratnam and Ahmadi, 1979). As the turbulence of these eddies decreases into the floodplain, sediment falls from suspension, resulting in a diffusion of sediment away from the river channel. The length scale of this diffusive transport is relatively short, resulting in steep narrow levees (Adams et al., 2004).

While levees in the upper tidal river can be described as narrow and steep (Figure 3.3A, B), those in the central tidal river are neither. In environments where the water level in a river rises faster than in its floodplain, sediment transport into the floodplain may be advective rather than diffusive, producing wider, more gently sloping levees (e.g. Lower Saskatchewan River, Adams et al., 2004). In the central Amazon tidal river, semidiurnal tides produce water-level changes of 0.5–1 m, which in turn drive barotropic (advective) flows into and out of the floodplain. The advection-dominated levees described by Adams et al. (2004) likely experience a few advective overbank flows in a year (e.g. freshet, storm). In contrast, the levees of the central Amazon tidal river experience four across-levee advective flows each day during periods when the seasonal water level is sufficiently elevated to allow for inundation of the floodplain.

While across-levee tidal currents appear to suppress levee development relative to the upper tidal river, tidal action along this reach is not sufficient to produce the elevated, channelized floodplain of the lower tidal river. As the filled floodplain below Cajari shows, tidal exchange is an effective means of moving sediment from the mainstem of the river into the floodplain. Two factors likely reduce the efficiency of tide-driven sediment transport into floodplains in the central tidal river. First, compared to the lower tidal river, water level in the central river is more affected by upstream changes in river stage. As a consequence, during low and moderate stages of the Amazon River, water level in the central tidal river is too low, even during high tides, to inundate the floodplain, whereas the floodplain farther downstream experiences inundation. Second, the greater tidal range in the lower tidal river results in a greater tidal excursion and flux of water and sediment into the floodplain, leading to more rapid sediment accumulation there.

3.5.2 Implications for sediment trapping

Holocene infilling of the Amazon paleo-valley

During the last glacial maximum (LGM), the Amazon River carved a deep valley to the paleo-coastline, which is now the continental-shelf break at a depth of ∼120 m (Vital and Stattegger, 2000a; Irion et al., 2010). At the upstream limit of the Amazon tidal river near Óbidos, the floodplain has aggraded ∼70 m since the LGM, and near Macapá, Holocene aggradation approaches 100 m (Irion et al., 2010). In the broadest sense, the Amazon River has effectively filled its paleo-valley, especially compared to low-load tributaries like the Negro, Tapajós, and Xingu Rivers (Irion, 1984; Sioli, 1984; Irion et al., 2010; Fricke et al., 2017b, *in revision*).

On a finer scale, however, the degree of infilling along the tidal river is not uniform. In the lower tidal river, where Holocene incision was greatest, river sediment has effectively filled all available accommodation space by filling the floodplain to an elevation roughly co-incident with the level of combined seasonal and tidal high water. By comparison, in the upper tidal river, the elevation of the floodplain behind the natural levees is 3-5 m below the level of combined seasonal and tidal high water. The degree of infilling in the central tidal river falls between these two endmembers. Water depths in the distal parts of the floodplain near Almeirim and the Amazon–Xingu confluence were not measured as part of this study. However, the lack of large open bodies of water, and the presence of permanent vegetation on the floodplain, indicates the depth of inundation in the central tidal river is reduced compared to areas in the upper tidal river.

Because the depth, and consequently width, of incision during the LGM was greater toward the lower part of what is now the tidal river, a greater amount of sediment was needed to infill the larger excavated volume downstream. Based on this simple geometric relationship, more sediment has accumulated over the Holocene in the lower reaches of the Amazon tidal river than in the upper reaches. However, the dominant sediment sink throughout the Holocene may not match patterns of modern sedimentation in the floodplain of the Amazon tidal river.

Modern sediment accumulation in the floodplain of the Amazon tidal river

As discussed above, the elevation of the floodplain along the lower Amazon tidal river (downstream of the Amazon–Xingu confluence) suggests that there is little remaining accommodation space for sediment accumulation. The creation of new accommodation space within the floodplain along this reach is likely associated with three factors: sea-level rise; neotectonics; and sediment compaction. Of these three factors, the rate of sea-level rise is probably the best constrained, with estimates for the western tropical Atlantic of $\sim$3 mm y^{-1} (Church et al., 2013). Tectonics have played a role in the evolution of the Amazon River and basin over geologic timescales (see Mertes and Dunne, 2008, for review), but rates of vertical tectonic displacement in the lower Amazon basin remain as yet unresolved. In the absence of evidence to the contrary, we assume tectonic displacement to be negligible. In a paper examining the sinking of most large river deltas around the world, Syvitski et al. (2009) list the subaerial Amazon delta as "not at risk" due to sufficient aggradation, and minimal anthropogenic subsidence. Natural compaction is typically $\leq$3 mm y^{-1} (Syvitski et al., 2009), and therefore could be responsible for up to half of the accommodation space being created in the lower Amazon tidal river.

Although ^{210}Pb profiles from the lower tidal river (Macapá area) are not log linear, and therefore cannot be interpreted using the method described in Section 3.3.2, it is possible to estimate a rough century-scale rate of sediment accumulation from the measured profile. The ^{210}Pb profile from the lower tidal river (Figure 3.9F) shows excess ^{210}Pb in the upper $\sim$30 cm of the core. An additional 4 measurements were made below 30 cm and all yielded activities equal to the supported activity of ^{210}Pb in the cores ($\sim$1.1 dpm g^{-1}). Given the ^{210}Pb half life of 22.3 years, the passing of five half lives (111.5 years) would result in an activity of $\sim$3% of the initial value. This $\sim$3% value is within the systematic error limits of the ^{210}Pb method used here (see Nittrouer et al., 1979). As a result, we can assume that the time represented by the sediment bearing excess ^{210}Pb (above the supported activity) represents up to five half lives, or approximately a century. Given these assumptions, the $\sim$30 cm of sediment with ^{210}Pb activities in excess of the supported activity have been deposited within the last century, indicating a century-scale sediment accumulation rate of

$\sim$3 mm y^{-1}. This sediment-accumulation rate is of a similar magnitude to estimates of sea-level rise (Church et al., 2013) and natural compaction (Syvitski et al., 2009) in the Amazon delta region.

The upper Amazon tidal river and associated floodplain appears to function in much the same manner as non-tidal reaches upstream. While tides are present, their influence is greatest when the the seasonal water-level is too low for significant communication between river and floodplain. Given the minor role of tides, the mechanisms and rates of sediment deposition in the upper tidal river are likely similar to those in the upstream non-tidal reach (see Mertes, 1994; Moreira-Turcq et al., 2004; Rudorff and Melack, 2014; Lewin et al., 2016). The sediment-accumulation rate of 0.8 cm y^{-1} measured in central Lago Grande de Monte Alegre (Figure 3.9B) is consistent with the 0.42–1.34 cm y^{-1} of accumulation in Lago Grande de Curuai, a similar floodplain lake just upstream of the limit of tidal influence (Moreira-Turcq et al., 2004). A higher accumulation rate (2.2 cm y^{-1}) was determined from a core collected within Lago Grande de Monte Alegre at a location near the terminus of a crevasse through the levee separating the lake from the mainstem (Figure 3.9A).

Sedimentation in the central tidal river has been the subject of considerable discussion. Klammer (1984) and Mertes et al. (1996) observe that the Amazon River below Lago Grande de Monte Alegre is relatively straight and the adjacent floodplain is devoid of the type of floodplain lakes or scroll topography common to the lower reach of the non-tidal Amazon River. Klammer (1984) suggests such features have been filled with sediment, and Mertes et al. (1996) estimate that 300–400 Mt of sediment is deposited in this reach annually. Changes in river gradient associated with a number of structural arches, principally the Purús Arch ($\sim$750 km upstream of Óbidos), and the Gurupá arch near the city of Gurupá, are invoked by Mertes et al. (1996) to explain variation in deposition along the lower fluvial and upper tidal river. Mertes and Dunne (2008) provide a concise summary of their earlier observations and suggest based on floodplain morphology that most of the 300–400 Mt of deposition occurs in the reach of the Amazon River between Lago Grande de Monte Alegre and the Amazon–Xingu confluence. Rather than being related to structural arches, we suggest that the distinct morphology of this reach is due to the changing balance of fluvial and tidal influences relative upstream reaches.

A core collected ∼50 m landward of the levee in the Almeirim area records a sediment-accumulation rate of 1.6 cm y^{-1} (Figure 3.9C). An additional core was collected in the interior of the Almeirim floodplain at a distance of ∼750 m from the river bank, and records a sediment-accumulation rate of 1.1 cm y^{-1} (Figure 3.9D). Levees in the central tidal river are muted compared to levees upstream, i.e., levee height relative to the floodplain behind the levee is less than in the upper tidal river. The <35% reduction in sediment-accumulation rate between the two cores from the Almeirim area (Figure 3.9C, D) is consistent with the observed morphology that suggests long-term rates of sediment accumulation near the river bank and in the distal floodplain are relatively similar, compared to reaches with prominent levees. The sediment-accumulation rate in the central tidal river of 1.1–1.6 cm y^{-1} is 1.4–2 times the sediment-accumulation rate measured in the interior of the floodplain in upper tidal river (Figure 3.9). The greater sediment-accumulation rate in the central tidal river is consistent with the greater degree of infilling of the floodplain at present relative to the upper tidal river. Similarly, the rate of sediment accumulation in the central tidal river significantly exceeds the rate in the lower tidal river of ∼ 30 cm per century (∼3 mm y^{-1}).

The more "filled" (Klammer, 1984) nature of the floodplain along the central tidal river relative to upstream reaches is the product of increased tidal influence. In the upper tidal river (and fluvial reaches upstream) the movement of sediment between river and floodplain is dominated by inefficient diffusive transport, which leads to deposition near the river bank, producing steep narrow levees (Rajaratnam and Ahmadi, 1979; Adams et al., 2004). As tidal range increases downstream, levees do not reach the level of highest water, because four daily tidal currents flood and drain across the levee. The increased energy associated with these tidal currents (relative to diffusive eddies) suppresses sediment deposition at the levee crest, but increases sediment deposition farther into the floodplain. The result is more efficient trapping increased infilling of the floodplain, and a decrease in levee height relative to high water.

3.6 Conclusions

This work provides the first comprehensive assessment of tidal-river floodplain morphology and processes. Any tidal river is a transition zone between fluvial and marine environments,

and the relative impact of signals from the upstream river and downstream ocean are not felt uniformly along its length. The morphology of the river banks, and the manner in which river–floodplain exchange occurs, reflects these overlapping fluvial and marine regimes. Table 3.1 subdivides the tidal river into upper, central, and lower reaches, and summarizes the defining characteristics of each reach. Because the intensity of the tidal and fluvial

	Tidal-River Reaches		
	upper	*central*	*lower*
levee character	prominent	muted	none
floodplain inundation depth during flood (% of seasonal W.L. change)	∼75%	∼50%	<10%
river–floodplain sediment exchange effeciency	low	moderate	high
dominant mode of sediment transport	diffusive overbank	advective overbank	advective channelized
sediment-accumulation rate	moderate	high	low
qualitative description	significant accommodation space, but diffusive across-levee transport limits accumulation	tidal currents suppress levee development and allow substantial sediment transport into floodplain	efficient channelized transport driven by tidal currents has filled available accommodation space

Table 3.1: Summary of some of the key attributes of the upper, central, and lower reaches of the tidal river.

signals vary smoothly along the tidal river, the transitions between each reach is likely to be gradational. Moreover, the intensity of those same signals varies over daily, fortnightly, and seasonal timescales, so any boundary between reaches would be expected to translate up- or downstream accordingly. Nonetheless, discretizing the Amazon tidal river into three reaches provides a framework for identifying key features and processes that define each of the three reaches of a tidal river:

- **The upper tidal river:** The dominance of the the seasonal change in water level over comparatively small water-level changes induced by tides causes this reach to resemble the non-tidal river upstream. While tides do affect the velocity of the mainstem, and

flows between the mainstem and the floodplain, their effect is matched or eclipsed by the seasonal signal. The strength of the tidal signal is greatest when fluvial discharge is least. However, during periods of low discharge, the floodplain is isolated from the mainstem by tall natural levees, rendering tidal exchange ineffective. Sediment delivery occurs primarily during periods of moderate to high discharge when water and sediment are able to flow through crevasse channels that incise the levees or when levees are overtopped. Sediment accumulation is accentuated in the interior of the floodplain associated with crevasse channels, but most sediment is deposited near the levee due to inefficient diffusive overbank transport between mainstem and floodplain.

- **The central tidal river:** The magnitude of the seasonal and tidal signals are more evenly matched in the central tidal river. Changes in water level due to tides drive currents between the mainstem and the floodplain. These tidal currents more efficiently transport sediment into the floodplain than do the diffusive eddies of the upper tidal river. The result is a reduction in sediment deposition at the river's edge (i.e., minimal in levee building), and an increase in sediment delivery to the interior of the floodplain. The amount of time that the floodplain is isolated from the mainstem in the central tidal river is less than in the upper tidal river, due to lower natural levees and a more attenuated seasonal low-water level. More efficient advective sediment transport and a shorter period of low-water isolation, cause rates of sediment accumulation to be greater in the central tidal river than in the upper tidal river.

- **The lower tidal river:** Currents driven by tides are the dominant means of sediment transport between mainstem and floodplain in the lower tidal river, and the morphology of the floodplain reflects this. The floodplain is elevated approximately to the level of combined seasonal and tidal high water. Tidal channels incise this elevated floodplain and act as conduits to deliver water and sediment efficiently to the interior of the floodplain. Rates of sediment accumulation in the lower tidal river are less than in other reaches of the tidal river, and reflect a lack of accommodation space rather than a lack of available sediment or efficient transport.

This work shows that the morphology of the tidal-river floodplain responds to subtle changes in the balance between fluvial and marine forcing. Given this, current and future changes to the up- and downstream boundary conditions of the tidal river, including dam construction and sea-level rise, have the potential to alter significantly the form and behavior of tidal-river floodplain environments.

Chapter 4

ASYMMETRIC PROGRADATION OF A COASTAL MANGROVE FOREST CONTROLLED BY COMBINED FLUVIAL AND MARINE INFLUENCE, Cù Lao Dung, VIETNAM[1]

4.1 Introduction

Mangroves are the dominant form of intertidal vegetation in tropical environments. Their role in limiting shoreline erosion by protecting against storm surge and wave energy is well documented (Alongi, 2008; Granek and Ruttenberg, 2007). However, conservationists warn that mangroves are declining globally at a rate that may result in their demise within a century (Duke et al., 2007). Some of the most expansive mangrove environments are associated with large tropical rivers, where they thrive in extensive low-gradient intertidal zones that are nourished by sediment recently discharged from adjacent rivers.

The Mekong River Delta in southern Vietnam is fringed by coastal mangrove forests, although the extent of these forests is in decline due to coastal retreat and conversion to agricultural or aquacultural use (Thu and Populus, 2007). Parts of the Mekong River Delta experience subsidence rates up to 4 cm y^{-1} (Erban et al., 2014), which combined with eustatic sea-level rise of $\sim$1.7 mm y^{-1} (Holgate and Woodworth, 2004), accentuates marine hazards in the coastal zone (e.g., flooding, salt intrusion, shoreline retreat). Coastal mangrove forests in the Mekong Delta should help ameliorate these negative effects by increasing coastal resilience to attack by waves and storm surge, and also by encouraging sediment retention leading to aggradation and progradation of the coast.

The balance of factors promoting the growth of coastal mangroves is likely site-specific, and in the case of the Mekong Delta is related to the strong seasonal (monsoonal) nature of both river discharge and marine energetics (e.g., winds, waves, longshore currents). The

[1]This chapter was accepted to *Continental Shelf Research* as: Fricke, A.T., Nittrouer, C.A., Ogston, A.S., Vo-Luong, H.P., Asymmetric progradation of a coastal mangrove forest controlled by combined fluvial and marine influence, Cù Lao Dung, Vietnam, and is in revision.

aim of this research is to elucidate the connections between the progradation of a mangrove-colonized shoreline, the fluvial sediment source (Mekong River), and forcing from the marine environment. Specific objectives are to (1) identify sediment-transport pathways between river, proximal inner shelf, and mangrove forest, (2) characterize the hydro- and sediment dynamics that facilitate differential sediment accumulation across a fringing coastal mangrove forest, and (3) compare modern sediment deposition and shoreline progradation to century-scale stratigraphy and sediment accumulation.

4.2 Setting

The Mekong River is the 7th largest source of freshwater to the global ocean, and the 11th largest source of sediment (Milliman and Farnsworth, 2011). Shortly after entering Vietnam, the Mekong bifurcates into two primary distributary channels, with the western Sông Hậo channel carrying ∼40% of the flow (Nguyen et al., 2008). The Sông Hậo remains a single thread until splitting around the ∼35-km-long island of Cù Lao Dung and entering the East Sea (South China Sea) (Figure 4.1). The seaward margin of Cù Lao Dung (9.52°N, 106.27°E) is colonized by mangroves (*sp. Sonneratia, Aegiceras corniculatum, Avicennia*) (Nardin et al., 2016) and is prograding in an asymmetric manner. Rapid progradation occurs in the southwest part of the mangrove forest (∼60 m y^{-1}), while the northeast part of the mangrove forest has experienced periods of retreat (Nardin et al., 2016), resulting in negligible progradation over the ∼40-year satellite record (Figure 4.2). With the exception of a manmade levee at its landward margin, crab foraging and fishing activities, and three small irrigation channels, processes within the mangrove forest occur in in the absence of extensive human manipulation (e.g., clear-cutting, dredging).

High flow of the Mekong River is associated with the southwest monsoon season during Jul–Dec (Wolanski et al., 1998). While the southwest monsoon brings rain, marine conditions (e.g., waves, currents) are relatively quiescent except during typhoons, which are uncommon as far south as the Mekong Delta. The northeast monsoon (Jan–Jun) is comparatively dry, resulting in low discharge of the Mekong during this period. Winds are generally stronger during the northeast monsoon, resulting in energetic marine conditions in the the East Sea (South China Sea). It is also during this period that longshore transport and coastal currents

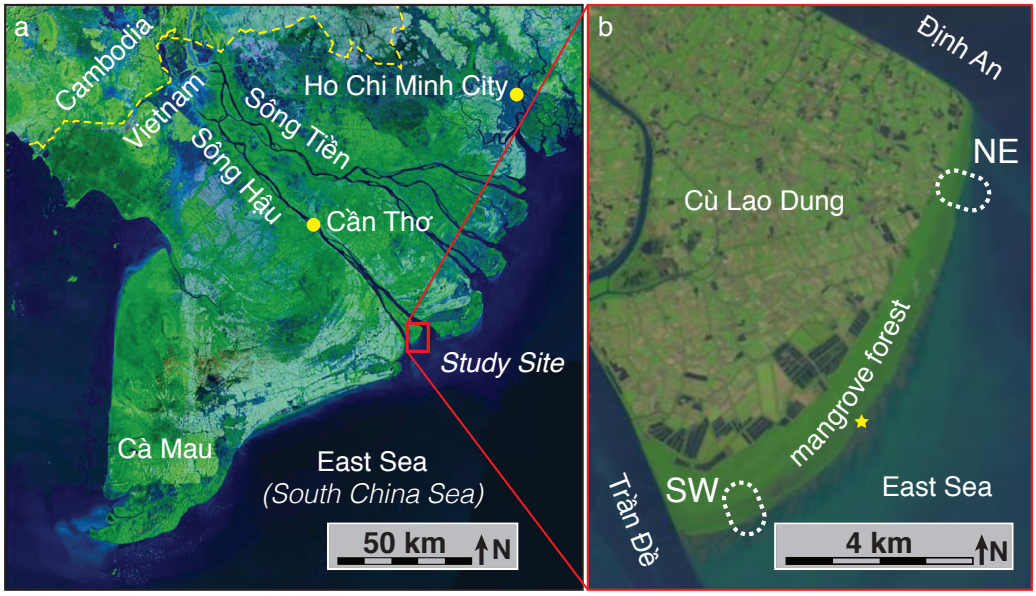

Figure 4.1: Location map of study area. Panel a shows the entire Mekong River delta including the southern Sông Hậo channels and the northern Sông Tiền channels. The enlargement at right (b) shows the seaward limit of the island of Cù Lao Dung with approximate locations of the SW and NE sites. A yellow star marks the approximate location of the study site described in Vo-Luong et al. (2017).

advect sediment and water toward the southwest along the coast (Ta et al., 2002; Hu et al., 2000). In essence, the year can be divided into a southwest monsoon season with elevated water and sediment discharge and subdued marine energetics, and a northeast monsoon season in which river discharge is low, but wave and current energy are high.

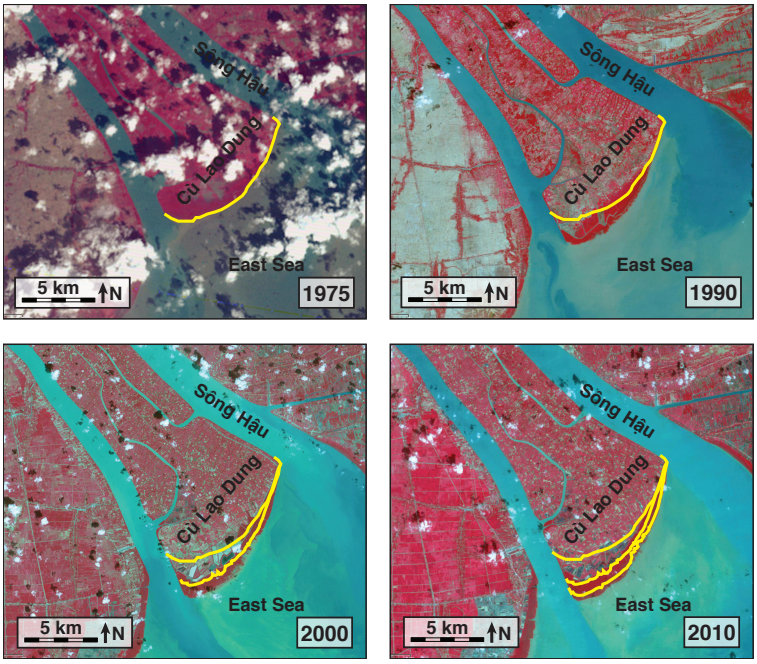

Figure 4.2: Four infrared Landsat images show seaward progradation of Cù Lao Dung between 1975 and 2010. The shoreline from each previous panel is marked on subsequent satellite images from 1990, 2000, and 2010. Maximum progradation between 1975 and 2010 is ∼2.8 km at the southernmost extent of the island.

4.3 Background

Mangrove environments have received substantial attention from the sedimentological community. The effects of mangrove roots and pneumatophores on sediment trapping and retention have been well documented (Wells and Coleman, 1981; Young and Harvey, 1996; Mazda et al., 1997; Krauss et al., 2003). Similarly, sediment accumulation rates and changes in bed elevation have been documented in a variety of mangrove environments around the

world (Lynch et al., 1989; Young and Harvey, 1996; Krauss et al., 2003). Mangrove environments are diverse and sediment dynamics within any given forest are influenced by myriad site-specific factors.

From a geological perspective, coastal mangrove forests can be grossly divided into those dominated by an allochthonous source of fluvial sediment (e.g., Gulf of Papua: Walsh and Nittrouer, 2004; Sunderbans: Rogers et al., 2013; Amazon: Allison et al., 1995b), or those that rely on autochthonous sediment (e.g., Caribbean: Parkinson et al., 1994; Pacific Islands: Ellison, 2008). The mangrove forest on Cù Lao Dung, which spans the coastline between the two mouths of the largest single distributary of the Mekong (Nguyen et al., 2008), is included amongst those systems dominated by fluvial sediment. Although early work on sedimentation in mangrove forests emphasized their role in *building* new land (Davis, 1940), more recent work suggests that mangroves *follow* sediment deposition and encourage sediment retention and enhance deposition once established (e.g., Zimmermann and Thom, 1982; Woodroffe, 1992). In general, mangroves are thought to colonize quiescent intertidal environments preferentially, where sediment is able to accumulate (Woodroffe, 2002; Alongi, 2008).

Many studies examine processes that affect sediment transport and deposition within mangrove forests (e.g., Wolanski and Ridd, 1986; Wolanski, 1995; Mazda et al., 1997, 2006), as well as the factors that influence the transport of sediment from fluvial source to mangrove forest (e.g., Schaeffer-Novelli et al., 1990; Allison and Kepple, 2001; Fromard et al., 2004; Baltzer et al., 2004; Walcker et al., 2015). Fewer studies compare mangrove environments that are experiencing retreat to those that are prograding seaward. Those that do, focus on broad trends and drivers rather than detailed processes (e.g., Alongi, 2002; Shearman et al., 2013). Focusing on broad trends is often necessary because of the difficulty in isolating the effect of any one process (e.g., reduction in sediment supply, sea-level rise) on multiple sites given differences between sites (e.g., grain size, marine forcing, vegetation species) that may overprint the process of interest.

Even with the proximity of the Cù Lao Dung mangrove forest to a major source of sediment, a portion of the shoreline has experienced limited growth through time (Figure 4.2). In contrast to comparisons between prograding and retreating mangrove forests separated

by hundreds of kilometers or even hemispheres, the gradient in progradation along a small (12-km-wide) mangrove forest allows many environmental variables to be held constant, and linkages to be established between measured processes and resultant morphology.

4.4 Methods

Field efforts were timed to coincide with the two dominant seasonal conditions in the Mekong Delta; the southwest monsoon (23 September–4 October 2014) and the northeast monsoon (3–16 March 2015). For the remainder of this paper we will refer to data from these two periods using the terms 'September' and 'March'. Field campaigns had a duration of ∼14 days in order to capture a spring-neap tidal cycle during each seasonal condition. Two sites were chosen within the Cù Lao Dung mangrove forest: one in the rapidly prograding southwest forest ∼2 km north of the southern (Trần Đề) channel of the Sông Hậo; and the other in the northeast part of the mangrove forest ∼2 km south of the northern (Định An) channel of the Sông Hậo (Figure 4.1). Simultaneous measurements were made at a 'middle' site roughly midway between the SW and NE sites (see Vo-Luong et al., 2017; Figure 4.1b). Field efforts comprised two foci: sediment sampling and coring of the substrate, and high-frequency time-series data collection in the water column.

4.4.1 Sediment Sampling and Coring

Sampling and coring was undertaken to examine short-term changes in sediment character between seasons, as well as patterns of sediment accumulation over decades to centuries. Grab samples were collected by hand or using a Van Veen grab from a small boat. Numerous short cores and x-ray trays (<60 cm) were pushed directly into the sediment by hand during low tides. A total of six long vibracores (4.5 - 5.5 m in length) were collected during both field campaigns on the unvegetated intertidal flat, at the mangrove/flat boundary, and within the mangrove forest.

X-radiographs were shot and developed in the field. Short cores and x-ray trays were cut into 2-cm intervals and bagged for grain-size and radiochemical analyses. Vibracores were cut into 2-m sections in the field and returned to the laboratory. A 1.5-cm thick medial slab was removed from each vibracore and and x-rayed using a Faxitron cabinet

x-ray system. One of the remaining one-third rounds was sealed for long-term storage, and the other was cut into 2-cm intervals and bagged for grain-size and radiochemical analyses. Grain-size distributions of the mud fraction (<64 μm) from each sample were determined using Micromeritics Sedigraph 5100, 5120, and 5125 particle sizers in the laboratory.

Sediment accumulation rates were determined using ^{210}Pb, a naturally occurring radioisotope that, because of its 22.3-year half-life, can be used to constrain sediment accumulation over the past century (Nittrouer et al., 1979). The activity of ^{210}Pb is determined by measuring that of its granddaughter, ^{210}Po, relative to a calibrated spike of ^{209}Po, via alpha spectrometry. The excess activity of ^{210}Pb is that above the supported level of ^{210}Pb produced from in-situ decay of ^{226}Ra, its effective parent isotope, in the sediment column. The sediment-accumulation rate (S) is calculated using:

$$S = \frac{\lambda z}{\ln(\frac{A_0}{A_z})} \tag{4.1}$$

where λ is the decay constant for ^{210}Pb, A_0 and A_z are excess ^{210}Pb activities at two points within the region of log-linear decay, and z is the difference in depth between A_0 and A_z. To account for variability in ^{210}Pb activity due to down-core fluctuations in grain size, activities were normalized to percent mud (<64 μm) in each sample. Total ^{210}Pb activity below the region of log-linear decay in the deepest cores is $\sim$1 dpm g^{-1} mud, so this value is used as the supported level for all cores.

4.4.2 Time-Series Observations

Instrument packages were placed at both the SW and NE sites in order to document hydrodynamics and sediment dynamics over timescales from individual waves to fortnightly tidal cycles. The same parameters were measured in both sites simultaneously using nearly identical instrumentation (Table 4.1). Although instruments were deployed at similar positions relative to the seaward edge of the mangrove forest, a steeper bed gradient at the NE site resulted in a lower absolute deployment elevation, and therefore greater depth of inundation. Instruments were configured to collect $\sim$6–8 minutes of data every 10 minutes. Aquadopp current profilers measured profiles of water velocity throughout the water column, and logged at 2 Hz. RBR Duos and Concerto included temperature, pressure, and optical backscatter

sensors, and logged at 6 Hz. Optical backscatter sensors (Seapoint and Campbell Scientific OBS 3+) were calibrated using *in-situ* water samples to obtain suspended-sediment concentrations. A 10-point calibration ($R^2 = 0.82$) was applied to the four Campbell Scientific OBS 3+ sensors attached to the Aquadopp current profilers and an 11-point calibration ($R^2 = 0.91$) was applied to Seapoint OBSs integrated into RBR Duo and Concerto instruments. Instruments were deployed in low-profile mounts to allow near-bed measurements while minimizing flow interference.

	parameters measured	southwest site	northeast site
mangrove/flat boundary	pressure (6Hz)	RBR Duo	RBR Concerto
	temperature	Hobo T	RBR Concerto
	salinity	Hobo C	RBR Concerto
	SSC	Seapoint OBS	Seapoint OBS
∼150m inside mangrove forest	water vel., pres., temp.	Nortek Aquadopp	Nortek Aquadopp
	salinity	Hobo C	Hobo C
	SSC at 15 and 40 cmab	Campbell Sci. OBS 3+	Campbell Sci. OBS 3+

Table 4.1: Summary of instruments deployed in the Cù Lao Dung mangrove forest during field campaigns in Septemer 2014 and March 2015.

4.5 Results

4.5.1 Sediment Character

Southwest Site

Mean sediment grain size at the SW site was coarser than at the NE site (Figure 4.3). The SW-site grain sizes varried both seasonally and spatially. Mean grain size from 44 surface sediment samples collected during September was ∼5.7 ϕ (∼19 μm), and increased to coarser than 4 ϕ (>64 μm) in March ($n = 23$). Sediment fined landward into the mangrove forest during both seasons. In September, the seabed was >75% sand at a distance 30 m landward of the forest edge, decreasing to <10% sand 150 m landward (Figure 4.4). In March, grain size along the entire transect coarsened, but the fining trend into the forest was still observed

(Figure 4.4). Repeat X-radiographs from the edge of the mangrove forest at the SW site also exhibit a coarsening of the upper 10 cm of the seabed between September and March (Figure 4.5).

Based on Landsat images collected between the 1970s and present, the SW part of the Cù Lao Dung mangrove forest has experienced an average progradation rate of ∼60 m y^{-1} (Figure 4.2). Such progradation is accomplished through accumulation of sediment within and offshore of the mangrove forest. Based on ^{210}Pb geochronology from two cores, the rate of sediment accumulation at the SW site is 3.0–5.1 cm yr^{-1} (Figure 4.7a,b). The lesser accumulation rate comes from a ∼5-m vibracore (MM-44) collected at the boundary between the mangrove forest and the unvegetated tidal flat. The greater accumulation rate was measured in a ∼2.7-m core (MM-208) collected in the central part of the mangrove forest ∼500 m landward of MM-44. The upper ∼75 cm of MM-44 comprise decimeter- to centimeter-scale beds with minor bioturbation from mangrove roots, and burrowing by crabs and mudskippers. Below ∼75 cm, the scale of bedding is reduced (mm–cm), and there is no evidence of bioturbation. Both MM-44 (Figure 4.6a) and MM-208 exhibit physical stratification throughout the cores, confirming that ^{210}Pb profiles are not significantly impacted by bioturbation, and that the accumulation rates are accurate (see Nittrouer et al., 1984; Sommerfield and Wheatcroft, 2007).

Northeast Site

The NE site experiences minor changes in grain size associated the transition from more quiescent September conditions to more energetic conditions in March (see Section 4.5.2). In September, the mean grain size of 23 surface sediment samples at the NE site was ∼7ϕ (∼8 μm) (Figure 4.3a). In March, mean grain size was unchanged (n=9), and the range in grain size was similar to that observed in September (Figure 4.3b). Based on Landsat images, the NE part of the Cù Lao Dung mangrove forest has has experienced little to no progradation since the mid-1970s (Figure 4.2). Sediment-accumulation rates at the NE site, as determined from two ∼5-m vibracores, are 0.8–2.8 cm yr^{-1} (Figure 4.7d, e). The greater accumulation rate was determined from a core (MM-95) collected on the unvegetated tidal

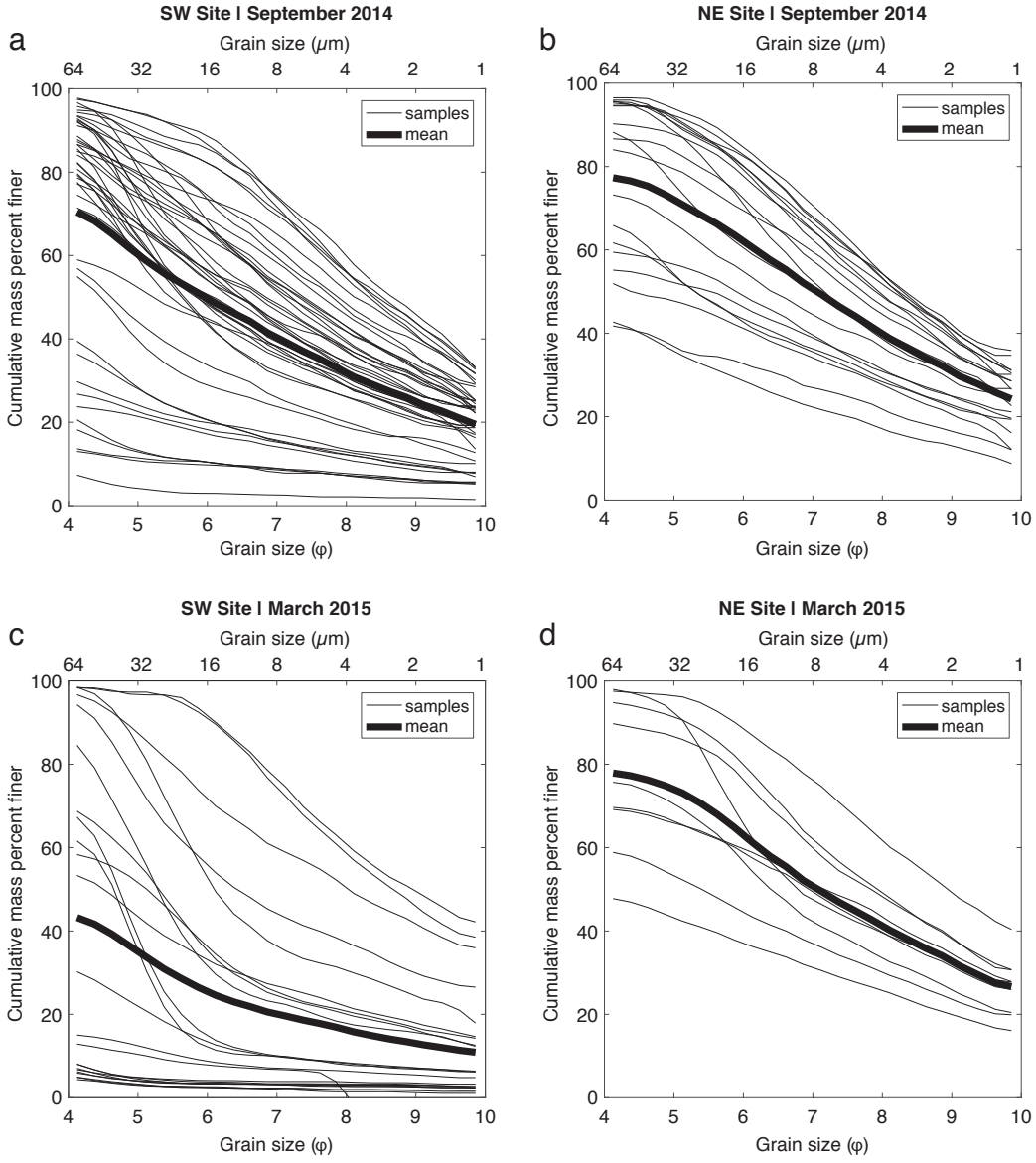

Figure 4.3: Comparison between surface-sediment grain-size distributions for the SW and NE sites during September 2014 and March 2015. Individual curves show the cumulative mass percent of each sample that is finer than the corresponding particle diameter in ϕ units (lower scale), and microns (upper scale). Bold black curves are the mean of the individual sample distributions shown. Sediment samples from the SW site (September: $n = 44$, March: $n = 23$) are generally coarser than samples from the NE site (September: $n = 20$, March: $n = 9$) and show a greater range in grain size. Mean grain size at the SW site is coarser in March than in September, while the mean grain size of samples from the NE site is very similar between the two seasons.

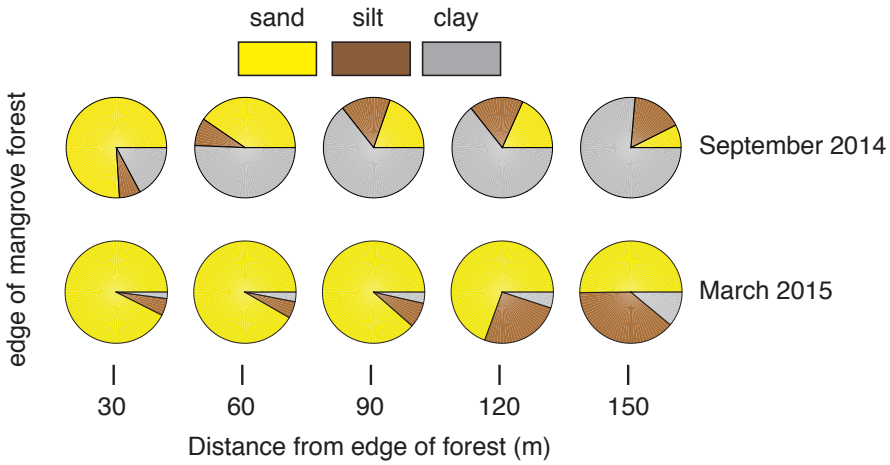

Figure 4.4: Repeat surface-sediment grain-size transect at the SW site during September 2014 and March 2015. Samples were collected along a transect extending from 30 inside the mangrove forest to a distance of 150 m from the seaward limit of the mangroves. Pie charts show the fraction of sand (yellow), silt (brown), and clay (gray) in each sample. Samples from both seasons show a fining trend into the mangrove forest, and samples collected in March are consistently coarser than samples collected at the same locations in September.

flat ∼300 m seaward of the mangrove forest. The lesser accumulation rate was determined for a core (MM-94) collected at the seaward edge of the mangrove forest. Bedding within core MM-94 is more chaotic than bedding observed at the SW site (Figure 4.6). Bioturbation has obliterated much of the physical structure above ∼65 cm. In general, the scale of beds in MM-94 are thicker than observed in MM-44 from the SW site. Below ∼65 cm, physical structure is present, reinforcing ^{210}Pb calculations of sediment-accumulation rate.

4.5.2 Hydro- and Sediment Dynamics

Southwest Site

During the two measurement periods, the SW site experienced larger waves, slightly stronger currents, and greater suspended-sediment concentrations than did the NE site (Table 4.2, Figures 4.8, 4.9). Mean depth-averaged tidal-current speeds were 11-12 cm s^{-1} regardless of season, while mean wave-orbital velocities varied between 21 and 46 cm s^{-1} (Figure 4.9a, c).

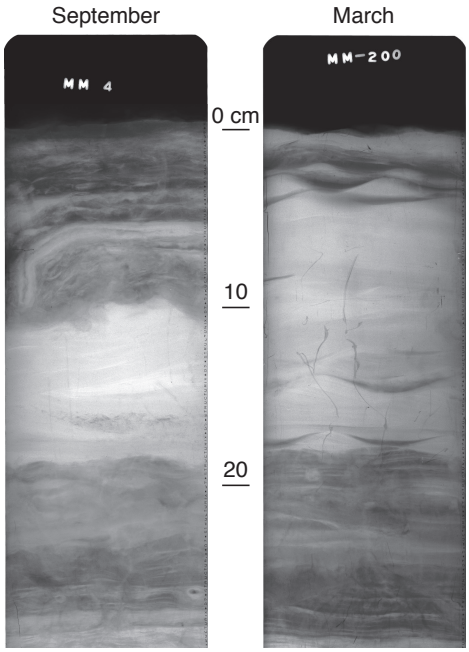

Figure 4.5: Repeat X-ray negatives (September and March) of the upper ∼28 cm of the seabed at the seaward edge of the mangrove forest at the SW site. Darker colors correspond to lower bulk density (more mud) and light colors indicate higher bulk density (more sand). X-radiographs were collected within 5 m of each other and show an increase in the proportion of sand in the upper 10 cm of the seabed between September and March.

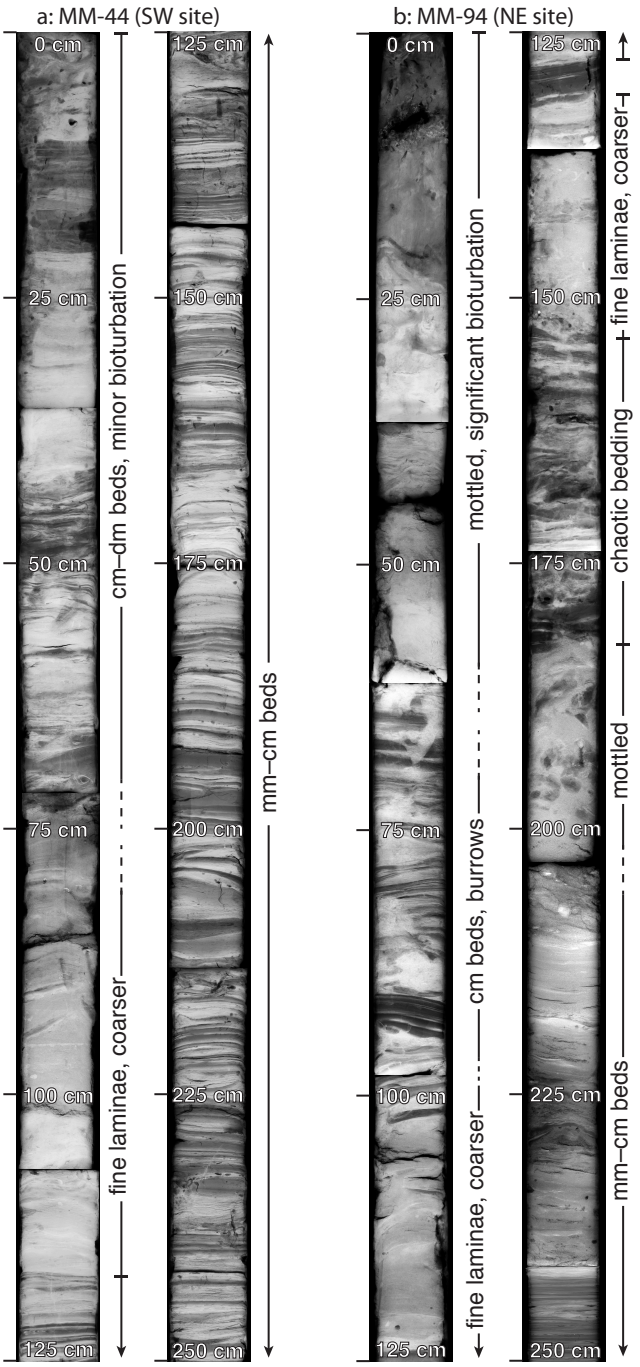

Figure 4.6: X-ray negatives of the upper 250 cm of two vibracores from the seaward edge of the Cù Lao Dung mangrove forest. Core MM-44 (a) was collected at the SW site, and core MM-94 (b) was collected at the NE site. Darker colors correspond to lower bulk density (more mud) and light colors indicate higher bulk density (more sand). Simplified core descriptions are shown to the right of each core section.

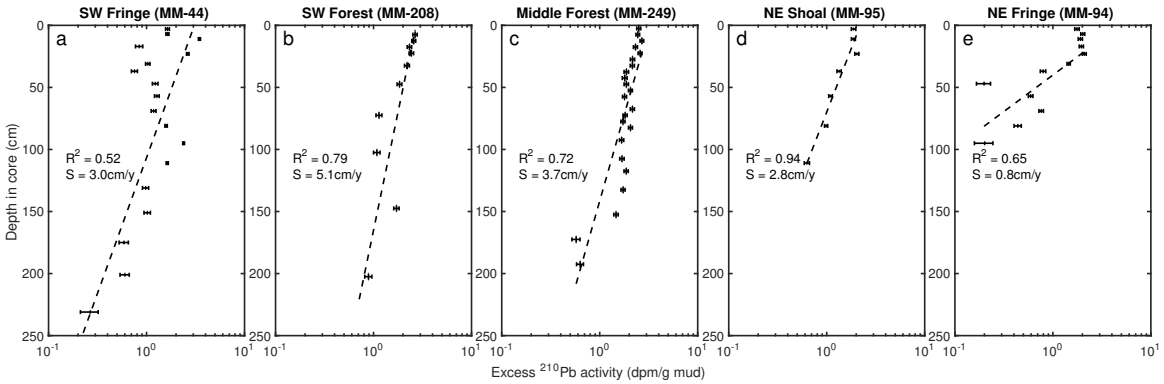

Figure 4.7: Profiles of excess ^{210}Pb from cores collected in or near the Cù Lao Dung mangrove forest. Panels a and b show data from cores at the SW site; MM-44 (a) was collected at the seaward edge of the mangrove forest, and MM-208 (b) was collected ∼500 m farther landward. Panel c shows data from a core (MM-249) collected in the interior of the mangrove forest at the middle site (see Vo-Luong et al., 2017). Panels d and e show data from cores collected at the NE site. MM-95 (d) was collected ∼300 m seaward of the mangrove forest on the unvegetated intertidal flat, and MM-94 (e) was collected at the boundary between the mangrove forest and flat. Log-linear regressions and correlation coefficients (R^2) are determined for the profile regions of log-linear decay, and the sediment accumulation rate (S) is shown.

The wave climate was more energetic during March, with waves as large 70 cm producing wave-orbital velocities >90 cm s^{-1} at the SW site (Table 4.2, Figure 4.9). Tidal-current speed is poorly correlated with SSC, suggesting tidal currents do not cause significant resuspension of sediment from the seabed, but advect sediment already in suspension within the mangrove forest. Variation in suspended-sediment concentration at the SW site is strongly influenced by wave-driven resuspension when the wave climate is sufficiently energetic. This is most apparent during the energetic March deployment when the majority of the variation in SSC can be explained by variation in wave-orbital velocity alone (see Figure 4.10c). Tidal-current speeds were largely unchanged between spring and neap tidal conditions, and the distribution of wave-orbital velocities was very similar across spring and neap portions of the study periods.

Season	**September 2014**		**March 2015**	
Site	SW	NE	SW	NE
H_{sig} mean (m)	0.12	0.07	0.27	0.21
H_{sig} max (m)	0.33	0.26	0.67	0.51
H_{sig} SD (m)	0.06	0.06	0.13	0.08
SSC mean (mg L^{-1})	400	190	920	210
SSC SD (mg L^{-1})	160	170	550	160
Salinity range (ppt)	0 - 2.5	0 - 6	11 -18	10 - 23
Temperature range (°C)	26 - 36	28 - 38	25 - 35	26 - 32

Table 4.2: Seasonal summary of wave, suspended-sediment concentration, salinity, and temperature data from instruments deployed on the mangrove/flat boundary (Table 4.1) at the SW and NE sites in the Cù Lao Dung mangrove forest. Mean significant wave heights (H_{sig}) and mean suspended-sediment concentrations (SSC) are statistically different between both seasons and sites at a 95% confidence level.

Salinity at the SW site varied greatly over the course of the year, with relatively fresh (0-2.5 PSU) water present during high-flow conditions in September and brackish conditions (11-18 PSU) during low flow of the Sông Hậo in March. At high flow of the river, the freshest waters were associated with the greatest SSCs (Figure 4.10e), while during low-flow conditions, waters with the greatest salinities carried the most sediment (Figure 4.10g).

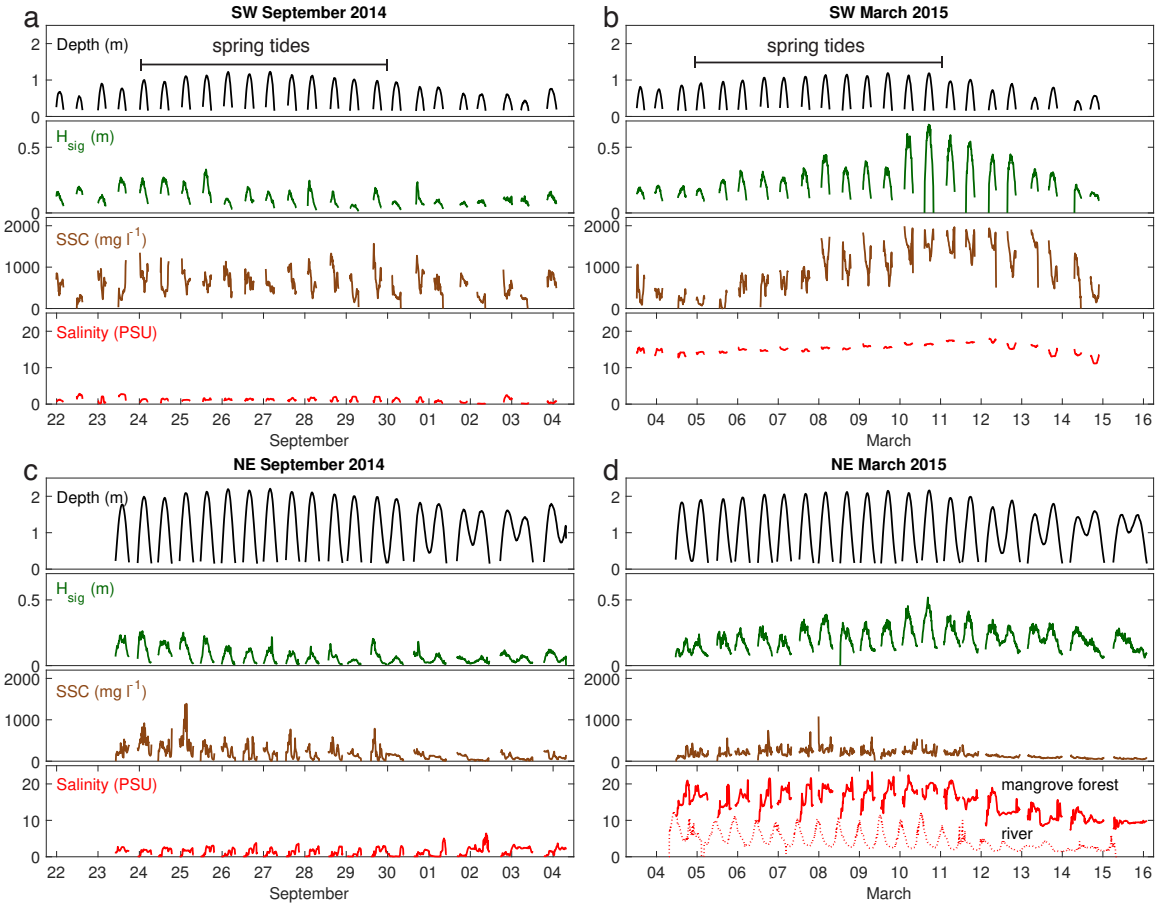

Figure 4.8: Plots of water depth, significant wave height (H_{sig}), suspended-sediment concentration (SSC), and salinity. Panels a and b show data from the SW site during September 2014 and March 2015, respectively. Depth, H_{sig}, and SSC were measured by an RBR-duo, and salinity was measured by a Hobo conductivity sensor. All sensors were located at the seaward edge of the mangrove forest (see Table 4.1). Panels c and d show data from the NE site during September 2014 and March 2015, respectively. Panel d also includes salinity data from the Định An channel (dashed red line) collected ~20 km upstream from the NE site using a YSI CTD. River salinity was 0 PSU during September 2014, and is not shown in panel c. All other parameters in panels c and d were measured by an RBR-concerto located at the seaward edge of the mangrove forest (see Table 4.1). The period of spring tidal conditions is marked for September and March deployments in panels a and b, respectively.

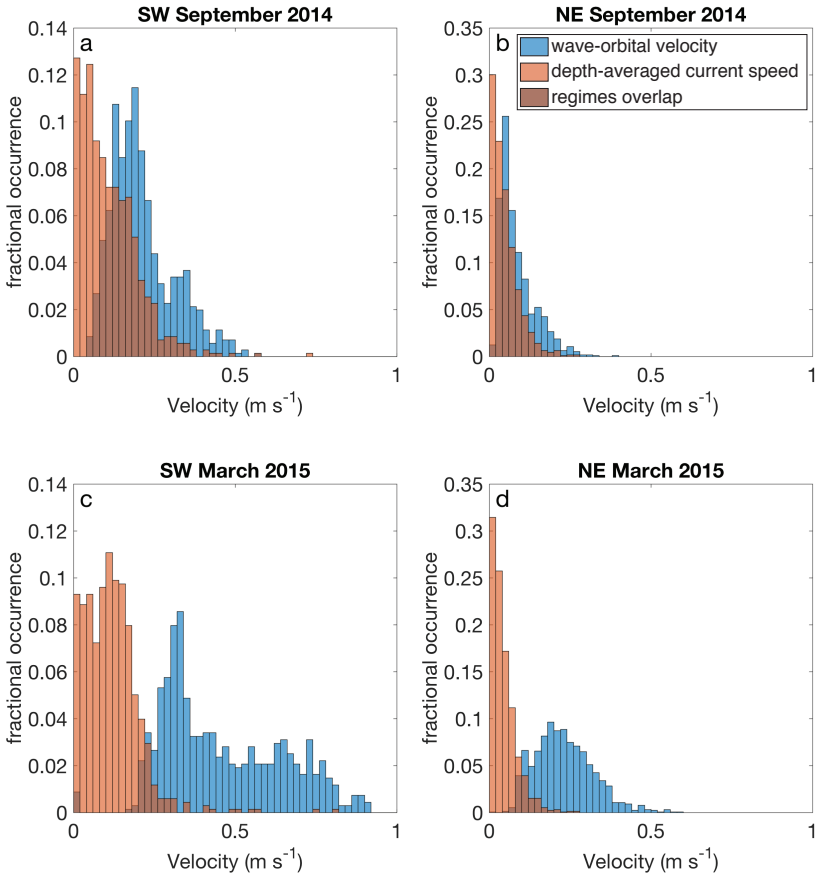

Figure 4.9: Four panels showing histograms of wave-orbital and depth-averaged current velocity for the SW and NE sites during September and March deployments. Blue-shaded bars represent wave-orbital velocities computed from 6-Hz pressure data collected at the mangrove–flat boundary, and semi-transparent light brown-shaded bars represent depth-averaged current velocities measured by Aquadopps locted 150 m inside the mangrove forest (see Table 4.1). Regions of overlap between the two distributions appear as dark brown. Plots a and b show data from the SW site, and plots b and d show data from the NE site.

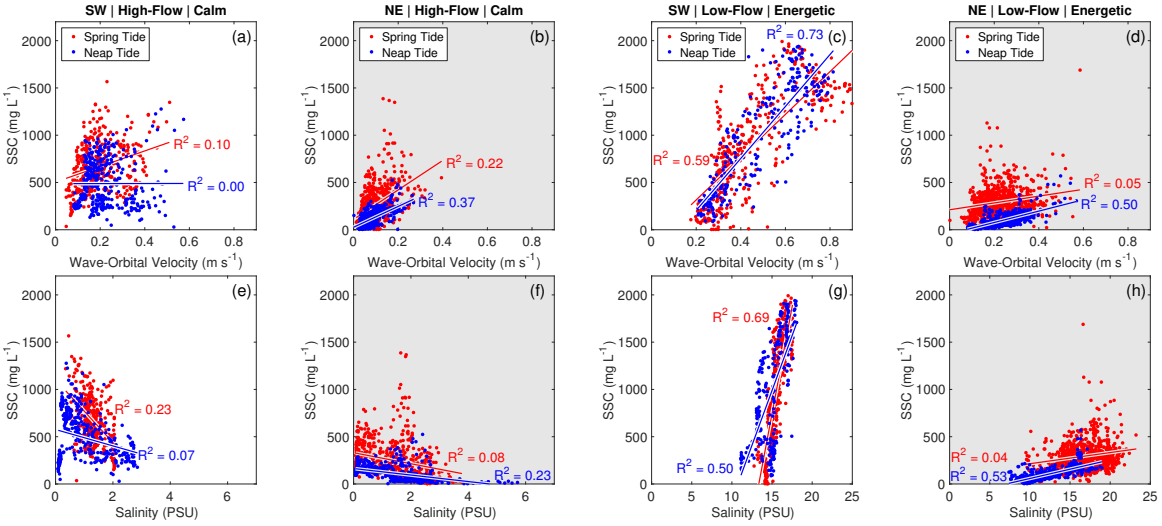

Figure 4.10: Eight plots showing the relationship between SSC and either wave-orbital velocity or salinity. Gray-shaded plots (b, d, f, h) represent data from the NE site, while unshaded plots (a, c, e, g) show data from the SW site. The four plots on the left show data from September (high-flow and calm), while the four plots on the right show data from the March (low flow and energetic). Data are colored such that red dots represent data collected during spring tides and blue dots represent data collected during neap tides. Trendlines are fit to both spring (red) and neap (blue) data in each panel, and correlation coefficients (R^2) are reported for each line.

Within each fortnightly deployment, we observed a similar range in wave-orbital velocity, salinity, and SSC regardless of timing within the spring–neap cycle (Figure 4.10).

The direction of sediment transport is assessed by calculating a sediment flux (Q_{sed}):

$$Q_{sed} = \int_0^H UC \, \mathrm{d}z \tag{4.2}$$

where U is water velocity, C is suspended-sediment concentration, and H is water depth. Practically, depth-integrated velocity is computed as the mean of the velocity profile measured by the Aquadopp, and the depth-averaged SSC is assumed to be the mean of the two SSC values determined by calibrated OBS's at 15 and 40 cmab. The direction of instantaneous measurements of flux varies over the course of the tide, but in a tidally averaged or fortnightly averaged sense, the sediment flux at the SW site was oriented into the mangrove forest (Figure 4.11). During the September experiment, the progressive sediment-flux vector was oriented into the mangrove forest $\sim$30° west of perpendicular to the shoreline. In March, the progressive sediment-flux vector had a greater alongshore component, being oriented $\sim$60° west of perpendicular to the local shoreline (Figure 4.11).

Northeast Site

In general, conditions at the NE site were less energetic than at the SW site during both seasons. Mean tide-driven currents were $\sim$4 cm s^{-1}, regardless of season (Figure 4.9b, d). During the more quiescent September deployment, small waves (Table 4.2) induced mean wave-orbital velocities of $\sim$8.5 cm s^{-1}. Wave heights roughly tripled in March, leading to mean wave-orbital velocities of $\sim$23 cm s^{-1} (Figure 4.9b, d). As at the SW site, there was a positive relationship between wave-orbital velocity and SSC during both seasons (Figure 4.10b, d).

Hydro- and sediment dynamics at the NE site vary dramatically over fortnightly tidal timescales. Although spring tides generally coincided with greater SSC values, the distribution of tide-driven current velocities did not change appreciably between periods of spring and neap tides, and the wave climate was very similar during both spring and neap tidal conditions. Spring–neap control on SSC was observed in both September and March, when

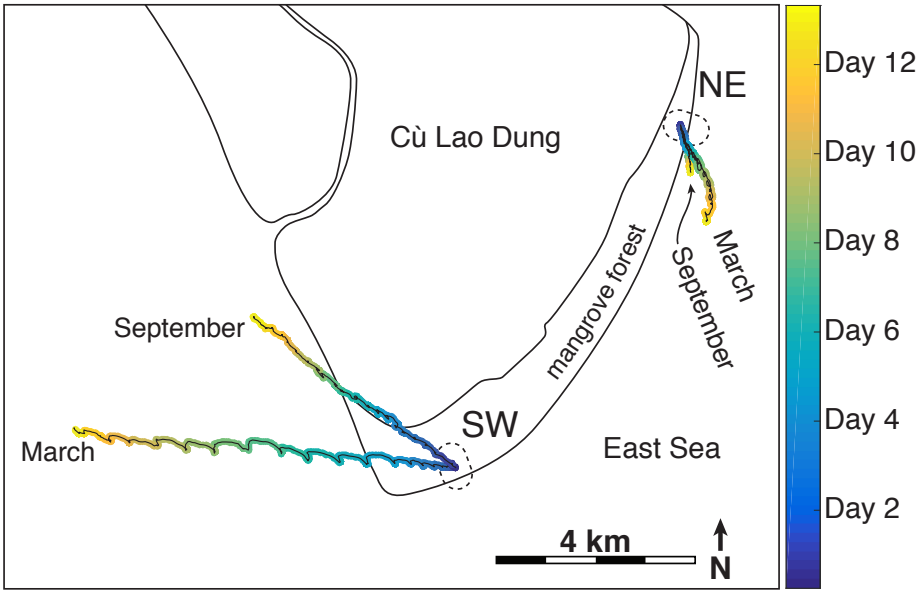

Figure 4.11: Map of the Cù Lao Dung mangrove forest showing the orientation of sediment flux at the SW and NE sites in September 2014 and March 2015. Colored lines are progressive vectors of sediment flux as measured by an Aquadopp current profiler and calibrated OBSs at the origin of each line ($\sim$ 150 m inside mangrove forest, see Table 4.1). These lines are constructed by joining sediment-flux vectors measured every 10 minutes in a tip-to-tail fashion. Line shading transitions from blue at the beginning of the deployment to yellow at the end of the deployment. Spring tidal conditions spanned roughly days 3-9 in September, and days 2-8 in March. Scaling of the vectors is arbitrary but all vectors are shown at the same scale.

neap tides coincided with reduced SSC regardless of wave energy (Figure 4.10b, d). Salinity at the NE site varied strongly over the course of the year, with relatively fresh (0-6 PSU) water present during September (high flow) and brackish conditions (8-22 PSU) during March (low flow). Salinity also varied on a fortnightly timescale with neap tides associated with saltier waters during September and with fresher waters during March (Figure 4.10f, h).

Progressive sediment-flux vectors computed for both September and March deployments are oriented out of the mangrove forest, suggesting a movement of sediment from the mangrove forest to the unvegetated flat near the NE site (Figure 4.11). The orientations of the progressive sediment-flux vectors are similar between seasons, with roughly equal offshore and alongshore (toward SW) components to the net flux. Three of the four computed progressive sediment-flux vectors (SW: September and March, NE: September) are relatively linear. The progressive sediment-flux vector for March at the NE site shows an increase in the alongshore (toward SW) component of flux roughly half way through the two-week deployment (Figure 4.11).

4.6 Discussion

4.6.1 Seasonal Control on Dynamics and Sediment Character

Hydro- and Sediment Dynamics

Seasonal variability in both river discharge and marine forcing (e.g., waves, currents) impacts hydro- and sediment dynamics in the mangrove forest of Cù Lao Dung. Sediment discharged by the Sông Hậo and other distributary channels of the Mekong River is the ultimate source of sediment supplied to the Cù Lao Dung mangrove forest. However, the greatest SSC and sediment fluxes do not coincide with peak discharge conditions in September (Figures 4.8, 4.11). This suggests that much of the sediment discharged from the Sông Hậo during peak-discharge conditions bypasses the mangrove-colonized shoreline of Cù Lao Dung. This pool of offshore sediment is subsequently remobilized during more energetic conditions associated with larger waves and coincident with seasonal low discharge of the river (i.e., March). Sediment stored offshore is moved landward by the interaction of river flow and tides (Eidam et al., 2017).

Waves are a dominant forcing mechanism in the Cù Lao Dung mangrove forest. As noted in Section 4.4.2, wave-logging instruments were deployed ∼1 m lower at the NE site than at the SW site. As a consequence, mean wave-orbital velocities measured at the NE site may be ∼5 cm s^{-1} slower than if measured at the same depth as the SW instruments. The larger waves observed at the SW site (Figure 4.8) are not the result of shoaling due to the shallower SW instrument location, because for a given water depth, significant wave heights at the SW site exceed those at the NE site. Waves, which show strong seasonal variation (Figure 4.9), exert a first-order control on SSC (Figure 4.10b–d), particularly at the SW site where wave-orbital velocities are substantially larger (Figure 4.9). There appears to be a gradient in wave energy across the Cù Lao Dung mangrove forest, with wave-orbital velocities observed to be largest at the SW site, intermediate at the middle site (Vo-Luong et al., 2017), and smallest at the NE site (Figure 4.12). Trà Vinh province projects into the East Sea northeast of Cù Lao Dung (Figure 4.1), and may shelter the middle and NE parts of the Cù Lao Dung mangrove forest from winds/waves coming predominantly from the northeast during March (Hu et al., 2000).

Although the relative change in the wave climate between September and March is similar for both the SW and NE sites (Figure 4.9), the SSC response is more pronounced at the SW site, where mean SSC more than doubles between these periods (Table 4.2). In contrast, mean SSC at the NE site is nearly unchanged between September and March (Table 4.2). The more pronounced SSC response at the SW site is consistent with the greater absolute increase in wave-orbital velocity at that location. This arises due to the positive non-linear relationship between transport and bed stress.

Sediment Character

Waves, as described above, play an important role in remobilizing sediment from the shallow continental shelf and unvegetated tidal flat for transport into the mangrove forest. This movement of material affects the character of the seabed both on the shelf where sediment may be sourced (Eidam et al., 2017), and within the mangrove forest where some of that sediment may be deposited. In addition, sediment sourced directly from adjacent river

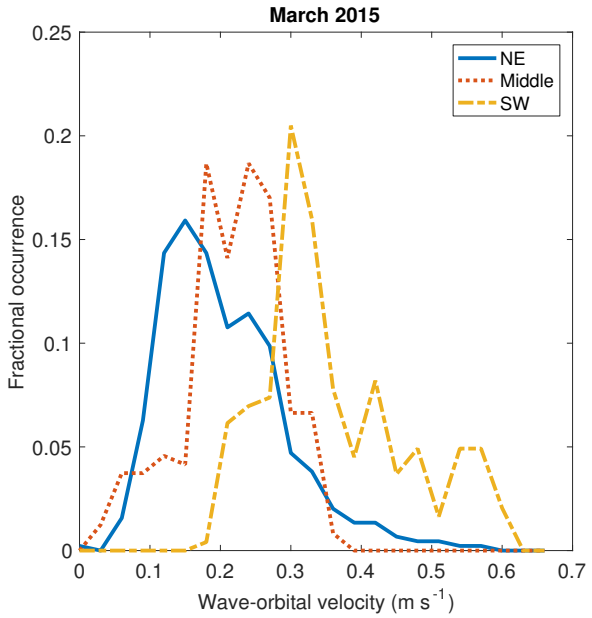

Figure 4.12: Distributions of wave-orbital velocities from the period 3–8 March 2015 at the NE (solid blue), middle (dotted red), and SW (dash-dot yellow) sites. Wave orbital velocities increase from NE to SW. Data from the middle site are from Vo-Luong et al. (2017).

channels is carried into the mangrove forest. The resultant character of the seabed reflects the influence of these diverse sediment-transport pathways, each of which varies on seasonal, fortnightly, and daily timescales.

In general, sediment is coarser at the SW site than at the NE site (Figure 4.3). This is consistent with the gradient in wave energy between the two locations (Figure 4.12). Repeat x-radiographs show an increase in the sand content of the upper 10 cm of the seabed during more energetic March conditions (Figure 4.5), suggesting that material is resuspended and the fines preferentially winnowed from the upper seabed. Because sediment flux is directed into the mangrove forest at the SW site during both seasons (Figure 4.11), fine sediment winnowed from areas with high bed stress (i.e., unvegetated tidal flat, seaward edge of mangrove forest) is likely carried into the forest and deposited as wave and current energy is attenuated by interaction with the bed and vegetation (e.g., Norris et al., 2017; Mullarney et al., 2017). The fining of sediment from the seaward edge of the forest into the interior (Figure 4.4) is consistent with such processes.

The subtle change in sediment grain size at the NE site between September and March (Figure 4.3c, d) is consistent with the similar ranges in SSC observed during both seasons at the site (Figure 4.8c,d). While the strength of waves nearly doubles at the NE site between September and March (Figure 4.9b,d), the relatively invariant SSC suggests that neither wave climate is sufficiently energetic to cause significant resuspension of sediment from the seabed. At the SW site, variability in wave energy exerts the greatest influence on SSC. However, at the NE site, SSC is most strongly influenced by changes in the estuarine regime of the adjacent Định An distributary channel, which propagate into the northeast mangrove forest.

4.6.2 Tidal Control on Hydro- and Sediment Dynamics

Semidiurnal Timescale

Currents driven by semidiurnal tides are an important means of moving water and sediment among the mangrove forest, unvegetated tidal flat, adjacent river channels, and ocean. Mean tidal current velocities are generally $<$15 cm s^{-1} within the mangrove forest, and

play a minor role in reworking or resuspending sediment from the bed. These relatively modest tidal currents do however provide a net current onto which largely oscillatory wave-driven velocities are superimposed, and therefore are a first-order control on the direction of sediment-transport within the mangrove forest (Figure 4.11).

Spring–Neap Timescale

At the SW site, spring–neap variability does not substantially impact hydro- or sediment dynamics. Mean tidal current speeds are relatively low (11-12 cm s^{-1}), and there is no change in tidal-current orientation over a full spring–neap cycle (Figure 4.11). Sediment resuspension is dominated by waves at the SW site, especially during more energetic March conditions when there is a strong relationship between wave-orbital velocity and SSC (Figure 4.10c).

In contrast, hydro- and sediment dynamics at the NE site are strongly impacted by processes that vary over spring–neap timescales. During both seasonal conditions, SSC and salinity measurements during neap tidal conditions are distinct from those during spring tidal conditions (Figure 4.10b,f,d,h). In September, SSC during spring tides was generally greater than during neap tides (Figure 4.10b). During these neap tides, some of the smallest SSC values were also associated with the greatest salinities (Figure 4.10f). While neap tides are also associated with reduced SSC at the NE site during March (Figure 4.10d), the relationship between SSC and salinity is the opposite of that observed in September. During March conditions, neap tides are associated with reduced salinity (Figure 4.10h).

This reduced SSC at the NE site during neap tidal conditions is not the product of reduced resuspension associated with a decrease in tidal current velocity or wave-orbital velocity. The reduction in mean depth-averaged current speed between spring and neap tidal conditions is minimal ($<$1 cm s^{-1}) during both seasons, and wave-orbital velocities are only subtly different during spring and neap tides. The relationship between reduced SSC and a change in salinity during neap tides suggests a change in the water mass reaching the NE mangrove forest. Changes in the character of the water mass at the NE site between spring and neap tides are the result of complex interactions between river and ocean. The

transition from spring to neap tidal conditions leads to increased stratification of the water column within the estuarine reach of the Định An channel (Nowacki et al., 2015; McLachlan et al., 2017).

During September conditions, when river discharge is greatest, and marine conditions are relatively quiescent, suspended-sediment concentrations are greater in river water than in the coastal ocean seaward of the mangrove forest. During this season, estuarine processes are pushed seaward of the river mouth for all but flood tides during neap tidal conditions, when an ephemeral tongue of saline water intrudes at depth into the river mouth (Wolanski et al., 1996; McLachlan et al., 2017). Although the water column is highly stratified during these times and the upper water column within the river channels is completely fresh, the increased stratification associated with the intrusion of a salt wedge represents a landward migration of marine water during neap tidal conditions. Through mixing of waters seaward of the mangrove forest or river mouth, shore-proximal marine water increases the salinity of waters at the NE site. Although suspended sediment is not a conservative tracer like salinity, the decrease in SSC during neap tidal conditions, in the absence of a decrease in wave or current energy, is consistent with increased contribution from low-SSC waters offshore.

During low-discharge conditions in March, waters of the energetic coastal ocean have the greatest SSC, and relatively low values of SSC are observed in the low-flow river channels (Nowacki et al., 2015). As opposed to September conditions, when water with a more marine signature (greater salinity, reduced SSC) is present at the NE site, during March, water with a more fluvial signature (less salinity, reduced SSC) is present at the NE site. During low discharge of the river in March, the Định An channel is a partially mixed estuary with greater SSC associated with more saline ocean water than with freshwater discharged by the river (Wolanski et al., 1998; Nowacki et al., 2015; McLachlan et al., 2017). Under these conditions, the transition from spring to neap tides results in greater stratification, causing the upper water column to become fresher (see river salinity in Figure 4.8d). The record of salinity at the NE site in the mangroves shows a very similar transition to that in the river channel, from more salinity (15–20 PSU) during spring tidal conditions to less salinity (9-15 PSU) during neap tidal conditions (Figure 4.8d). Consistent with reduced vertical mixing of ocean-derived sediment into the upper water column, this fresher water is also associated

with a marked reduction in SSC at the NE site (Figure 4.8d).

Estuarine processes acting in the Định An channel appear to reduce the delivery of sediment to the NE site during neap tides in both September and March. Such a relationship is not observed between the Trần Đề channel and the SW site. The lack of a spring–neap signal in sediment delivery to the SW site may be the result of proximity to the non-dominant distributary channel around Cù Lao Dung and/or the orientation of alongshore currents. The discharge and depth of the Trần Đề channel is less than the Định An channel (McLachlan et al., 2017). The increase in stratification observed in the Định An channel during neap tidal conditions in September and March is greater than that observed in the Trần Đề channel (McLachlan et al., 2017). Stratification increases as the balance between river discharge and tidal exchange moves toward greater river influence (Nowacki et al., 2015; McLachlan et al., 2017). Because of the lesser discharge of the Trần Đề channel, the balance between river discharge and tidal exchange does not favor the river and limits stratification in the Trần Đề channel and SW mangrove forest. The result is a continuous supply of sediment from the local distributary channel to the SW mangrove forest across spring and neap tidal conditions, and a near hiatus in sediment supply to the NE mangrove forest during neap tidal conditions throughout the year.

4.6.3 Integrating Short-Term Measurements into a Long-Term Record

Since at least the 1970's, satellite observations of the mangrove forest at the seaward edge of Cù Lao Dung show that the island has prograded seaward in an asymmetric fashion, with more rapid expansion near the southwest end of the forest, and minimal growth toward the northeast (Figure 4.2). Such asymmetric progradation is ultimately related to the balance between deposition and erosion of sediment at each location.

Considering the proximity of the entire mangrove forest to a major source of sediment (the Sông Hậo distributary of the Mekong River), the progradational asymmetry might be explained simply by a difference in hydrodynamic energy between the two sites (e.g., high stress leading to little accumulation and vice versa). However, such a relationship is not observed, and both wave and current stresses are more intense at the rapidly prograding

SW site than at the NE site during both seasonal conditions (Figure 4.12). The more rapid sediment accumulation and progradation rates in the southwest part of the forest are the result of a greater supply of sediment to that location relative to the northeast forest. This difference is largely attributable to the marked decrease in SSC during neap tidal conditions at the NE site in both September and March study periods (Figure 4.8). Because these two time periods bracket the range of environmental forcing, the relationship between neap tides and low SSC likely occurs throughout the year. In addition, the NE site experiences seaward-dominant fluxes of water and sediment over both semidiurnal and fortnightly tidal timescales, whereas sediment and water fluxes measured at the SW site have a net landward trend (Figure 4.11). Because the landward boundary of the mangrove forest is above the level of high tide, the net landward sediment fluxes measured at the SW site strongly imply flux convergence (i.e., deposition) within the mangrove forest landward of the location where sediment-flux measurements were made.

Sediment-accumulation rates determined using ^{210}Pb geochronology show that the century-scale rates of sediment accumulation are consistent with short-term dynamic measurements made over the two fortnight-long study periods. At the SW site, where modern rates of shoreline progradation (determined from satellite observations) are 10s meters per year, the sediment-accumulation rate is between 3.0 and 5.1 cm y^{-1} (Figure 4.7a, b). The sediment-accumulation rates determined from cores at the NE site are between 0.8 and 2.8 cm y^{-1} (Figure 4.7d, e). An additional core was collected at a location midway between the SW and NE sites (see Vo-Luong et al., 2017). The sediment-accumulation rate at this core location is 3.7 cm y^{-1} (Figure 4.7c), which falls between mean sediment-accumulation rates at the NE and SW sites.

The roughly two-fold decrease in sediment-accumulation rate between the SW and NE sites is consistent with dramatically lower rates of progradation (Figure 4.2) near the NE site. Accounting for local subsidence of $\sim$1.5 cm y^{-1} (Erban et al., 2014), sediment-accumulation rates at the NE site are consistent with either slight land loss due to local relative sea-level rise, or modest progradation. Rates of sediment accumulation at the SW site are greater than the rate of local subsidence by a factor of $\sim$2–3.5, which is consistent with progradation of the shoreline in the southwest part of the mangrove forest. There is good

agreement between rates of sediment accumulation and shoreline progradation at the SW site. In order to maintain the measured shore-perpendicular slope of 9.9×10^{-4} at the SW site (W. Nardin, *pers. comm.*, 2015) given a mean annual progradation rate of ∼60 m y^{-1} since the 1970s, new sediment would need to accumulate at ∼6 cm y^{-1}. This calculation ignores a number of potentially important time-varying phenomena (e.g., sea-level rise, subsidence) that could complicate this simple geometric relationship, but shows good agreement between geochronological and geomorphological estimates of coastal evolution.

Vibracores reveal the stratigraphy associated with a mangrove forest experiencing differential rates of progradation (Figure 4.6). Core MM-44 from the SW site is characterized by minimal bioturbation, interbedded sand and mud, and a down-core decrease in bed thickness. This stacking pattern is consistent with rapid progradation and an ample supply of sediment. Using a mean sediment accumulation rate of 4 cm y^{-1} (Figure 4.7a, b) and ignoring subsidence and sea-level rise, the 250 cm of core shown in Figure 4.6a represent ∼60 years of sediment accumulation. This rapid rate of sediment delivery to the bed would limit bioturbation, preserve individual beds through rapid burial, and decrease the local water depth. The resulting lateral migration of depositional environments from sub-tidal (mm–cm beds) through foreshore (cm–dm beds), is preserved in core MM-44.

Core MM-94 from the NE site preserves a record of sedimentation that is more episodic than that preserved at the SW site (Figure 4.6). Assuming a mean sediment-accumulation rate at the NE site of 1.8 cm y^{-1} (Figure 4.7d, e), the 250 cm of core shown in Figure 4.6b record ∼140 years of sedimentary history. The slower rate of sediment accumulation relative to the SW site may allow bioturbation to have more completely obscured primary sedimentary structures in the upper part of the core. There are a greater number of thicker beds preserved in MM-94 (NE) than in MM-44 (SW). If these thicker layers are associated with low-frequency events (e.g., storms, floods), then the longer period of time recorded in MM-94 would allow a greater number to be recorded in the core. Alternatively, the less-consistent bedding pattern preserved in MM-94 (relative to MM-44) could reflect the inconsistent supply of sediment to the NE site (see Section 4.6.2).

4.6.4 Comparison with Other Systems

The connection between fluvial sediment sources and mangrove forests is rarely straightforward. For example, the majority of coastal mangroves nourished by sediment from the Amazon River are displaced 100s–1000 kilometers north of the river mouth and sediment delivery is impacted by numerous oceanographic processes (e.g. Allison et al., 1995b; Fromard et al., 2004; Walcker et al., 2015). Similarly, the mangrove forests of the Sundarbans are displaced 10s–100 km west of the Ganges-Brahmaputra mouth (Allison and Kepple, 2001; Rogers et al., 2013). In both of these examples, the physical separation between source and sink allows time and space for marine forcing (e.g., winds, waves, tidal currents) to impact the timing and character of sediment delivered to the mangrove forests. In contrast, the mangrove forest on Cù Lao Dung is more proximal to its sources of sediment, yet even over this small spatial scale we observe dramatic differences in sediment delivery and accumulation between the SW and NE study sites.

Just as variability in oceanographic forcing explains many of the patterns and processes associated with mangrove sedimentation in spatially decoupled systems like the Amazon and Ganges-Brahmaputra, river-related processes strongly impact sediment dynamics in the more closely linked Cù Lao Dung mangrove forest. However, the connection between river source and mangrove sink is not entirely direct, as evidenced by peak sediment fluxes in the river and mangrove forest being out of phase. The connection between river/estuarine processes and mangrove sedimentation is most pronounced at the NE site during neap tidal conditions when changes in salinity and SSC within the Định An channel propagate (with some modification) into the NE part of the Cù Lao Dung mangrove forest (Figure 4.8d).

4.7 Conclusions

Mangrove forests are recognized as important ecosystems and critical elements of natural coastal resiliency in tropical environments. However, mangrove forests are generally in decline due to both anthropogenic (e.g., land reclamation, aquaculture) and natural (e.g. coastal erosion) forcing (e.g., Duke et al., 2007). Mangrove forests are not universally in decline (Shearman et al., 2013), and understanding the processes that drive the advance or

retreat of coastal mangrove forests is a crucial first step toward preserving what mangrove forests remain. The mangrove forest at the seaward edge of Cù Lao Dung in the Vietnamese Mekong Delta spans most of the range in shoreline trajectories experienced by mangrove forests around the world from rapid progradation of 10s of meters per year, to steady state, and even retreat. Because the entire forest extends <12 km along shore, differences observed between sites (e.g., SSC, salinity, currents) can be attributed to differences in local application of the same fundamental forcing (e.g., sediment supply, physical processes). Based on the above discussion we reach the following conclusions.

(1) Peak sediment fluxes within the mangrove forest occur during low-discharge of the Mekong River. Waves resuspend sediment on the shallow inner shelf and tidal flat seaward of the mangrove forest, and tidal currents transport that sediment landward.

(2) Progradation of the northeastern part of the Cù Lao Dung mangrove forest is limited due its proximity to the dominant Định An distributary channel. During neap tides in both September and March, increased stratification of the water column within the estuarine reach of the Định An channel leads to a >50% reduction in SSC compared to spring tidal conditions. This reduction in SSC combined with seaward-directed fluxes of water and sediment results in lower rates of sediment accumulation and shoreline progradation. Spring–neap variability does not appreciably affect sediment fluxes at the SW site where progradation is most rapid.

(3) The asymmetric progradation of Cù Lao Dung observed in satellite images over the past 40 years is consistent with rates of sediment accumulation determined using ^{210}Pb geochronology, suggesting that the patterns in sediment deposition and transport observed in the present are representative of the dominant processes acting over century timescales.

The interaction of fluvial, estuarine, and marine processes leads to marked differences in sediment transport and deposition within a mangrove forest immediately adjacent to a primary distributary channel of one of the world's largest rivers. This observation highlights the complexity of processes acting over small spatial scales both to deliver sediment to and and erode sediment from coastal mangrove forests.

Chapter 5

SUMMARY

For a considerable fraction of the sediment carried to the global ocean, tidal-river and adjacent coastal-mangrove environments represent the last two depositional environments encountered before reaching the sea. Most estimates of fluvial discharge to the ocean are based on measurements made upstream of tidal influence, and likely overestimate the amount of sediment that actually reaches the sea (Milliman and Farnsworth, 2011). Floodplains along the lower reaches of large rivers (e.g., Ganges-Brahmaputra: Goodbred and Kuehl, 1999, and Amazon: Nittrouer et al., 1995b; Dunne et al., 1998) have been suggested as possible sinks for this 'missing' sediment in these source-to-sink sediment budgets.

The objective of this research is not to close the gap in any sediment budget, but rather to elucidate sedimentary processes, pathways, and morphologies within tidal-river and linked mangrove environments that may modify the sediment fluxes that are currently estimated upstream of tidal influence. Chapter 2 examines the mechanisms of sediment exchange between the Amazon tidal river and the two largest tributaries along the tidal reach. The Tapajós and Xingu Rivers contribute ∼10% of the water discharged by the Amazon River, but because of the ria valleys near their confluences with the Amazon, these tributaries act as sinks for both tributary- *and* Amazon-derived sediment.

The mechanisms of sediment exchange vary as a function of relative fluvial and tidal influence. Barotropic flows driven by changes in the fluvial hydrograph upstream of the Tapajós Ria represent a more important sediment-delivery pathway than in the Xingu Ria, where greater tidal exchange, due to increased proximity to the ocean, likely dominates delivery to the ria. In addition to transport related to fluvial and tidal forcing, density-driven underflows transport Amazon water and sediment into the Xingu Ria, and wind-driven currents are responsible for upstream-directed flow within the Tapajós Ria. In addition to identifying these means of sediment exchange, a sediment-accumulation budget was determined for each

ria. In order to determine the amount of Amazon-derived sediment accumulating in each ria, the total annual sediment accumulation based on ^{210}Pb geochronology was compared to estimates of sediment discharge from each tributary. The result suggest that a combined total of ∼20 Mt of Amazon-derived sediment accumulates in the two ría basins each year. This is the first quantitative assessment of sediment trapping in any depositional environment along the Amazon tidal river.

While the Tapajós and Xingu Rias are important depositional environments in their own right, their scale is dwarfed by that of the floodplain of the Amazon tidal river, which extends ∼800 km from Óbidos to the Atlantic ocean. Chapter 3 examines the evolution of river bank and floodplain morphology along the tidal river along the fluvial–tidal transition. Dynamics and deposits in the upper reaches of tidal rivers (e.g., Tapajós Ria, Lago Grande de Monte Alegre) bear a strong resemblance to those characteristic of similar environments upstream of tidal influence. Similarly, sedimentary processes in the lower tidal river are dominated by tides, and although salinity is lacking, the morphologies created by these processes strongly resemble those in marine tidal environments. Even in these end-member environments, the interplay of both fluvial and tidal signals is present. This amalgam of processes is most evident in the central tidal river where high-frequency tidal oscillations are superimposed on the gradual rise and fall of the fluvial hydrograph. This reach of the river, which is perhaps unique to tidal rivers, requires a balance of fluvial and tidal influence in which tides are intense enough to disrupt diffusive levee-building, as is characteristic of the upper tidal river, but not so intense as to infill the floodplain, as is the case in the lower tidal river.

While this work makes no integrated assessment of sediment trapping, it highlights the importance of along-river variation in dynamics and resultant morphology on the potential for sediment trapping in the floodplain. For example, across-levee advection due to tides is too weak in the upper tidal river to suppress levee building, leading to floodplains with significant accommodation space but sufficiently efficient transport processes to fill it. This is in contrast to the lower tidal river, which experiences very efficient sediment transport via channelized tidal currents, but nearly all accommodation space has already been filled. This would suggest that if the floodplain of the Amazon tidal river acts to trap a significant fraction of the discharge gauged at Óbidos (e.g. Nittrouer et al., 1995b; Dunne et al., 1998),

then the central tidal river may play a disproportionally large role in such trapping.

Regardless of sediment trapping in depositional environments along tidal rivers, the vast majority of sediment carried by rivers is discharged to the coastal ocean. Sediment discharged to the coast is influenced by both the fluvial (or estuarine) process of delivery, as well as marine processes (e.g., waves, currents) that act to redistribute it along shorelines or into deeper water. Chapter 4 explores the interplay between fluvial and marine forcing in a coastal mangrove forest on the island of Cù Lao Dung at the mouth of the Mekong tidal river. The island is prograding seaward in an asymmetric manner, with more rapid seaward advance near the southern distributary channel than near the northern channel. The forest spans the shoreline between these two distributary mouths and signals of fluvial influence are easily resolved within the mangrove forest. Although the ultimate source of sediment to the mangrove coastline is fluvial, it is observed that fluvial influence serves to inhibit shoreline progradation in parts of the Cù Lao Dung mangrove forest. Moreover, rates of sediment accumulation and shoreline advance are greatest where direct fluvial influence is least, and marine energy is greatest. These counterintuitive findings suggest that although many mangrove forests rely on a supply of sediment from nearby rivers, processes operating in the coastal zone such a seasonal storage, wave resuspension, and littoral processes are needed to effectively deliver that sediment to mangrove forests.

The research presented here is an important contribution to the understanding of dynamics and deposits associated with the transition from fluvial to marine environments. Each of the environments studied here is shaped by terrestrial inputs of water and sediment that are subject to modification by processes acting on timescales from seconds to years. The morphology of each environment reflects the relative contribution of fluvial, tidal, and other marine influences. These results add important information about processes operating in and between two of the downstream-most terrestrial depositional environments in the source-to-sink system.

BIBLIOGRAPHY

Aalto, R. and Nittrouer, C. A. (2012). ^{210}Pb geochronology of flood events in large tropical river systems. *Phil. Trans. R. Soc. A*, 370:2040–2074.

Adams, P. N., Slingerland, R. L., and Smith, N. D. (2004). Variations in natural levee morphology in anastomosed channel flood plain complexes. *Geomorphology*, 61:127–142.

Alcântara, E., Novo, E., and Stech, J. (2010). A contribution to understanding the turbidity behaviour in an Amazon floodplain. *Hydrology and Earth System Sciences*, 14:351–364.

Allen, J. R. L. (1964). Studies in fluviatile sedimentation: Six cyclothems from the Lower Old Red Sandstone, Anglo-Welsh Basin. *Sedimentology*, 3:163–198.

Allison, M. A. and Kepple, E. B. (2001). Modern sediment supply to the lower delta plain of the Ganges-Brahmaputra River in Bangladesh. *Geo-Marine Letters*, 21:66–74.

Allison, M. A., Nittrouer, C. A., and Faria, L. E. C. (1995a). Rates and mechanisms of shoreface progradation and retreat downdrift of the Amazon River south. *Marine Geology*, 125:373–392.

Allison, M. A., Nittrouer, C. A., and Kineke, G. C. (1995b). Seasonal sediment storage on mudflats adjacent to the Amazon River. *Marine Geology*, 125:303–328.

Alongi, D. M. (2002). Present state and future of the world's mangrove forests. *Environmental Conservation*, 29:331–349.

Alongi, D. M. (2008). Mangrove forests: Resilience, protection from tsunamis, and responses to global climate change. *Estuarine Coastal And Shelf Science*, 76:1–13.

Andel, T. J. H. V. (1967). The Orinoco Delta. *Journal of Sedimentary Research*, 37:297–310.

Archer, A. W. (2005). *Review of Amazonian depositional systems.* Fluvial Sedimentology VII, International Association of Sedimentologists.

Asp, N. E., Gomes, V. J. C., Ogston, A., Borges, J. C. C., and Nittrouer, C. A. (2016). Sediment source, turbidity maximum, and implications for mud exchange between channel and mangroves in an Amazonian estuary. *Ocean Dynamics*, 66:285–297.

Bagnold, R. A. (1966). An approach to the sediment transport problem from general physics. Technical Report United States Geological Survey Professional Paper 422-I.

Baltzer, F., Allison, M. A., and Fromard, F. (2004). Material exchange between the continental shelf and mangrove-fringed coasts with special reference to the Amazon–Guianas coast. *Marine Geology*, 208:115–126.

Barua, D. K. (1990). Suspended sediment movement in the estuary of the Ganges-Brahmaputra-Meghna river system. *Marine Geology*, 91:243–253.

Benninger, L. K. and Wells, J. T. (1993). Sources of sediment to the Neuse River estuary, North Carolina. *Marine Chemistry*, 43:137–156.

Blum, M., Martin, J., Milliken, K., and Garvin, M. (2013). Paleovalley systems: Insights from Quaternary analogs and experiments. *Earth-Science Reviews*, 116.

Bonnet, M., Barroux, G., Martinez, J., and Seyler, F. (2008). Floodplain hydrology in an Amazon floodplain lake (Lago Grande de Curuaí). *Journal of Hydrology*, 349:18–30.

Bridges, P. H. and Leeder, M. R. (1976). Sedimentary model for intertidal mudflat channels, with examples from the Solway Firth, Scotland. *Sedimentology*, 23:533–552.

Brierley, G. J., Ferguson, R. J., and Woolfe, K. J. (1997). What is a fluvial levee? *Sedimentary Geology*, 114:1–9.

Carter, L., Orpin, A. R., and Kuehl, S. A. (2010). From mountain source to ocean sink – the passage of sediment across an active margin, Waipaoa Sedimentary System, New Zealand. *Marine Geology*, 270:1–10.

Church, J. A., Clark, P. U., Cazenave, A., Gregory, J. M., Jevrejeva, S., Levermann, A., Merrifield, M. A., Milne, G. A., Nerem, R. S., Nunn, P. D., Payne, A. J., Pfeffer, W. T.,

Stammer, D., and Unnikrishnan, A. S. (2013). Sea level change . In Stocker, F. D., Quin, D., Plattner, G. K., Tignor, M., Allen, S. K., Boschung, J., Nauels, A., Xia, Y., Bex, V., and Midgley, P. M., editors, *Climate change 2013: The physical science basis. Contribution of working group I to the fifth assessment report of the Intergovernmental Panel on Climate Change*, pages 1137–1216. Cambridge University Press, Cambridge, United Kingdom and New York, NY, USA.

Coleman, J. M. (1969). Brahmaputra river: Channel processes and sedimentation. *Sedimentary Geology*, 3:129–239.

Csanady, G. T. (1973). Wind-induced barotropic motions in long lakes. *Journal of Physical Oceanography*, 3:429–438.

Dalrymple, R. W., Mackay, D. A., Ichaso, A. A., and Choi, K. S. (2011). Processes, Morphodynamics, and Facies of Tide-Dominated Estuaries. In *Principles of Tidal Sedimentology*, pages 79–107. Springer Netherlands, Dordrecht.

Davis, J. H. (1940). *The ecology and geologic role of mangroves in Florida*, volume 32. Papers of the Tortugas Laboratory.

Driscoll, N. and Nittrouer, C. A. (2000). Source to sink studies. *MARGINS Newsletter*, 5:1–3.

Droppo, I. G. and Ongley, E. D. (1994). Flocculation of suspended sediment in rivers of southeastern Canada. *Water Research*, 28:1799–1809.

Duke, N. C., Meynecke, J.-O., Dittmann, S., Ellison, A. M., Anger, K., Berger, U., Cannicci, S., Diele, K., Ewel, K. C., Field, C. D., Koedam, N., Lee, S. Y., Marchand, C., Nordhaus, I., and Dahdouh-Guebas, F. (2007). A world without mangroves? *Science*, 317:41–42.

Dunne, T., Mertes, L. A. K., Meade, R. H., Richey, J. E., and Forsberg, B. R. (1998). Exchanges of sediment between the flood plain and channel of the Amazon River in Brazil. *Geological Society of America Bulletin*, 110:450–467.

Eidam, E. et al. (2017). Wave, tide, and sediment controls on the geometry the shallow Mekong clinoform. *Continental Shelf Research, in review.*

Eisma, D. (1986). Flocculation and de-flocculation of suspended matter in estuaries. *Netherlands Journal of Sea Research*, 20:183–199.

Elliott, M. and McLusky, D. S. (2002). The need for definitions in understanding estuaries. *Estuarine Coastal And Shelf Science*, 55:815–827.

Ellison, J. C. (2008). Wetlands of the Pacific Island region. *Wetlands Ecology and Management*, 17:169–206.

Erban, L. E., Gorelick, S. M., and Zebker, H. A. (2014). Groundwater extraction, land subsidence, and sea-level rise in the Mekong Delta, Vietnam. *Environmental Research Letters*, 9:084010.

Filizola, N. and Guyot, J. L. (2009). Suspended sediment yields in the Amazon basin: an assessment using the Brazilian national data set. *Hydrological Processes*, 23:3207–3215.

Fisk, H. N. (1947). *Fine-grained alluvial deposits and their effects on Mississippi River activity.* Mississippi River Commission, Waterways Experiment Station, Vicksburg, Mississippi.

Fitzjarrald, D., Sakai, R., and De Moraes, O. (2009). LBA-ECO CD-03 Mesoscale Meteorological Data, Santarem Region, Para, Brazil: 1998-2006.

Freitas, T., Asp, N., Souza Filho, P., Nittrouer, C., Ogston, A., and da Silva, M. (2017). Tidal influence on the hydrodynamics and Sediment entrapment in a major Amazon River triburary – lower Tapajós River. *Journal of South American Earth Sciences, in prep.*

Frey, R. W. and Basan, P. B. (1985). Coastal Salt Marshes. In Davis, R. A., editor, *Coastal sedimentary environments*, pages 225–302. Springer-Verlag, New York, NY.

Fricke, A. T., Nittrouer, C. A., Ogston, A. S., Nowacki, D. J., Asp, N. E., and Souza-Filho, P. W. M. (2017a). Evolution of the intertidal floodplain of the Amazon tidal river along the fluvial–tidal continuum, in prep.

Fricke, A. T., Nittrouer, C. A., Ogston, A. S., Nowacki, D. J., Asp, N. E., Souza-Filho, P. W. M., and de Silva, M. S. (2017b). River tributaries as sediment sinks: Processes operating where the Tapajós and Xingu Rivers meet the Amazon tidal river. *Sedimentology, in revision*.

Friedrichs, C. T. (2011). Tidal flat morphodynamics: a synthesis . In McLusky, D. and Wolanski, E., editors, *Treatise on Estuarine and Coastal Science*, pages 137–170. Elsevier.

Fromard, F., Vega, C., and Proisy, C. (2004). Half a century of dynamic coastal change affecting mangrove shorelines of French Guiana. A case study based on remote sensing data analyses and field surveys. *Marine Geology*, 208:265–280.

Geyer, W. R., Beardsley, R. C., and Lentz, S. J. (1996). Physical oceanography of the Amazon shelf. *Continental Shelf . . . .*

Gibbs, R. J. (1967). Amazon river: environmental factors that control its dissolved and suspended load. *Science*, 156:1734–1737.

Gibbs, R. J. (1970). Circulation in the Amazon River estuary and adjacent Atlantic Ocean. *Journal of Marine Research*, 28:113–123.

Goodbred, S. L. (2003). Response of the Ganges dispersal system to climate change: a source-to-sink view since the last interstade. *Sedimentary Geology*, 162:83–104.

Goodbred, S. L. and Kuehl, S. A. (1999). Holocene and modern sediment budgets for the Ganges-Brahmaputra river system: Evidence for highstand dispersal to flood-plain, shelf, and deep-sea depocenters. *Geology*, 27:559–562.

Granek, E. F. and Ruttenberg, B. I. (2007). Protective capacity of mangroves during tropical storms: a case study from 'Wilma' and 'Gamma' in Belize. *Marine Ecology Progress Series*, 343:101–105.

Guyot, J. L., Jouanneau, J. M., Soares, L., Boaventura, G. R., Maillet, N., and Lagane, C. (2007). Clay mineral composition of river sediments in the Amazon Basin. *Catena*, 71:340–356.

Hobbs, C. (2004). Geological history of Chesapeake Bay, USA. *Quaternary Science Reviews*, 23:641–661.

Hoitink, A. and Jay, D. A. (2016). Tidal river dynamics: implications for deltas. *Reviews of Geophysics*, 54:240–272.

Holgate, S. J. and Woodworth, P. L. (2004). Evidence for enhanced coastal sea level rise during the 1990s. *Geophysical Research Letters*, 31:L07305.

Hu, J., Kawamura, H., Hong, H., and Qi, Y. (2000). A Review on the Currents in the South China Sea: Seasonal Circulation, South China Sea Warm Current and Kuroshio Intrusion. *Journal of Oceanography*, 56(6):607–624.

Irion, G. (1984). Sedimentation and sediments of Amazonian rivers and evolution of the Amazonian landscape since Pliocene times. In Sioli, H., editor, *The Amazon*, pages 201–214. DR W. Junk Publishers, Dordrecht.

Irion, G., Bush, M. B., Nunes de Mello, J. A., Stüben, D., Neumann, T., Müller, G., Morais de, J. O., and Junk, J. W. (2006). A multiproxy palaeoecological record of Holocene lake sediments from the Rio Tapajós, eastern Amazonia. *Palaeogeography Palaeoclimatology Palaeoecology*, 240:523–535.

Irion, G., Mello, J. A. S. N., Morais, J., Piedade, M. T. F., Junk, W. J., and Garming, L. (2010). Development of the Amazon valley during the middle to late Quaternary: sedimentological and climatological observations. In Caldwell, M. M., Heldmaier, G., Jackson, R. B., Lange, O. L., Mooney, H. A., Schulze, E. D., and Sommer, U., editors, *Amazonian Floodplain Forests*, pages 27–42. Springer Netherlands, Dordrecht.

Iseya, F. and Ikeda, H. (1989). Sedimentation in coarse-grained sand-bedded meanders: distinctive deposition of suspended sediment. In Taira, A. and Masuda, F., editors, *Sedimentary Facies in the Active Plate Margin*, pages 81–112. Terra Scientific Publishing, Tokyo.

Junk, W., Bayley, P., and Sparks, R. (1989). The flood pulse concept in river-floodplain systems. *Canadian special publication of fisheries and aquatic sciences*, 106:110–127.

Keil, R. G., Montluçon, D. B., Prahl, F. G., and Hedges, J. I. (1994). Sorptive preservation of labile organic matter in marine sediments. *Nature*, 370(6490):549–552.

Keim, G., Irion, G., Behling, H., Junk, W., and de Mello, J. N. (1999). The sediment deposits of Lago Calado, a ria-lake in Central Amazonia (Brazil), as indicator for postglacial water level rise of the Amazon River . In *International Symposium on Hydrological and Geochemical Processes in Large-Scale River Basins*, Manaus, Brazil.

Klammer, G. (1984). The relief of the extra-Andean Amazon basin. In Sioli, H., editor, *The Amazon*, pages 47–83. DR W. Junk Publishers, Dordrecht.

Kosuth, P., Callede, J., Laraque, A., Filizola, N., Guyot, J. L., Seyler, P., Fritsch, J. M., and Guimaraes, V. (2009). Sea-tide effects on flows in the lower reaches of the Amazon River. *Hydrological Processes*, 23:3141–3150.

Krauss, K. W., Allen, J. A., and Cahoon, D. R. (2003). Differential rates of vertical accretion and elevation change among aerial root types in Micronesian mangrove forests. *Estuarine Coastal And Shelf Science*, 56:251–259.

Kravtsova, V. I., Mikhailov, V. N., and Kidyaeva, V. M. (2009). Hydrological regime, morphological features and natural territorial complexes of the Irrawaddy River Delta (Myanmar). *Water Resources*, 36:243–260.

Kuehl, S. A., DeMaster, D. J., and Nittrouer, C. A. (1986). Nature of sediment accumulation on the Amazon continental shelf. *Continental Shelf Research*, 6:209–225.

Kuehl, S. A. and Nittrouer, C. A. (2011). Exploring the transfer of Earth surface materials from source to sink. *Eos, Transactions American Geophysical Union*, 92:188.

Kuehl, S. A., Nittrouer, C. A., Allison, M. A., Faria, L. E. C., Dukat, D. A., Jaeger, J. M., Pacioni, T. D., Figueiredo, A. G., and Underkoffler, E. C. (1996). Sediment deposition, accumulation, and seabed dynamics in are energetic fine-grained coastal environment. *Continental Shelf Research*, 16:787–815.

Latrubesse, E. M. and Franzinelli, E. (2002). The Holocene alluvial plain of the middle Amazon River, Brazil. *Geomorphology*, 44:241–257.

Latrubesse, E. M., Stevaux, J. C., and Sinha, R. (2005). Tropical rivers. *Geomorphology*, 70:187–206.

Lewin, J., Ashworth, P. J., and Strick, R. J. P. (2016). Spillage sedimentation on large river floodplains. *Earth Surface Processes And Landforms*.

Lynch, J. C., Meriwether, J. R., McKee, B. A., Vera-Herrera, F., and Twilley, R. R. (1989). Recent Accretion in Mangrove Ecosystems Based on ^{137}Cs and ^{210}Pb. *Estuaries*, 12:284–299.

Mazda, Y., Magi, M., Ikeda, Y., Kurokawa, T., and Asano, T. (2006). Wave reduction in a mangrove forest dominated by Sonneratia sp. *Wetlands Ecology and Management*, 14:365–378.

Mazda, Y., Wolanski, E., King, B., Sase, A., Ohtsuka, D., and Magi, M. (1997). Drag force due to vegetation in mangrove swamps. *Mangroves and Salt Marshes*, 1:193–199.

McLachlan, R. et al. (2017). Sediment and hydrodynamics in the tidal river to estuarine reach of the Mekong River. *Continental Shelf Research, in review*.

Mead, R. H. (1969). Landward Transport of Bottom Sediments in Estuaries of the Atlantic Coastal Plain. *Journal of Sedimentary Research*, 39:222–234.

Mead, R. H., Nordin, C. F., Curtis, W. F., Rodrigues, F. M. C., Do Vale, C. M., and Edmond, J. M. (1979). Sediment loads in the Amazon River. *Nature*, 278:161–163.

Meade, R. H. (1985). Suspended sediment in the Amazon River and its tributaries in Brazil during 1982-84. Technical report, USGS.

Meade, R. H., Dunne, T., Richey, J. E., Santos, U. D., and Salati, E. (1985). Storage and Remobilization of Suspended Sediment in the Lower Amazon River of Brazil. *Science*, 228:488–490.

Mertes, L. A. K. (1994). Rates of flood-plain sedimentation on the central Amazon River. *Geology*, 122:171–174.

Mertes, L. A. K. (1997). Documentation and significance of the perirheic zone on inundated floodplains. *Water Resources Research*, 33:1749–1762.

Mertes, L. A. K. and Dunne, T. (2008). Effects of Tectonism, Climate Change, and Sea-level Change on the Form and Behaviour of the Modern Amazon River and its Floodplain. In Gupta, A., editor, *Large Rivers: Geomorphology and Management*, pages 115–144. John Wiley & Sons, Ltd., West Sussex, England.

Mertes, L. A. K., Dunne, T., and Martinelli, L. A. (1996). Channel-floodplain geomorphology along the Solimoes-Amazon River, Brazil. *Geological Society of America Bulletin*, 108:1089–1107.

Milliman, J. D. and Farnsworth, K. L. (2011). *River Discharge to the Coastal Ocean.* A Global Synthesis. Cambridge University Press, Cambridge.

Milliman, J. D. and Meade, R. H. (1983). World-wide delivery of river sediment to the oceans. *The Journal of Geology*, 91:1–21.

Moore, D. M. and Reynolds, R. C. (1997). *X-ray Diffraction and the Identification and Analysis of Clay Minerals.* Oxford University Press, USA.

Moreira-Turcq, P., Jouanneau, J. M., and Turcq, B. (2004). Carbon sedimentation at Lago Grande de Curuai, a floodplain lake in the low Amazon region: insights into sedimentation rates. *Palaeogeography*, 214:27–40.

Mullarney, J., Henderson, S., Norris, B., and Bryan, K. (2017). Drag and flow rotation within a mangrove forest in the Mekong Delta. *Continental Shelf Research, in review.*

Nardin, W., Locatelli, S., Pasquarella, V., Rulli, M. C., Woodcock, C. E., and Fagherazzi, S. (2016). Dynamics of a fringe mangrove forest detected by Landsat images in the Mekong River Delta, Vietnam. *Earth Surface Processes And Landforms*, 41:2024–2037.

Nguyen, A. D., Savenije, H. H. G., Pham, D. N., and Tang, D. T. (2008). Using salt intrusion measurements to determine the freshwater discharge distribution over the branches of a multi-channel estuary: The Mekong Delta case. *Estuarine Coastal And Shelf Science*, 77:433–445.

Nittrouer, C. A., Brunskill, G. J., and Figueiredo, A. G. (1995a). Importance of tropical coastal environments. *Geo-Marine Letters*, 15:121–126.

Nittrouer, C. A. and DeMaster, D. J. (1996). The Amazon shelf setting: Tropical, energetic, and influenced by a large river. *Continental Shelf Research*, 16:553–573.

Nittrouer, C. A., DeMaster, D. J., McKee, B. A., Cutshall, N. H., and Larsen, I. L. (1984). The effect of sediment mixing on Pb-210 accumulation rates for the Washington continental shelf. *Marine Geology*, 54:201–221.

Nittrouer, C. A., Kuehl, S. A., Sternberg, R. W., Figueiredo, A. G., and Faria, L. E. C. (1995b). An introduction to the geological significance of sediment transport and accumulation on the Amazon continental shelf. *Marine Geology*, 125:177–192.

Nittrouer, C. A., Raubenheimer, B., and Wheatcroft, R. A. (2013). Lessons learned from comparisons of mesotidal sand- and mudflats. *Continental Shelf Research*, 60:S1–S12.

Nittrouer, C. A., Sternberg, R. W., Carpenter, R., and Bennett, J. T. (1979). Use of Pb-210 geochronology as a sedimentological tool: application to the Washington continental shelf. *Marine Geology*, 31:297–316.

Nordfjord, S., Goff, J. A., Austin, J. A., and Gulick, S. P. S. (2006). Seismic facies of incised-valley fills, New Jersey continental shelf: Implications for erosion and preservation processes acting during latest Pleistocene-Holocene Transgression. *Journal of Sedimentary Research*, 76:1284–1303.

Norris, B., Mullarney, J., Henderson, S., and Bryan, K. (2017). Turbulence within a fringing mangrove forest - dependence on vegetation density. *Continental Shelf Research, in review.*

Nowacki, D. J., Ogston, A. S., Nittrouer, C. A., Fricke, A. T., Asp, N. E., and Souza-Filho, P. W. M. (2017). Seasonal, tidal, and geomorphic controls on sediment export to Amazon River tidal floodplains. *Journal of Geophysical Research, in revision.*

Nowacki, D. J., Ogston, A. S., Nittrouer, C. A., Fricke, A. T., and Van, P. D. T. (2015). Sediment dynamics in the lower Mekong River: Transition from tidal river to estuary. *Journal of Geophysical Research: Oceans*, 120:6363–6383.

Parkinson, R. W., DeLaune, R. D., and White, J. R. (1994). Holocene Sea-Level Rise and the Fate of Mangrove Forests within the Wider Caribbean Region. *Journal of Coastal Research*, 10:1077–1086.

Rajaratnam, N. and Ahmadi, R. M. (1979). Interaction between Main Channel and Flood-Plain Flows. *Journal of the Hydraulics Division*, 105:573–588.

Rogers, K. G., Goodbred, S. L., and Mondal, D. R. (2013). Monsoon sedimentation on the 'abandoned' tide-influenced Ganges–Brahmaputra delta plain. *Estuarine Coastal And Shelf Science*, 131:297–309.

Rudorff, C. M. and Melack, J. M. (2014). Flooding dynamics on the lower Amazon floodplain: 1. Hydraulic controls on water elevation, inundation extent, and river-floodplain discharge. *Water Resources Research*, 50:619–634.

Schaeffer-Novelli, Y., Cintrón-Molero, G., Adaime, R. R., and de Camargo, T. M. (1990). Variability of Mangrove Ecosystems along the Brazilian Coast. *Estuaries*, 13:204–218.

Schmidt, G. W. (1982). Primary production of phytoplankton in the three types of Amazonian waters. V. Some investigations on the phytoplankton and its primary productivity in the clear water of the lower Rio Tapajós (Pará, Brazil). *Amazoniana*, 7:335–348.

Shearman, P., Bryan, J., and Walsh, J. P. (2013). Trends in deltaic change over chree decades in the Asia-Pacific region. *Journal of Coastal Research*, 59:1169–1183.

Sioli, H. (1984). The Amazon and its main affluents: Hydrography, morphology of the river

courses, and river types. In Sioli, H., editor, *The Amazon*, pages 127–165. DR W. Junk Publishers, Dordrecht.

Smith, N. D., Pérez-Arlucea, M., Edmonds, D. A., and Slingerland, R. L. (2009). Elevation adjustments of paired natural levees during flooding of the Saskatchewan River. *Earth Surface Processes And Landforms*, 34:1060–1068.

Sommerfield, C. K. and Wheatcroft, R. A. (2007). Late Holocene sediment accumulation on the northern California shelf: Oceanic, fluvial, and anthropogenic influences . *Geological Society of America Bulletin*, 119:1120–1134.

Swanson, K. M., Watson, E., Aalto, R., Lauer, J. W., Bera, M. T., Marshall, A., Taylor, M. P., Apte, S. C., and Dietrich, W. E. (2008). Sediment load and floodplain deposition rates: Comparison of the Fly and Strickland rivers, Papua New Guinea . *Journal of Geophysical Research*, 113:F01S03.

Syvitski, J. P. M., Kettner, A. J., Overeem, I., Hutton, E. W. H., Hannon, M. T., Brakenridge, G. R., Day, J., Vörösmarty, C., Saito, Y., Giosan, L., and Nicholls, R. J. (2009). Sinking deltas due to human activities. *Nature Geoscience*, 2:681–686.

Ta, T., Nguyen, V., Tateishi, M., Kobayashi, I., Tanabe, S., and Saito, Y. (2002). Holocene delta evolution and sediment discharge of the Mekong River southern Vietnam. *Quaternary Science Reviews*, 21:1807–1819.

Thu, P. M. and Populus, J. (2007). Status and changes of mangrove forest in Mekong Delta: Case study in Tra Vinh, Vietnam. *Estuarine Coastal And Shelf Science*, 71:98–109.

Torres, A. M. (1997). Sedimentology of the Amazon mouth: north and south channels, Brazil. Technical Report 82, Keil.

van Straaten, L. M. J. U. (1961). Sedimentation in Tidal Flat Areas. *Bulletin of Canadian Petroleum Geology*, 9:203–226.

Vital, H. and Stattegger, K. (2000a). Lowermost Amazon River: evidence of late Quater-

nary sea-level fluctuations in a complex hydrodynamic system. *Quaternary International*, 72:53–60.

Vital, H. and Stattegger, K. (2000b). Major and trace elements of stream sediments from the lowermost Amazon River. *Chemical Geology*, 168:151–168.

Vital, H. and Stattegger, K. (2000c). Sediment dynamics in the lowermost Amazon. *Journal of Coastal Research*, 16:316–328.

Vital, H., Stattegger, K., and Garbe-Schonberg, C. (1999). Composition and trace-element geochemistry of detrital clay and heavy-mineral suites of the lowermost Amazon River: A provenance study. *Journal of Sedimentary Research*, 69(3):563–575.

Vital, H., Stattegger, K., Posewang, J., and Theilen, F. (1998). Lowermost Amazon River: morphology and shallow seismic characteristics. *Marine Geology*, 152:277–294.

Vo-Luong, H. P. et al. (2017). Erosion and deposition in Cù Lao Dung and Ca Mau Peninsula, Vietnam. *Continental Shelf Research, in review.*

Walcker, R., Anthony, E. J., Cassou, C., Aller, R. C., Gardel, A., Proisy, C., Martinez, J.-M., and Fromard, F. (2015). Fluctuations in the extent of mangroves driven by multi-decadal changes in North Atlantic waves. *Journal of Biogeography*, 42:2209–2219.

Wallace, A. R. (1853). *A narrative of travels on the Amazon and Rio Negro: with an account of the native tribes, and observations on the climate, geology and natural history of the Amazon valley.* Reeve and Company, London.

Walling, D. E. and Moorehead, P. W. (1989). The Particle-Size Characteristics of Fluvial Suspended Sediment - an Overview. *Hydrobiologia*, 176:125–149.

Walsh, J. P. and Nittrouer, C. A. (2004). Mangrove-bank sedimentation in a mesotidal environment with large sediment supply, Gulf of Papua. *Marine Geology*, 208:225–248.

Wells, J. T. and Coleman, J. M. (1981). Periodic mudflat progradation, northeastern coast of South America: A hypothesis. *Journal of Sedimentary Research*, 51:1069–1075.

Wilson, I. G. (1973). Equilibrium Cross-section of Meandering and Braided Rivers. *Nature*, 241:393–394.

Wittmann, H., von Blanckenburg, F., Maurice, L., Guyot, J.-L., Filizola, N., and Kubik, P. W. (2011). Sediment production and delivery in the Amazon River basin quantified by in situ-produced cosmogenic nuclides and recent river loads. *Geological Society of America Bulletin*.

Wolanski, E. (1995). Transport of sediment in mangrove swamps. *Hydrobiologia*, 295:31–42.

Wolanski, E., Ngoc Huan, N., Trong Dao, L., Huu Nhan, N., and Ngoc Thuy, N. (1996). Fine-sediment Dynamics in the Mekong River Estuary, Vietnam. *Estuarine Coastal And Shelf Science*, 43:565–582.

Wolanski, E., Nhan, N. H., and Spagnol, S. (1998). Sediment dynamics during low flow conditions in the Mekong River estuary, Vietnam. *Journal of Coastal Research*, 14:472–482.

Wolanski, E. and Ridd, P. (1986). Tidal mixing and trapping in mangrove swamps. *Estuarine Coastal And Shelf Science*, 23:759–771.

Wolman, M. G. and Leopold, L. B. (1957). River flood plains: some observations on their formation. Technical Report Professional Paper 282-C, United States Geological Survey.

Woodroffe, C. (1992). Mangrove sediments and geomorphology. In *Coastal and Estuarine Studies*, pages 7–41. American Geophysical Union, Washington, D. C.

Woodroffe, C. D. (2002). *Coasts: Form, process and evolution*. Cambridge University Press, Cambridge.

Wright, L. D. and Coleman, J. M. (1974). Mississippi River Mouth Processes - Effluent Dynamics and Morphologic Development. *Journal of Geology*, 82:751–778.

Young, B. M. and Harvey, E. L. (1996). A spatial analysis of the relationship between mangrove (Avicennia marina var. australasica) physiognomy and sediment accretion in the Hauraki Plains, New Zealand. *Estuarine Coastal And Shelf Science*, 42:231–246.

Zaitlin, B. A., Dalrymple, R. W., and Boyd, R. (1994). The stratigraphic organization of incised-valley systems associated with relative sea-level change. In Dalrymple, R. W., Boyd, R., and Zaitlin, B. A., editors, *Incised-Valley Systems: Origin and Sedimentary Sequences*, pages 45–60. SEPM, Tulsa, OK.

Zimmermann, R. C. and Thom, B. G. (1982). Physiographic plant geography. *Progress in Physical Geography*, 6:45–59.